NASA Technical Memorandum 86886

Fundamental Studies of Low Velocity Impact Resistance of Graphite Fiber Reinforced Polymer Matrix Composites

Kenneth J. Bowles
Lewis Research Center
Cleveland, Ohio

November 1985

NASA

FUNDAMENTAL STUDIES OF LOW VELOCITY IMPACT RESISTANCE OF GRAPHITE FIBER REINFORCED POLYMER MATRIX COMPOSITES

Kenneth J. Bowles
National Aeronautics and Space Administration
Lewis Research Center
Cleveland, Ohio 44135

SUMMARY

A study was conducted to relate the impact resistance of graphite fiber reinforced composites with matrix properties through gaining an understanding of the basic mechanics involved in the deformation and fracture process, and the effect of the polymer matrix structure on these mechanisms.

It was found that the resin matrix structure influences the composite impact resistance in at least two ways. The integration of flexibilizers into the polymer chain structure tends to reduce the T_G and the mechanical properties of the polymer. The reduction in the mechanical properties of the matrix does not enhance the composite impact resistance because it allows matrix controlled failure to initiate impact damage. Linear polymers, which contain no active groups for cross-linking, do not toughen composites because the fiber-matrix interfacial bond is not of sufficient strength

to prevent interfacial failure from occurring. Toughness must be built into the basic polymer backbone and cross-linking structure.

It was found that when the instrumented dropweight impact tester is used as a means for assessing resin toughness, the resin toughness is enhanced by the ability of the clamped specimen to deflect enough to produce sufficient membrane action to support a significant amount of the load. Thus, resin strain to failure is also significant. For composite specimens, the amount of deflection is limited by the magnitude of the strain at failure of the graphite fiber (less than 2 percent) and it appears that very little membrane action is realized during the impact of a composite.

Unidirectional composites do not appear to simulate the impact behavior of real structural composites and they are not recommended for use in assessing composite impact resistance with the dropweight impact tester.

The results of this study indicate that crossplied composite impact resistance is very much dependent on the matrix mechanical properties. When the matrix modulus is reduced, shear induced compressive failure may initiate composite impact failure. When the matrix strength is reduced, interlaminar shear stresses may become significant and initiate impact failure. Both

the modulus and the strength of the matrix must be increased to increase the composite impact resistance.

TABLE OF CONTENTS

CHAPTER I

INTRODUCTION

I-1. Background

With the sudden emergence of the energy crisis during the past decade and the subsequent rapid rise of energy costs, the light weight polymer matrix composites are being examined for their potential as fuel-conservative materials of construction for propulsion systems. The possible application of these materials to land propulsion systems is directed toward reducing system weight and thereby decreasing fuel consumption. In the aircraft industry, the fuel conservation concept is just one of a number of proposed payoffs resulting from the use of fiber reinforced composites. Manufacturing costs can be projected to be reduced for a large number of aircraft structures. Strength can be directionally designed into a structure because of the anisotropy of the composite. This concept can conceivably be used advantageously to produce less bulky structures by tailoring the fiber orientation so that the required strength is provided only where it is necessary in the direction of predicted critical stresses.

In both the land propulsion and air propulsion industries, polymer matrix composites have already

become accepted as materials of construction for system structural parts. While their use is presently limited to secondary structural assemblies in propulsion systems, a great amount of effort is being expended to provide the necessary assurance that these materials can be used as engineering materials for primary load bearing structures. With the development of the polyimide resins which, when used with graphite fibers, extend the use of polymer matrix composites to a temperature limit of about 550° F, composites can also be considered for use in aircraft engines [1].

Some of the advantages of using graphite fiber reinforced composites for aircraft engines are as follows:

(1) Low density.

(2) High specific strength.

(3) High specific modulus.

(4) Composite insensitivity to fatigue.

(5) Composite insensitivity to creep.

The anisotropic nature of composite materials does introduce some disadvantages in their use. Normally, composite structures are built up by stacking either unidirectional plies or woven fabric plies on top of one another until the stack contains the required amount of material. While relatively high tensile strengths and

moduli can be achieved in the direction of the reinforcing graphite fibers, very low tensile properties and moduli are realized in the direction perpendicular to the fiber direction. In order to increase the transverse strength to acceptable levels, "angle plies", with fibers oriented at angles other than 0° are designed into a composite structure. Normally, these plies are interspersed between the primary load carrying plies. When this is done, the strength requirements can often be met in the two dimensional plane parallel to the surface of the composite. The thickness direction is, therefore, composed of a number of interfaces of fibers oriented in different directions, and the through-the-thickness strength is low.

The bond between the different laminae is a bond supplied by the matrix resin or the fiber-matrix interface. The matrix mechanical properties are very low in comparison with the fiber mechanical properties. While the interlaminar strength is low because of the low resin strength, the situation is further complicated by the fact that rather high residual stresses can be set up in the matrix because of the differences in thermal expansion, not only between the resin and the fiber, but also between the fibers with different orientations. The residual stresses are a result of the cooling of the

cured composite material from the elevated curing temperature normally employed to room temperature. The interlaminar interfaces are considered to be the weak link in this type of composite design.

High modulus resin matrix fiber reinforced composites materials are normally characterized as brittle materials with low through-the thickness tensile strength, and are highly susceptible to delamination and interlaminar shear failure. These unattractive aspects limit the use of these materials to structural application where significant levels of delamination and transverse stresses are anticipated. Since impact loading of a structure can introduce these types of stresses, as will be seen later, there is a hesitancy to use composite materials in a structure which may be subjected to impact loading during its lifetime without an adequate proof testing program on actual structural components.

I-2. Current Approach to the Problem

During the past ten years, a significant amount of work has been directed to the use of resin matrix fiber reinforced composites as materials of construction for turbofan aircraft engine components. Of special interest is the potential of using this material for engine fan blades. In use, fan blades are exposed to impact by foreign objects such as birds, stones and ice balls.

Most efforts in this work culminated in very expensive and time consuming simulated impact tests in which a real blade was impacted by a real or simulated bird [2 to 4]. Blade designs were proposed incorporating design features which had logically evolved to eliminate those failure mechanisms found to predominate in previous tests. In general, the programs were simply testing of ideas, and in some cases, not supported by analytical data to support the design feature selection. Some types of blade designs, although not successful in withstanding impact loading as would be imparted by a bird, did exhibit improved performance over other types of design. In these cases, solutions were sought from examination of reinforcement utilization and structural placement of various types of reinforcement. Minimal consideration was given to resin properties because composite impact behavior was believed to be fiber dominated [6].

For lower speed impacting, such as tool droppage, ice impact, and even bird impact with a static engine component or substructure, it has been found that non-visible damage can occur as a result of the impact [5]. The damage can occur within the composite material without visibly damaging the surface. The damage can exist in the form of an interior delamination. These types of failures are related to resin or fiber-resin interface

failures. It is this type of impact and toughness characteristics of fiber reinforced polymer matrix composite material that is the subject of the present study.

At this time, there is a significant effort being expended in the aircraft industry, in Universities and in Government laboratories to produce tougher resins. It is expected that by producing a tougher resin, the resin toughness can be translated into tougher resin matrix composites. For example, those impact failure mechanisms which are influenced by interlaminar shear strengths and strains, transverse tensile strength and strains, and fiber pull-out energies, (all of which are resin controlled properties), can be measurably altered by proper selection of resin properties. It should be noted, however, that no definition has been proposed which specifies the exact mechanical characteristics of a tough resin. Most investigators infer that a tough resin possesses a significant amount of ductility or tensile strain to failure.

To date, the translation of tougher resin properties into tougher composite properties has not been clearly demonstrated. Further, it has not been demonstrated that resin properties cannot be translated into tougher composite properties.

Miller, Hertzberg, and Ratana [7], have studied the effect of a few resins on the toughness of both fiberglass and graphite reinforced unidirectional composites. One of these results was the development of an elastomeric resin purposely designed to possess those mechanical properties which the investigators believed would translate into improved composite toughness. They evaluated composite toughness by two different methods. In the first method, instrumented drop weight impact tests were conducted on samples of composites containing each of the resins chosen for study. The results from these tests were used to assess the resistance of each composite material to initiation of failure.

The second test method utilized in this study was a fracture toughness test which was designed to measure the interlaminar fracture toughness of the composites studied. The specimen used was of a double cantilever beam design. The test results were used to assess the resistance of the composites to the propagation of damage.

The results of these tests demonstrated a significant improvement in the interlaminar fracture toughness of the composite with the more ductile polymer-elastomer matrix in comparison with that of the more brittle resins studied. The investigators, however, did not characterize the mechanical properties of the resins nor did

they describe the elastomerized resin adequately with respect to what was the chemistry or mechanism for elastomerizing the resin.

Winsa and Petrasek [8] investigated the effect of matrix and fiber toughness on unidirectional metal matrix composite impact strength. They demonstrated that the metal matrix composite toughness was influenced by the toughness of the reinforcement fibers, the interfacial reactions, and the metal matrix. Tungsten fibers were used as the reinforcing material. Copper, copper-10 nickel and a superalloy matrix were included to vary matrix toughness. The copper was the toughest and the superalloy was the least tough matrix. Variation of the tungsten toughness was achieved by conducting tests both below and above the tungsten ductile to brittle transition temperature. Toughness measurements were made using an Izod impact tester. The moduli of the metal matrix materials investigated are significantly greater than those of polymers, and thus the metal matrix contributes more to the impact resistance of the metal-composite material than the polymer matrix does when using reinforcement with comparable moduli.

Chamis, Hanson and Serafini studied the effects of composite constituent variables on the impact resistance of unidirectional composites [6]. In addition, a number

of proposed impact failure mechanisms were mathematically modeled to assess the criteria for improving composite impact resistance. The test used in this work to assess toughness was an Izod impact test. By calculating the failure energies of the significant failure mechanisms, the investigators were able to rank the effectiveness of the different composite systems qualitatively in resisting impact. Some of the conclusions resulting from this work are:

(1) Longitudinal impact resistance can be fiber controlled.

(2) Transverse and shear impact resistances can be matrix controlled.

(3) Three prevalent longitudinal impact failure modes are cleavage, cleavage with fiber pull-out, and cleavage combined with partial delamination.

(4) Transverse impact failure mode was cleavage.

Novak and DeCrescente [9] used Charpy impact testing to measure the impact resistance of various resin matrix/fiber reinforced composite systems. Epoxy/glass, epoxy/boron and epoxy/graphite composites were studied. It was found that the glass reinforced composites had the highest impact resistance and the graphite fiber reinforced composites had the lowest impact resistance. This was attributed to the higher strain to failure of the glass fiber. Energy-absorbing failure mechanism

were considered; the effect of the matrix deformation on the amount of energy absorbed during failure was not found to be a significant energy-absorbing factor from mathematical models of these failure modes. Other conclusions the authors reached, based on their studies, are:

(1) Three energy absorbing mechanisms of fracture are filament fracture, filament pullout, and shear delamination.

(2) The single most important parameter governing composite Charpy impact strength is the stress-strain behavior of the reinforcing fiber.

(3) The toughness of boron and graphite reinforced composites can be improved by the addition of glass fibers.

A number of other studies have been conducted to evaluate the impact performance of other types of composite materials [10 to 12]. Except for the work in Reference 7, the impact testing involved small, unidirectional test specimens. The ply stacking sequence in angle plied composites introduces stress conditions into the composite sample which are not present in the simple unidirectional specimens normally used in the pendulum tests. Thus, the dominant failure mechanisms resulting from the angle plied composite impact tests would not be expected to be identical to those observed for the

smaller unidirectional specimen tests. The difference in specimen sizes and the elimination of the possible small specimen "edge effects" [13] would produce impact reactions within the specimens more like those present in actual structural components, especially for structures such as "skin" sections found on aircraft wings or fuselages.

A specific failure sequence would be applicable to a particular composite design. For example, it would not be expected that a composite structure that was filament wound with interwoven continuous fibers would react to impact in a manner identical to that of a structure made from a molding compound filled with discontinuous fibers. The interweaving of the wound fibers would strengthen the composite in the thickness direction.

Because of the large number of composite designs that are available (composite designs refers to the manner in which the composite material is built up and the form of the ply material), it is impossible to devise a universal model for examining impact and toughness. One of the most common models in use today for analyzing composite structures is that comprised of individual unidirectional laminae of continuous fibers and matrix materials. The individual laminae can be oriented so that the reinforcing fibers in adjacent laminae are

either parallel (unidirectional) or are skewed at angles ranging between 0° and 90°. This will be the model for this study.

As with other impact tests, the tests using the larger specimens with more realistically oriented reinforcement also do not produce engineering type information which is directly applicable to structure design, or which can be interpreted as an intrinsic property of a material. They have been useful in characterizing impact failure mechanisms for the type of impact that was involved; there seems to be good agreement among various investigators as to the failure mechanisms involved. The tests ranged in nature from low velocity drop weight impact tests to high velocity projectile impact tests.

Based on the velocity of the impacting projectile, the impact tests can be categorized into three general groups [5]. They are as follows:

(1) High velocity or ballistic. Velocity > 2000 ft/sec (61×10^3 cm/sec).

(2) Intermediate velocity. 150 ft/sec (4.6×10^3 cm/sec) < Velocity < 2000 ft/sec (61×10^3 cm/sec).

(3) Low velocity impact. Velocity < 150 ft/sec (4.6×10^3 cm/sec). Only in the low velocity regime (3 above) is it believed that wave effects are negligible

and that structural analysis can be used to predict the specimen impact response. In these tests, the projectiles used included steel balls, ice balls, and gelatin balls.

Greszczuk [14], presents failure mode sequences which are representative of the results from the tests. For this model, the impact sequence for a spherical object striking a flat composite plate would be as follows:

(1) Elastic compression

(2) Crushing through the impacted surface

(3) Delamination by interlaminar shear

(4) Fiber fracture and matrix fracture (Cleavage)

(5) Fiber pullout

The elastic compression represents a very low energy absorbing process for graphite fiber reinforced composite materials [15].

I-3. Objectives of the Present Study

The purpose of this study is that of relating toughness and impact resistance of graphite fiber reinforced composites with matrix properties through the process of gaining an understanding of the basic mechanisms involved in the deformation and fracture process, and the effect of the polymer matrix structure on these mechanisms. Of special concern is the potential of

being able to determine those measured matrix properties which can be translated into composite toughness properties. If this were realized, the search for tougher resins could be simplified by reducing the present two-step characterization procedure, with both resin and composite studies, to a "significant resin property" study.

The pre-established definition of low velocity impact toughness was visualized as the ability of the composite material to resist incipient damage (actual failure of one or both of the composite constituent materials) and the ability of the material to resist damage propagation. It has been observed that the damage propagation normally occurs as interlaminar crack growth (delamination). Thus, two toughness tests were chosen to evaluate the toughness properties of the matrix resins and the composite materials under study. One of these tests was the drop weight impact test in which the test material was impacted with a falling one-half inch diameter penetrator. This test was selected as being able to provide both incipient damage and penetration resistance information. The second test was the double cantilever beam "fracture toughness" test. This test was chosen to provide information as to the ability of the different composite materials to

resist the propagation of cracks or damage initiated by low velocity impact.

CHAPTER II

MATERIALS SELECTION AND COMPOSITE FABRICATION

II-1. Resin Matrices

In general, there are four ways in which to impart some degree of toughness to a resin system. One method is that of introducing flexibility into the backbone of the polymer chain as a flexible hinge point. Two groups which are commonly introduced into backbone structures to add flexibility are the ether group and the isopropylidene group. These groups allow complete freedom of rotation of chains or chain segments about their position in the backbone.

Sometimes, rather than to design a polymer chain with inherent flexibility, it is simpler and more expedient to introduce a long-chain element into an epoxy system. An example of this long-chain element is one which reacts during the cure. These types of elements are called flexibilizers. The use of these flexibilizers tends to reduce system functionality in terms of epoxy equivalent weight, introduces long chain segments in the polymer network, and increases the free volume of the system. In turn, this allows the flexibilized

crosslinked structure to move more freely under imposed loads.

Another way in which to toughen a crosslinked polymer system is the use of appropriate crosslinkers which decrease the crosslink density. In general, by decreasing the crosslink density, one can improve polymer toughness and increase polymer elongation [16].

The fourth way in which to toughen a polymer is that of dispersing an elastomeric phase throughout the polymer phase. The elastomeric particles appear to initiate and to control craze formation so that impact energy is dissipated in the production of numerous small crazes [17,18].

Of these four available means, the use of elastomeric dispersion within the polymeric material was eliminated as a method for the present study. The addition of a third phase to an already complicated two-phase material study would increase the scope of this work to an unmanageable level.

For the purposes of this investigation, resins were chosen to satisfy criteria based on their mechanical properties. The resins were selected to provide a wide range of yield and/or fracture strengths, initial tensile moduli, and strain to yield and/or fracture.

It was expected that a sufficiently wide range of resin mechanical properties would allow subtle effects

of resin mechanical properties to be observed in those composite mechanical properties and failure mechanisms which could be rationalized as affecting the toughness properties of composite materials.

In order to satisfy this resin selection criteria, it was not possible to fully control or characterize the chemical structures of the selected resins. It was not within the scope of this work to develop resins with tailor made properties. Resin selection was accomplished by reviewing manufacturer's mechanical properties data and choosing those resins which would provide a significantly wide range of mechanical properties. Four resins were chosen for the program.

The first resin selected was the Fiberite 930 resin (hereafter referred to as 930 resin) was selected because it has a relatively high strength to failure typical of the epoxy resins currently being used today. The chemical structure of this resin is that of an aromatic diglycidyl ether (DGEBA). The structure is similar to that shown below.

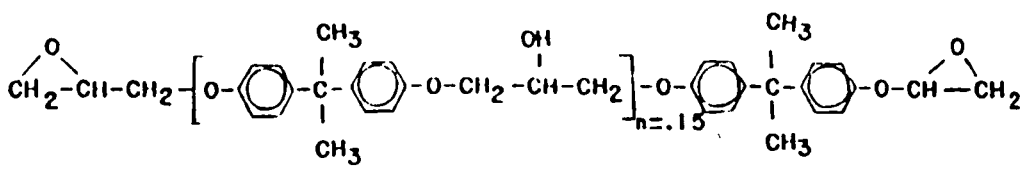

The symbol n denotes the number of times the structure within the brackets is repeated within the complete chain.

The curing agent is an aromatic diamine with a structure like the following:

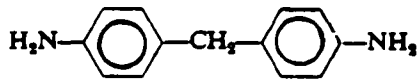

Resins cured with curing agents which contain aromatic rings are more rigid and make a stronger cured resin than those cured with aliphatic curing agents. A cured resin containing more aromatic rings has greater thermal stability and chemical resistance than a resin with few aromatic rings.

The curing of this resin was carried out at 350° C for 2 hr. This resin is considered to be a "high temperature epoxy" resin. The high rigidity of the resin molecule necessitates a high cure temperature because of the reduced molecular mobility needed to position the two reactive end groups properly for reaction.

The second resin selected was the Union Carbide P-1700 polysulfone (P-1700), a tough, thermally stable thermoplastic resin with the following structure:

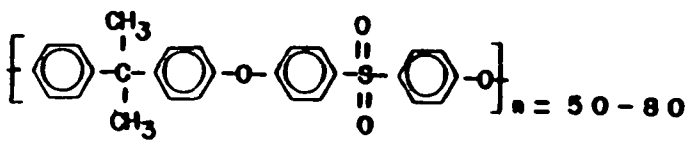

This structural unit is composed of three phenylene rings linked by three different chemical groups. The three groups are isopropylidene, ether, and sulfone. The most distinctive feature of the backbone chain is the diphenylene sulfone group:

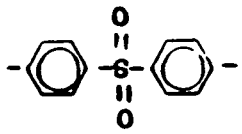

The sulfur atoms in this group are in their highest state of oxidation. Also, the sulfone group tends to draw electrons from the adjacent benzene rings, making them electron-deficient. Substances which are stable to oxidation strongly resist the tendency to lose their electrons to an oxidizer. The entire diphenylene sulfone group is in a state to resist oxidation.

The diphenylene sulfone group also contains chemical bonds with high strength. This group is an aromatic group and possesses the capability of a high degree of resonance. A highly resonant group produces bonds that are stronger than it is otherwise possible to attain. The result of this resonance is that the atoms comprising the sulfone group are fixed in a rigid spatial configuration. The resonance imparts the characteristics of thermal stability, oxidative stability and rigidity to the polymer at high temperatures.

The other groups within the backbone structure contribute characteristics to the polymer which are desirable for processing and end use. Both the ether group and the isopropylidene group add flexibility to the backbone. The ether group also contributes to the thermal stability of the polymer. This material is a thermoplastic which contains no crosslinking; this further enhances the toughness of the polymer.

The other resins which were characterized in this research study are closely related in that they are both formulated from mixtures of two Ciba-Geigy resins. One of the formulated resins was mixed as follows:

Ciba Geigy	6010 Resin	50 grams
Ciba Geigy	508 Resin	50 grams
Ciba Geigy	840 Hardener	24.5 grams

In this report, the formulated resin is designated by the hardener number - (840).

The second formulated resin was similarly mixed and the proportions are as below:

Ciba Geigy	6010 Resin	40 grams
Ciba Geigy	508 Resin	60 grams
Ciba Geigy	956 Hardener	17.5 grams

This resin will also be designated hereafter by its hardener identification - (956). The 6010 resin, which is used in both the 840 and 956 resins, is a diglycidyl ether of bisphenol A (DGEBA) and has the following structure:

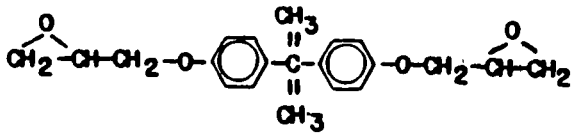

The epoxy equivalent weight, in gram/equivalent, is 185 to 190. The epoxy equivalent weight is defined as the molecular weight of the chain per epoxide group. The $-\underset{2}{CH}\overset{O}{\diagdown\diagup}CH$ group at the ends of the above figure is the epoxide group. During polymerization, the epoxide ring opens up to react with another pendant group in another molecule of either the resin or the hardener. This results in crosslinking. As the crosslink density increases, resin brittleness increases, as a general rule. From the epoxy equivalent weight magnitude, it can be deduced that the 6010 resin, after curing, is a brittle resin, since the molecular weight of the chain between the two epoxide groups is about 360 to 380. The resin, or backbone is therefore relatively short and probably rigid. Manufacturers data give the tensile strength and fracture strain as 7000 psi (48.3 MN/m^2) and 0.02 respectively.

To illustrate the significance of the information supplied by the epoxy equivalent weight, the structure of the 508 resin can be taken as a case in point. The 508 resin is a modified 6010 resin. The 6010 resin is diluted with an epoxidized polyol; the exact polyol

structure is not important in understanding the effect of the structure on the mechanical behavior of the cured resin. The equivalent weight resulting from the mixture of 6010 and the epoxidized polyol raises the epoxy equivalent weight from 185-190 to 500-550. If the majority of atoms are carbon atoms with a molecular weight of 12, there are close to 100 carbon atoms between epoxide groups. Recalling that the structure of DGEBA has seven atoms and two six member rings between epoxide groups, there is a possibility that the main backbone of the resulting 6010 resin mixture between the crosslinks could be very long and thus flexible. It would be significantly shorter if aromatic rings were included in the length of the chain between the epoxide groups. The extreme length of the chains allows the possibility of a high degree of flexibility within the chains. This can result in an actual folding over of the chains and maybe some entanglement with other molecular chains. Under these conditions, when a stress is applied to the cured resin, the chains will tend to straighten out and untangle. This will be evidenced by a significant strain to yield or strain to failure and strain rate sensitivity.

The hardeners used to crosslink the epoxy systems also have an effect on the properties of the resulting cured resin systems. For the two Ciba-Geigy polymers,

two different hardeners were used. One was an oxylated triethylenetetramine (956) and the other was a polyamide (840).

The 956 hardener has the following structure:

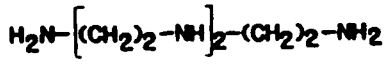

The chemical name is triethylenetetramine (TETA). A number of points can be made about this structure which will help to understand and rationalize the influence of this material on the cured resin mechanical behavior. At each end of the chain is a NH_2 group (primary amine) while within the chain are two NH groups (second amine). The primary amine groups are more reactive than the secondary amines and they can react with the epoxide group as follows:

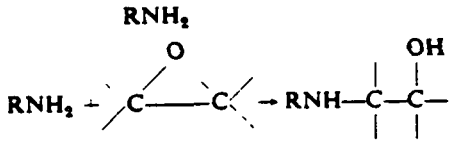

Thus, it is possible for each primary amine to link two epoxy chains together with itself. In contrast, each secondary amine in the central part of the chain

can react with only one epoxide group by a similar reaction.

The polyamide, 840, hardener has a structure as shown below:

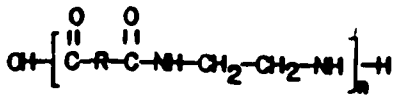

For the 840 hardener, the value of n is 5 to 15. The identification of the R group is proprietary. While the TETA chain contains reactive hydrogens, the polyamide contains only two reactive hydrogens in each repeating group. The distance between these functional groups is dependent on the nature of the R group within this repeating structure. The reaction of the amide group with the epoxide group is inhibited in comparison with the reaction of the amine group, because of the structure. If the R group is aliphatic, the crosslinking density (functional groups per length of chain) could be less for the amide compound than for the amine hardener.

II-2. Graphite Fiber Reinforcement

The graphite fiber used in this research program is a PAN (Polyacrylonitrile) based high strength fiber marketed by the Celanese Plastics and Specialties Co.

and designated as Celion 6000. The mechanical properties, as provided by the vendor are listed in Table 1.

The density of the fibers is 1.77 gm/cc. The precursor of this fiber (Polyacrylonitrile) is a polymer with a continuous C-C chain and pendant nitrile groups. The polymer can be readily cyclised into a ladder polymer with hetero-atoms. During the process used to convert the polymer to graphite fiber, the polymer structure forms graphite like planar layers which become arranged to form parallel ribbon-like bundles. The strength and stiffness of the resulting graphite fiber are functions of the orientation of the graphite fiber ribbons in relation to the fiber axis.

The fiber was purchased and used without a surface finish. The surface treatment used in the manufacturing process, as described by the vendor, was a liquid phase oxidation which was continued to equilibrium.

It has been proposed that the bond between the fiber and the polymer matrix is both chemical and physical in nature [19]. It has been found that to achieve good reinforcement of a polymer by a carbon fiber, chemical bonding between the fiber surface groups and the functional groups in the resin matrix should occur. Both the chemical nature of the fiber surface and the type of surface treatment determine the nature of the surface groups present on the fiber. The most important

method of producing functional groups on graphite fiber surface is treatment by surface oxidation. It has been shown that oxides can become attached to surface areas where free vacancies of the graphite carbon atoms have not been saturated [20]. Free vacancies are formed by faults in the graphite structure or by peripheral atoms of the graphite layers at the surface (Figure 1). The peripheral atoms only have two neighboring C atoms.

In reality, the base surfaces of the graphite crystals are chemically inert since all carbon atoms are sp^2 hybridized and these valencies are saturated by neighboring carbon atoms. The free pi-electrons serve to build up the graphite layer structure which is held together by Van der Waals forces.

Liquid phase oxidation of graphite fibers, such as the Celion 6000 fibers, is carried out with oxidizing liquids such as boiling nitric and sulfuric acids. In order to reach equilibrium, when nitric acid is used as an oxidizer, the time of treatment can range between 15 min and 100 hr.

Some of the surface groups which are formed by wet oxidation are hydroxyl, carbonic, carboxylic and phenolic groups. Nitric acid oxidation of PAN based carbon fibers results in etching or smoothing at the microscopic level and an increase in functionality on the molecular scale. Hydroxyl surface groups are formed by

liquid phase treatment of more highly graphite fibers with a mixture of $KMNO_4$ and H_2SO_4. The exact nature of the resulting surface group depends on a number of factor which are controlled by the oxidizing process and the oxidizers. In the past the effectiveness of the surface treatment has been monitored qualitatively by relative interlaminar shear strength values and wetability of the fiber by the resin.

II-3. Composite Fabrication

All composites were made up from unidirectional prepreg plies. Prepreg processing was carried out as follows:

(1) For the epoxy resins, the dry Celion 6000 graphite fiber was wound onto a 30 inch (76.2 cm) diameter by 24 inch (13 cm) long cylindrical mandrel which was covered with a silicone coated release paper. The winding was done at a spacing of 12 turns/inch (4.7 turns/cm). The mandrel speed was 10 rpm and the fiber tension was maintained at 0.25 lb (1.11 N). The amount of resin used to impregnate the fibers was calculated to produce a cured laminate with about 60 volume percent fibers. The 930 resin was dissolved in acetone (28 weight percent acetone) before the impregnation. The solution was pumped onto the fibers with a metering pump. After impregnation, the prepreg material was

allowed to dry on the mandrel until the acetone evaporated and only a slight tackiness was evident on the prepreg surface. The 840 and 956 resins were applied to the graphite fibers in a solventless condition by pouring onto the fibers and then spreading evenly over the rotating surface with a roller. Since the gel time for these resins at room temperature is very short (around 45 min), immediately after impregnation, a portion of the prepreg was frozen with an instant freeze spray. The frozen area was cut across the fibers with a razor, and the tacky prepreg, supported by the release paper, was taken off the mandrel. The prepreg material was then immediately put into a freezer to prevent gellation of the resin. After being frozen, the prepreg sheets were cut up into plies of the required dimensions and fiber orientation. The pre-freezing was not necessary for the 930 prepreg. All prepreg material was stored in a freezer until it was processed into cured laminates.

(2) The P-1700 resin was acquired in pellet form. The pellets were first dried in an oven at 150° C for 4 hr to remove absorbed moisture. The resin was then dissolved in methylene chloride to make a 10 percent solids solution of the resin. In order to attain satisfactory impregnation of the graphite fibers with the resin solution, the graphite fibers were wet-wound onto the mandrel. The fibers were taken from the spool and

run through a resin solution bath after the tow was spread over a 0.5 inch (1.25 cm) diameter Teflon roller. Excess solution was removed as the tow material passed over an exiting roller. The wet tow was then passed through the delivery eye onto the rotating mandrel. The prepreg was allowed to dry by solvent evaporation on the mandrel until it became "boardy". It was then removed from the mandrel and cut into the ply configuration that was required for testing.

(3) All composite laminates were made by compression molding in matched metal die molds. Compression pressures were provided by heated hydraulic presses. The laminate processing parameters are listed in Table 2.

(4) The molds and laminates were removed from the press, allowed to cool in air and then the cured laminates were removed from the mold. The epoxy laminates were post cured at their respective cure temperature for an hour.

Laminate quality was determined by two methods. Through transmission ultrasonic C-scans were run on each laminate after fabrication and then, when possible, samples were cut from the laminates and examined microscopically for voids and cracks.

CHAPTER III

MATERIAL CHARACTERIZATION PROCEDURES

III-1. Regular Tensile Tests

All tensile testing was carried out on gear driven tensile test machines at a constant crosshead speed. One of the machines was an Instron Universal Testing Machine. The other was a Rhiele Testing Machine. All testing was done at a temperature of 22° C ± 1.5° C and the crosshead speed was adjusted to provide an initial strain rate of 0.05 per minute in the gage section of the specimen.

The values for Young's moduli and Poisson's ratios for composites were measured using straight sided specimens cut with a water cooled diamond wheel from flat resin plates of about 0.135 inch (0.38 cm) thickness. The specimens were 0.50 inch (1.27 cm) wide and 6 inch (15.24 cm) long with fiberglass reinforced end tabs bonded in place. The strains were measured by four strain gages bonded to the specimen. A longitudinal and a transverse gage were bonded to each side. The modulus and Poisson's ratio for the test piece were taken to be the average of those calculated from the strains on each side of the specimen. The neat resin[1] specimens which

were stressed to failure and the transverse tensile composite specimens were of a "dog bone" shape and are shown in Figure 2.

The neat resin strain to yield, strain to fracture, yield stress and fracture stress were also measured using clip-on extensometers. To prevent slippage of the extensometer during a test, thin slices of "double-sided" tape were wrapped part way around the specimen at the positions where the extensometer knife edges touched the specimen.

When strain gages were used, the output was recorded as traces on two x-y-y' recorders with longitudinal strain versus load and longitudinal strain versus transverse strain on one recorder and the same longitudinal strain versus the longitudinal and transverse strains of the second pair of gages on the second recorder. The composite tensile specimens were instrumented in the same manner as the strain gaged neat resin samples.

III-2. 10° Off-Axis Tensile Tests

Ten degrees off-axis tests were conducted to assess shear stress effects. Since the 10° off-axis tensile test is not a standard mechanical properties test and is

---

[1]The term, neat resin, denotes a pure resin without any fillers or contaminants.

relatively new [21], a brief explanation of the test seems warranted. The description of this test is found in Appendix A. A schematic of the test specimen is shown in Figure 3. The unidirectional fibers are oriented 10° off the axis along which the test load is applied. The test specimens measured 0.5 inch (1.27 cm) by 8 inch (20.3 cm) long by 0.125 inch (0.32 cm) thick. The ends were tabbed with fiberglass reinforced tabs. Two 60° strain gage rosettes were bonded to each specimen. One gage was bonded on each of the two 0.50 inch (1.27 cm) wide surfaces of the specimen. The tests were conducted using the same procedure as was used in the tensile testing.

III-3. Compression Tests

Compression tests were conducted with neat resin and composite test pieces to assess compression effects that may contribute to composite impact failure.

Resin and composite test pieces were tested under compression with an Instron Tensile Test Machine at an initial strain rate of 0.05 per minute. The test temperature was controlled at 22° C ± 1.5° C for all the tests. All the test specimens were instrumented with four grid-type strain gages. One longitudinal gage and one transverse gage was bonded to each side of each specimen.

Three types of compression specimens were used in this study. They are described as follows:

(1) Flat specimens measuring about 0.12 inch (0.29 cm) by 0.500 inch (1.27 cm) by 3.25 inch (7.8 cm) were used to measure the compression strengths of the composites that were evaluated in this study. The slenderness ratio of the gage length between the end blocks (Figure 4) was 15:1 as specified in ASTM D695-77.

(2) The three epoxy resins were cast into 0.50 inch (1.27 cm) diameter rods and then cut into 1.75 inch (4.38 cm) long cylinders. This provided a length to diameter ratio of 2.6:1 which has been shown to be sufficient to insure that end effects from the constraint of the compressing platens would not extend into the strain gage area of the specimens [22]. The strain gages occupied a 0.25 inch (0.64 cm) long section in the middle of each specimen.

(3) Since the P-1700 thermoplastic resin had to be molded to shape at a temperature in excess of 600° F, specimen rods could not be made conveniently as with the epoxy resins. Flat plates were molded and cut into 0.50 inch (1.27 cm) by 0.50 inch (1.27 cm) compression specimens. Length to width ratios of 2.6:1 were maintained as with the cylindrical specimens. Square bar specimens of the 956 and 840 resins were also made to determine if any variation of the test results could be

attributed to the geometry of the specimens. Strain gage positioning was equivalent to that for the cylindrical specimens. Both moduli and Poisson's ratios were measured with these specimens.

In order to reduce the constraint of the compressing platens on the specimen ends, 0.003 inch (0.0076 cm) thick Teflon film was placed between the platens and the specimen ends of type 2 and 3 specimens above.

III-4. Resin Fracture Toughness Tests

Mode I plane strain fracture toughness tests were performed on specimens of the four neat resins as specified in ANSI/ASTM E 399-78. A schematic of the compact tensile specimen, as shown in Figure 5, was used. The test specimen was loaded with an MTS Machine at an initial crosshead speed of 0.1 inch/min (0.254 cm/min). The crack opening displacement was measured with a double-cantilever clip-on displacement gage. The gage was mounted between two razor blade sections bonded on either side of the machined starter-crack as shown in Figure 5.

The epoxy resins were cast between two flat aluminum plates into sheets of the required thickness. Specimens were machined from these cast plates. The P-1700 specimen blanks were molded in matched metal die

molds. Molding and curing procedures were as previously described in Table 2.

The starter-cracks were made by first cutting the root of the machined crack with a 0.012 inch thick jeweler's saw blade and then extending this cut by pressing a razor blade into the uncut resin. Crack lengths were measured from the fracture surfaces after testing was completed.

III-5. Dynamic Mechanical Properties Measurements

Dynamic mechanical properties measurements were made on the four neat resins and their respective Celion 6000 fiber reinforced composites using a Rheometrics Dynamic Mechanical Analyzer (Figure 6). Flat plate specimens were tested. The test piece dimensions were 1.5 inch (3.8 cm) long by 0.5 inch (1.27 cm) wide by about 0.10 inch (0.254 cm) thick. This test utilizes the measurement of torque in forced torsion of the flat specimen to calculate the stored shear modulus (G'), the loss shear modulus (G") and the damping factor as a function of temperature, strain rate, or strain. Also the resin glass transition temperature (T_G) can be measured with this test equipment. Details of the dynamic mechanical analyzer and the testing procedure are given in Appendix B.

III-6. Relaxation Tests

Relaxation testing was done at a temperature of 22° C ± 1.50° C with only one specimen of each of the four resins. The samples measured 2.50 inch (6.35 cm) by 0.5 inch (1.27 cm) by 0.125 inch (0.286 cm) in thickness. The ends were tabbed and the specimen configuration was straight sided rather than dog-boned in shape. The samples were stressed as quickly as possible but not so quickly as to lose the ability to control the desired test load. Strain values at the initiation of the tests were kept at values in the range where all the stress strain curves are reasonably linear. The samples were instrumented with grid type strain gages to measure the test strain and to monitor possible variations in sample strain during the tests. A transverse and longitudinal strain gage was bonded to each side of the specimen. Both Young's Modulus and Poisson's ratio were measured during the test. Load measurements were taken at time intervals which increased as the testing progressed.

III-7. Thermal Expansion Measurements

A DuPont Thermal Analyzer (Model 942) was used to measure the thermal coefficient of expansion and the glass transition temperature for each of the resins and composites being studied. These properties were measured in order to try to characterize the stress and

structural (chemical) state of the resins as matrices in the composites. This test warrants a brief description because of its uniqueness. The description is given in Appendix C.

III-8. Composite Interlaminar Fracture Toughness Tests

Composite fracture toughness testing was conducted on double cantilever beam (DCB) specimens. The specimen design is shown in Figure 7. In this test an existing crack, formed by a short length of Teflon film positioned between the two central laminae of the specimen, is caused to extend through the length of the specimen. The crack growth is accomplished by pulling apart the end of the specimen containing the Teflon film. Load and displacement are measured and the energy release rate (G_{IC}) is calculated from the data. The details of this test procedure are given in Appendix D.

III-9. Drop Weight Impact Testing

Both the neat resin samples and the composite samples measured 6 inch (15.24 cm) by 6 inch (15.24 cm) by about 0.125 inch (0.318 cm) in size. Three types of samples were tested. These types were:

(1) Fifteen plies in a 0°/90° fiber orientation sequence ,

(2) Thirty plies in a 0°/90° fiber orientation sequence

(3) Fifteen plies in a unidirectional stacking sequence

The samples were clamped along all four edges. The impactor was a 0.5 inch (1.27 cm) diameter cylinder with a spherical end. The impactor (tup) was instrumented with strain gages to measure the impacting loads. The test is described in Appendix E.

III-10. Miscellaneous Tests

Throughout the duration of this study, a number of tests were conducted which generated data as required to characterize specimen composition (fiber volume, void content, etc.). These tests are described briefly below.

Composite composition and quality were determined by a combination of analytical testing procedures. The fiber content was determined by sulfuric acid digestion of matrix resins and hydrogen peroxide treatment as described by Jones, et al. [23]. The weight fractions of fiber and resin were determined by this method and then converted to volume fractions by utilization of the following equation:

$$K_{vf} = \frac{D_f K_{wf}}{D_r K_{wf} + D_f K_{wr}} \qquad (1)$$

K_{vf} = volume fraction of fiber

K_{wf} = weight fraction of fiber

K_{wr} = weight fraction of resin

D_f = density of fiber

D_r = density of resin

Density measurements of both neat resins and composite materials were made using the water immersion technique as described in ASTM D 792-66. The equation used for calculating the density (D) is as follows:

$$D = \frac{W_a \times D_w}{W_a + W_b - W_{bs}} \qquad (2)$$

W_a = weight of sample air

W_{bs} = weight of basket and sample in water

W_b = weight of basket in water

D_w = density of water at test temperature

The water density at the test temperature of 70° F was taken from Reference 24.

Resin samples were in the form of short cylinders weighting about 3 to 4 g. Composite samples were rectangular in shape and weighed about 1 g.

No measurements of fiber density were made. The fiber density value provided by the vendor was used in this study.

The void content of composite samples were determined by computing differences between the theoretical specific volumes calculated on the basis of the measured fiber contents and the specific volumes as measured by

the water immersion technique. The void fraction was calculated using the following equation:

$$K_v = \frac{K_{vf1} - K_{vf2}}{K_{vf1}} \qquad (3)$$

K_v = void fraction

K_{vf1} = specific volume from density measurement

K_{vf2} = specific volume from acid digestion

Bending moduli and flexural strengths of the composites were measured using a three point bend test fixture. The fixture had a 4 inch span. The loading pin and supports were 0.25 inch (0.635 cm) in diameter. A dial gage was positioned against the specimen surface, directly opposite the loading pin, to measure the beam deflection. The test was conducted using an Instron Universal Test Machine and a crosshead speed calculated to produce an initial strain rate of 0.05 per minute in the outer fibers of the composite. Load and time were recorded on an X-Y recorder. Deflection measurements were taken incrementally by stopping the machine at various loads and recording the resultant deflection. When the specimens were tested to failure, the test was run continuously and no deflection measurements were recorded.

CHAPTER IV

EXPERIMENTAL RESULTS

IV-1. Resin Tension Test Results

Testing procedure which was planned was one of the imposing small tensile stains on the test pieces (less than 1 percent) and measuring initial moduli and Poisson's ratios. When these measurements were completed, the specimens would be tested to failure in order to obtain the complete engineering stress strain curve for each resin. The two resins with higher moduli (P-1700 and 930) continually failed prematurely and the fracture surface always coincided with the end of the strain gage backing. Figure 8 shows a typical failure in the P-1700 resin tensile specimen. The fracture surfaces were examined by means of optical microscopy and electron beam microscopy. There is no evidence of polymer damage due to adhesive attack nor does it appear that the fracture emanated from a point. It appears that the fracture initiated all along the bottom face of the specimen. In view of the lack of visible adhesive induced resin surface damage, it was concluded that the adhesive-strain gage backing behaved as an external

reinforcement and produced a stress concentration at the ends of the strain gage backing.

Because of this behavior, the stress-strain curves for all the resin specimens were obtained by measuring strains with a clip-on extensometer. The extensometer was calibrated with a CSI Templex Calibrator, Model CS28A-052.

The measured mechanical properties are presented in Table 3 along with the calculated shear modulus. The shear modulus (G) was calculated from:

$$G = \frac{E}{2\ (1 + \nu)} \qquad (4)$$

E = Young's modulus

ν = Poisson's ratio

The Young's modulus was taken to be the initial modulus or the tangent to the stress strain curve at the low strain end.

The stress-strain curves for the four resins are shown in Figure 9. The yield point is defined as the initial point on the stress-strain curves where the slope is zero. The curves for the 930 resin and the P-1700 resin are classical examples of brittle and ductile resins respectively. The 930 resin shows slight nonlinearity near the point of failure in the stress-strain curve. The P-1700 stress-strain curve does not really indicate the true ductility of this resin. The

fracture occurred after localized necking occurred. This necking occurred in a shear mode as is shown in Figure 10. Measurements of the dimensions of the specimens at the plan of fracture show that a reduction in area of about 34 percent had occurred at the time of failure. Since this is a localized reduction, it is not reflected in the stress-strain trace.

The general structures of the four polymers are reflected in their respective tensile stress-strain curves. The linear relationship and low strain to failure exhibited by the 930 data are typical of a highly crosslinked polymer containing a large number of immobilizing aromatic rings in its backbone. The data representing the linear P-1700 polymer indicates a strong polymer with ductility resulting from the uncrosslinked chains sliding over one another. The flexibilized polymers with the long coiled and folded chains and relatively greater distance between chains are characterized by low moduli, low yield strengths and high elongation to yield and fracture. The lower crosslink density of the 956 polymer in comparison to that of the 840 polymer is reflected in the lower modulus and greater elongation to yield and failure.

IV-2. Results of Intralaminar Shear Tests

The intralaminar shear properties for each of the four composite combinations are presented in Table 4. The shear stress-strain curves for the four composites are shown in Figure 11. None of the composites that were tested produced linear stress-strain curves. The failure strains of the 956 composites were estimated because some of the strain gages in the rosettes were overstrained and failed just before the specimen fractured. The procedure for estimating was that of extrapolating the output of each of the strain gages to the fracture point and using these values to calculate the strain.

The Celion 6000 fiber shear modulus was calculated using the measured matrix and composite shear moduli in the following constitutive equation [25]:

$$G_{\ell} = \frac{G_m}{1 - K_{fv}\left(1 - \frac{G_m}{G_f}\right)} \qquad (5)$$

G_{ℓ} = laminate shear modulus

G_m = matrix shear modulus

G_f = fiber shear modulus

K_{fv} = fiber volumetric fraction

The calculated fiber shear modulus is 1.5×10^6 psi $\pm$ 0.2×10^6 psi (10.0 GN/m^2 $\pm$ 1.4 GN/m^2). This is a reasonable value when it is compared with values

measured by ultrasonic methods [26] and other calculated values [27].

SEM examination of the fracture surfaces revealed two significant points. The first is that there was very little, if any, chemical bonding at the interface of the P-1700 matrix and the Celion fiber (Figure 12(a)). The second point is that the fracture surface features verify that the specimen fracture is one of shear. The inclined lips, saw-toothed in shape, can be seen in Figure 12(b). All the matrix resins sustained ductile shear failure during the 10° off-axis testing.

The intralaminar shear properties, which are a measure of the shearing between fibers within the plies, are identical to the interlaminar shear properties which involve shearing between the plies.

IV-3. Resin Compression Test Results

In general, the moduli and yield strengths measured for each of the resins studied were greater in compression than in tension. The initial moduli were slightly higher in magnitude but the compressive yield strengths were as great as twice the value as measured under tension. The yield strains for tension and compression were not equivalent for all the resins. Engineering stress values and corresponding moduli measured by compression testing are presented in Table 5.

Pieces of Teflon film, measuring 0.003 inch (0.008 cm) in thickness were placed between the sample ends and the compressing surfaces of the test machine to reduce the constraining effect of the compressing surfaces on the ends of the specimens. When testing was carried out without the Teflon film, it was found that there was no effect on the measured yield strengths. There was, however, a lower fracture strength when the Teflon film was omitted from the test. Figure 13 shows the compressive stress-strain traces for each of the resins. The P-1700 resin was the only resin which did not fracture. It sustained a reduction in specimen length to a length equal to about 25 percent of the original length. The tests were stopped at this time because it appeared that no fracturing would occur.

Figure 14 is typical of the compressive fracture modes for the three epoxy resins. The fractures were longitudinal and fibrous in appearance. The 930 resin sustained a significant amount of compressive strain prior to fracture. This can be interpreted as an indication of a low fracture toughness for this polymer since the measured tensile strain was significantly lower.

IV-4. Resin Densities

Resin densities are presented in Table 6. It is evident from the values in the table that there is very little spread in the measured values. The measured values agree quite well with the published densities of 1.24 g/cm^3 for P-1700 and 1.36 g/cm^3 for the Fiberite 903 resin [25,26]. These data strongly reflect the structure characteristics of the flexibilized polymers. The long, coiled and folded chains which force the molecules of the cured system further apart than they would normally be, have produced cured polymers with substantially reduced densities.

IV-5. Resin Relaxation Test Results

Plots of logarithm E/E_o versus time for each of the resins are presented in Figure 15. E is the instantaneous Young's modulus of the resin. E_o is the initial modulus of the resin, as calculated from the load and strain existing in the test specimen at the onset of the relaxation test. The curves for the 930 and P-1700 resins appear to be linear over almost a three decade time interval. Table 7 presents the test data and the T_G for each of the four resins. The flexibilized resins, because of the freedom of movement of the long chains, relax more quickly than the 930 and

P-1700 polymers. Because of the low T_G values for these flexibilized resins, the curves are not linear and indicate more than one relaxation mechanism exists.

Monitoring of the strain gages during the tests showed that there was no grip slippage or other occurrences which might have allowed the strain level to change during the testing. All strains remained constant.

IV-6. Dynamic Mechanical Analysis Results

Dynamic shear moduli of the neat resins were measured as functions of temperature, frequency and maximum strain. The temperature scan was measured to determine the dynamic T_G of each of the resins under study. The frequency scan, which can be converted to a strain rate scan, was measured to obtain information about the response of each resin to strain rates so that the resins could be evaluated at those strain rates which they would experience under the impact conditions of this study. The lower limit of the strain rate range was established to include the strain rate of 0.05 per minute, which was used in the "static" mechanical properties tests in this investigation. The frequency of 0.0132 rad/sec was calculated as that frequency which produces this strain rate. The maximum calculated strain rate measured 3820 per minute at 100 rad/sec.

The maximum strain scans were conducted to measure changes in the moduli along the stress-strain curve The composites were tested under variable temperature and strain rate conditions only.

Table 8 presents the T_G values for each of the four resins studies at strain rates of 0.5 rad/sec and 6.28 rad/sec. Figure 16 is a typical plot of the data produced by a temperature scan at a strain rate of 0.1 rad/sec. The glass transition temperature, as defined by Nielson [27], is that temperature at which the loss modulus, G", is at its maximum value. This transition is specified by Nielson to be measured at low strain rates. The T_G values for the four composites are also presented in Table 8. The strain rates at which these values were measured was also 0.1 rad/sec and 6.28 rad/sec.

Figure 16 shows plots of G', G", and tangent delta as functions of temperature for the 930 resin. Figure 17 shows the same relationships for the 930/Celion composite. The addition of the fibers to the resin has broadened the G" and tangent delta peaks slightly and also shifted these two peaks to the higher temperatures. Figure 18 shows a temperature scan for one of the flexibilized neat resin specimens (840). In contrast to the highly crosslinked 930 resin, the G" peak for the 840 resin does not have a very pronounced peak

and has a very slight rise as the temperature increases. The tan delta peak is broad and also not as great in amplitude as the peak for the 930 resin. This is due to the flexibilizer which probably increases the range of molecular weights in the flexibilized resin over that of the unflexibilized resin. The range of molecular weights in the 930 resin is probably narrower than that of the 840 resin.

Neat resin frequency scans were run at ambient test temperatures and ranged from 21.7° to 23.4° C. Table 9 presents the values of G' and G" at five different frequencies for each of the four resins tested. Also listed are the calculated values of Young's modulus using measured values of Poisson's ration using Equation (4). Table 9 also includes G' and G" values which were measured using the composite samples. Table 10 presents the data obtained from measuring the dynamic moduli of each of the resin specimens at different maximum strains. When the maximum test strain was increased to 1 percent, the stored modulus decreased at the higher test frequencies for the 840 and 956 resins. It was believed that this was due to the generation of heat within the sample at a rate in excess of the heat transfer rate out of the samples. Thermocouples were bonded to the outer edge of the samples and the sample

surface temperature were monitored with a digital temperature indicator. The maximum temperature rises measured during the frequency scans for the 930, P-1700, 840, and 956 resins were 5.4°, 9°, 25°, and 12.1° F (3°, 5°, 14°, and 7° C) respectively.

The results of the dynamic testing reflect the chemical structure of the four resins. The high strain rate sensitivity of the 840 and 956 resins is due to the long folded chain structure which allows movement of the chains over one another. This results in the formation of heat due to internal friction. The 930 resin, being tightly crosslinked exhibits a low loss modulus and less internal friction.

IV-7. Thermal Mechanical Analysis Results

Thermal mechanical analysis (TMA) of the neat resin samples and the unidirectional and cross ply composites provided thermal expansion information and T_G values for all of the samples. The cross ply (0°/90°) specimens were cut from the falling weight impact test specimens. The unidirectional composite test specimens were cut from the double cantilever beam fracture test specimen.

Figure 19 shows traces of displacement as a function of temperature for the 930 resin and the P-1700 resin. Figure 20 shows the same type of traces for the

840 and 956 resins. The T_G values determined from the initial inflection in the displacement-temperature slope are indicated on the figures. The slopes of the curves at temperature below T_G were used with the sample thickness to calculate the resin coefficients of thermal expansion. The values along with the T_G values and curing or molding temperatures are presented in Table 11.

As previously stated, TMA was conducted on two different composite layups, The 0° unidirectional fiber orientation and also cross ply construction with 0°/90° fiber orientation. Thermal expansion measurements were taken in the specimen lengthwise direction, across the thickness of the specimen, and for the unidirectional specimens, across the width of the samples. Tables 12 and 13 present the data acquired from the TMA work. The measurement directions for the two types of composite constructions are shown on the tables.

The coefficients of thermal expansion were calculated from the slope of the displacement-temperature curve up to the composite T_G and the sample dimension across which the expansion measurements were made. Figure 21 shows a typical composite TMA plot. The transition is not as sharp for the composite specimen as it is for the neat resin specimen. This made it difficult to measure the T_G for some of the composites.

IV-8. Neat Resin Impact Test Results

Two specimens of each of the neat resins being studied were impacted with the instrumented drop weight impact tester. Figure 22 shows graphical representations of the results of these tests. The impacting forces and energies are shown as a function of deflection for the impacts. Table 14 presents that data from these tests. All neat resin panels were tested under equivalent impact conditions. Impacting velocity was controlled at about 8.0 ft/sec (244 cm/sec).

The load traces in the above figures indicate a very brittle response for resins 930, 940, and 956. In Figure 22 this is indicated by a linear increase in load with an increase indeflection and then an almost instantaneous drop in load to a value of zero. All three had similar failure modes of a star fracture under the impact point. This fracture appears to have propagated until the material failed from a circumferential fracture at about 1-1/2 inch (3.81 cm) radius from the impact point. Figures 23 and 24 show the impacted specimens of these three resins. The outer 0.5 inch (1.27 cm) band along the perimeter of each specimen is the specimen surface that was clamped by the holder during the impacting test. In contrast to the failure mode of these three resins, Figure 24(b) shows the impacted P-1700 resin sample. This resin was able to

absorb all of the available energy [30 ft-lb (41 J)]) with no through penetration. The damage was a permanent deformation on a 0.5 inch (1.27 cm) diameter hemisphere at the point of impact. It appears that, given enough energy, the panel would fail by elongation of the hemisphere until complete shearing occurs. These visual observations are reflected in the load-deflection curve in Figure 22(b). No abrupt drop in load, which occurred during the epoxy resin impact tests, is evident in Figure 12(b).

IV-9. Unidirectional Composite Impact Test Results

The unidirectional composite impact tests can be generally described as dynamic three point flexure tests. Impact damage was contained within a central strip of the impacted composite. The widths of the damaged strips and the lengths of the damage along the strips varied depending on the type of composite being tested and the fiber content.

Basically, two different types of impact damage occurred. One type is shown in Figure 25(a). This damage results from interfiber splitting of the composite parallel to the axis of the fibers and fiber fracture across the fibers. The number of interfiber cracks is usually three. There is usually a central crack, and two outer cracks which separate the damaged composite

from the rest of the composite. Parts of the damaged composite strips are sometimes completely separated from the specimen during impact. The second type of damage also produced at least three interfiber cracks, but no complete fiber fracture across the fibers. The penetrator wedges through the central crack, spreading it apart and twisting the material on both sides of the crack. Compression failure of the surface fibers on the impacted side of the laminate can be seen (see Figure 25(b)) and no surface fiber damage (breakage across the fibers) can be observed on the opposite surface. Some composites exhibit a combination of both types of damage. The load-deflection curves for these two types of damage are shown in Figures 26(a) and (b).

The second type of damage, which produced a splitting and wedging apart of the central crack, did not produce any internal damage in the composite. The absence of appreciable damage is observable by utilizing ultrasonic C-scan examination of the impacted specimens (Figure 27). The splitting and fracture damage did not produce any significant damage outside of the area of the fractured central strip.

Microscopic examination of the damaged area produced by the wedging penetration action of the impactor is shown in Figure 28. The area immediately under the

point of impact does contain some delaminations and the compression failure of the surface plies are evident.

The loads at initiation of damage, P_i, maximum loads, P_m, and the energies at initiation of damage, Q_i, at maximum load, Q_m, and total energies, Q_t, are presented in Tables 15 and 17.

IV-10. Results of Crossply Impact Tests

The crossply (0°/90°) laminates were impact tested using two different test conditions. Thirteen through-penetration tests were conducted at an impacting velocity of 8 ft (244 cm/sec). The impactor completely penetrated each of the laminated specimens. A load-deflection curve and an energy-deflection curve was recorded for each of the specimens tested. All the specimens which were tested were built up from fifteen prepreg plies, but the specimen thickness and fiber volume contents varied between specimens. The second test plan utilized the impacting of composite specimens at a constant drop weight energy level which would reach the maximum loading point of the most impact resistant composite system, but not fully penetrate it. This energy level was determined from the results of the through-penetration tests. Two of these tests were conducted on each of the graphite/resin laminate systems

used in this study. The number of prepreg plies used to build up the laminates was 30.

The results of the second type of testing (damage initiation) will be presented first because they give a clear, graphic picture of the damage initiation processes and also they contribute significantly to the interpretation of the load-deflection curves generated during the through-penetration tests.

The energy level or these tests was controlled by selecting the drop height to produce an impacting velocity of about 3.3 ft (100.6 cm) per second. Table 19 presents the load data from these tests and the through penetration tests in terms of load at inception of damage (P_i), maximum load (P_m), and plate deflections. The damage initiation specimens are denoted by asterisks. Using load at initiation of failure as a basis for evaluating impact resistance, the composite systems, subject to 31 ft-lb (42 J) of impact energy, rank in the following order: 930 > 840 > 956 > P-1700.[2]

Figure 29 shows load-deflection and energy-deflection curves generated during the impact of each of the four different laminates. Specimen loading is

---

[2]Throughout this paper the composites will be identified by their matrix designation. For example the Celion 6000/930 composite will be referred to by "930 composite".

denoted by an initial smooth, continuous load-deflection curve. Initial specimen damage is considered to occur at the point on the curve where a decrease in slope occurs (Point A). Each of the four types of composites, whose impact histories are shown in Figure 29, appear to have sustained damage prior to reaching the maximum load (Point B). The load-deflection curves for the 930 and P-1700 composites indicate one change in slope prior to reaching the maximum loading points. The same curves for the 840 and 956 composites show two changes in slope as the load increases to a maximum. It is apparent from Figure 29 that the maximum loads were reached and through penetration occurred for the P-1700 and 840 composites. One cannot determine from the figure how near to the maximum loading point the 930 and 956 composites were after absorbing 31 ft-lb (42 J) of impact energy.

It is of interest to examine the energy-deflection curves of the four types of composites. The four curves are characterized by an initial upward concavity to a deflection of about 0.17 inch (0.43 cm) where the slope becomes linear. The greatest amount of the energy absorbed by these composites was absorbed after they were deflected 0.17 inch (0.43 cm).

Photographs of the impacted specimen surfaces are presented in Figures 30 to 33. Figure 30 shows the impacted surface and the backside surface of one of the

930 composite specimens. No damage is observable on the impacted surface other than the penetrator indentation mark which measures 0.197 inch (0.500 cm) in diameter. No broken fibers or cracked resin are observable by microscopic examination of the surface of the crater caused by the penetrator. The backside surface shows no breakage or longitudinal splitting between the surface fibers and no delamination of the surface lamina. The "warm-tracks" in Figure 30 appear to be minute depressions caused by the surface gasses which were emitted from the mold during the curing of the composite.

In Figures 31 to 33 which show the surfaces of the P-1700/Celion, 840/Celion, and 956/Celion specimens respectively, the surface features are totally different. In addition to the hole or indentations caused by the penetrator, each of the three impacted surfaces show damage from compressive failure. This is indicated by two thin lines radiating out from the impact-induced crater. The lines are indicated by arrows in the figure. One of the lines is perpendicular to the surface fiber orientation and the other is parallel to it. The failure line perpendicular to the fiber direction is caused by a kinking of the surface fibers out of the plane of the surface lamina. The other line is an intra laminar crack, running between the surface fibers. The lengths of the kink line measures 1 inch (2.54 cm),

1.25 inch (3.18 cm), and 2.375 inch (6.03 cm) for the P-1700, 840, and 956 composites respectively. The backsides show various degrees of surface lamina delamination and interfiber cracking.

Figure 34 shows the through transmission ultrasonic C-scans of the four types of composite laminates after impact. One can see the extent of damage in the impact area. It is evident from these figures that the internal damage extends a significant distance away from the center of the impact site. It appears that the damage is due mainly to delamination within the laminate. One other point to be made from these figures is that the lengths of the two axes of the ellipsoid or diamond shaped damage area of the 956 laminate are very close to the lengths of the compressive failure lines on the impacted face of the impacted specimens. This is also true for the 840 and P-1700 impact specimens. The 930 laminate showed no evidence of compressive failure away from the impact site.

By slicing through the damaged area of all four types of specimen, the interior damaged structure of each specimen was exposed for examination. All four types of composites exhibited compressive failure starting at the impacted surface in the volume of the composites deformed by the spherical penetrator. The extensive damage incurred by the P-1700 composite completely

obliterated any signs of compressive failure initiation under the impact crater; however, compressive failure lines, radiating out from the damage area infer compressive damage initiation under the point of impact. Figures 35 and 36 show classical composite shear type compressive failure for the 930 and 956 composites. It is apparent in Figure 35, which shows the area of the 930 specimen directly under the impact point, that the compressive failure extends almost through the entire thickness of the damaged volume. Also, the back surface shows no evidence of flexural tensile failure. In Figure 36, which shows the compressive failure crack for the 840 specimen, one can see the delamination crack which emanates from the end of the compressively induced crack.

The through penetration tests of the fifteen ply cross-plied impact specimens produced diamond shaped failures on the back face of the specimens with varying amounts of surface ply delamination, also on the back face. Load-deflection-energy responses through initial failure were in general similar to those of the previously described "limited impact energy" test specimens. Figures 37 and 38 show the condition of each of the four types of composite specimens after through-penetration. Except for the P-1700 composites, all composites exhibit some extent of backside delamination, with the amount of

delamination greatest for the 930 composites and least for the 956 composites. The measured data, and the normalized data from the through penetration tests are presented in Tables 19 to 22 with data for the constant impact energy test data. The compressive failure lines on the impacted surfaces are less distinguishable for the thinner through-penetration specimens than they are for the limited-energy impact specimens. They do not extend as far from the center of the impact-damaged area.

Ultrasonic through-transmission C-scanning of the impacted, thinner (15 ply) specimens shows that the internal damage is contained within the visible surface damage area of the specimens (Figure 39). Also, there is not the variation in the extent of damage area between different composites as there is in the thicker impacted specimens.

Sections through the damaged areas of the thinner specimens are shown in Figures 40 and 41. Except for the P-1700 composites, multiple delaminations are present throughout the damage zones.

IV-11. Results of Neat Resin Fracture Toughness Tests

The measured dimensional and load values from the fracture toughness tests of compact tensile specimens were converted to K_q values by use of the following equation.

$$K_q = (Pq/BW^{1/2}) - f\ (a/w) \qquad (6)$$

P_q = load determined as instructed in ANSI/ASTM E399-78

B = specimen thickness

W = specimen width

a = crack length

f(w) is taken from 9.1.4.1 in ANSI/ASTM E399-78

The load displacement curves for the 930, P-1700, and 840 resins were Type III curves as described in ANSI/ASTM E399-78. The load displacement curves for the 956 resin were Type I curves. The determination of P_q and the validation of K_q as actual K_{IC} values were also done as outlined in ANSI/ASTM E399-78.

G_{IC} values were calculated from the expression;

$$G_{IC} = \frac{K_{IC}^2\ (1 - \nu^2)}{E} \qquad (7)$$

E = Resin modulus

ν = Poisson's Ratio

B, W and a are defined in Equation (6). P_{max} is the maximum load measured during the test. Clip gage displacement measurements were transformed into load line displacement values to obtain normalized compliance values using Newman's modified boundary collection techniques [30].

Data from these fracture toughness tests are presented in Table 23.

IV-12. Results of Composite Fracture Toughness Tests

The data measured herein were by two different testing procedures. One method was to load the specimen continuously and record the load at the time the crack tip reached a specific index mark on the side of the specimen. The second procedure was to load the specimen until the crack tip reached a specific index mark and then to unload the specimen completely. This cycle was then repeated until the required number of data points had been reached. It was found that there was some hysteresis indicating that some of the energy was not recoverable by the crack growth; however, the differences in fracture toughness data measured by these two different methods were insignificant in comparison to the experimental data scatter.

The data from these tests are presented in Table 24. The data scatter within the group of data from a single beam for different lengths of cracks is relatively large (about 20 percent for G_{IC} values less than one and less for the larger values). This could be due to inaccuracies in measuring crack lengths, loads, or inherent in the assumption that all the strain energy is transferred into crack growth.

CHAPTER V

COMPOSITE CONSTITUENT EFFECTS AND INTERACTIONS

V-1. Polymer Structural Effects

It was found that the matrix structure was a very important factor in composite response to low velocity impact. Wide ranges of matrix resin mechanical properties, among the four matrix resins studied, were attained by using four resins with different structural characteristics. One resin was a high crosslink density epoxy having a highly aromatic backbone. Two other epoxy matrices with flexibilized backbones and low crosslink densities were also studied. Another resin, which was a linear polysulfone, contained a rigid, aromatic backbone structure with no crosslinking.

The polymer structures are reflected in the polymer properties. The polymers with the stiff aromatic backbones possess high strengths and moduli in tension, compression and shear. Also, dynamic modulus data for these materials indicate nominally moderate strain rate sensitivity. The moderate relaxation characteristics of these resins were confirmed by experiment.

If one compares the two polymers with rigid backbones, one can observe that the strain to fracture is

low for the highly crosslinked resin because the high crosslink density restricts the backbone chains from moving in relation to neighboring chains. Since there is no flexibility in the backbone, relative movements of the chains before polymer bonds fracture are limited to very small distances. The absence of bonding in the linear polymer is reflected in its high strain to failure. The sliding of the uncrosslinked chains past one another only results in the breaking of secondary Van der Waals or hydrogen bonds (intermolecular forces).

The flexibilized resins can be imagined as a network of loose coils and loops which are separated from each other by a sufficient distance to allow free movement of the lightly crosslinked structure under imposed loads. The chains are not rigid and the crosslink density is not great in relation to that of the highly crosslinked epoxy resin. Because of the intertwining of the loops and coils, when a load is imposed on the polymer, the coils and loops can move to straighten out. This movement is time dependent, however, because of resistance from neighboring chain loops. Since these chains are not rigidly connected together, the high strengths and moduli in tension, shear, and compression are rather low. Because of the uncoiling of the folded chains, the strain to fracture can be rather high and also the strain rate sensitivity is of a significant

magnitude. Relaxation times are very low. The addition of the polyol flexibilizer to an unflexibilized polymer produces a new polymer with a T_G lower than the parent polymer. Measurements made during this study indicated that the loose chain structure of the flexibilized resins also results in a decrease in the resin density and also a significant increase in the resin thermal expansion coefficient.

The effect of the polymer structures on their respective graphite fiber reinforced composites can be rationalized, in part, from the polymer properties. The matrix dominated properties such as interlaminar shear, transverse tensile, compression, etc. are highest for the heavily crosslinked epoxy and lowest for the flexibilized epoxies. The linear, uncrosslinked resin, P-1700, is unique in that its high neat resin mechanical properties are not translated into high matrix dominated mechanical properties because of the lack of functional groups along the chains which would possibly chemically bond with the fiber surface to produce strong interfacial bonds. This reduction in interfacial bonding with the P-1700 as a matrix can allow the crossplied composite impact damage mechanism to be one of interlaminar shear.

The increase in the polymer thermal expansion coefficient due to the flexibilized polymer structure

does result in larger residual strains resulting from cooling of the cured composite from the processing temperature than one would observe in a highly crosslinked matrix composite.

It was found that neat resin and composite physical and mechanical properties reflect the polymer structure. The structural differences between the polymers used in this study include backbone structure and crosslinking density. A tightly crosslinked epoxy polymer with a rigid backbone structure, typical of polymers commonly used in graphite fiber reinforced composite structure, was included for study as a reference against which the other resins were assessed. This polymer exhibits a high modulus, a high strength, a low strain to failure, and a moderate strain rate sensitivity. The polymers with a decreased amount of crosslinking and flexibilized chains were found to be tougher resins (as assessed by the impact tests) than the highly crosslinked epoxy. This was due to the increase in the strain to yield which resulted from the loosening of the crosslink density and intrachain constraints. This increase in resin toughness did not translate into an increase in composite toughness because of the resulting decrease in moduli and strength properties which also was a consequence of the types of structural changes described above. The decrease in modulus and strength

properties resulted in failure mechanisms dependent on matrix properties to occur before the potential maximum impact loading was attained. This then resulted in an increase in impact energy absorption which is gained at the expense of increasing internal damage propagation.

The importance of fiber/matrix bonding has been illustrated with composites made with the linear polymer as a matrix. There is no chemical bonding between the polymer chains and the fiber surface active sites because of the absence of reactive functional groups along the lengths of the backbone chains of the linear polymer. Fiber/polymer interactions are either mechanical in nature, and/or are due to Van der Waals forces or hydrogen bonding. This lack of a strong interfacial bond results in low matrix dependent composite properties (transverse tensile, interlaminar shear, etc.) and unexpectedly low composite impact resistance.

The impact behavior displayed by the matrices with the more flexible structures is acceptable for containment structures which are designed to absorb energy before total failure occurs. The failure mechanisms exhibited by composites with these matrices are undesirable for structures that are subject to impact and must not sustain internal or hidden damage.

Polymer toughness (impact resistance) appears to increase with increasing polymer strain to yield or

fracture because of the resultant increase of the membrane action of the impacted plate. However, in graphite fiber reinforced composite materials the magnitude of the diaphragm action during impact is dependent on the fiber properties. In order to attain maximum loading during impact, polymer controlled failure mechanisms must be repressed by maintaining polymer strength and modulus values at or above critical values. From the results of this study it appears that the modulus and strength of the polymers are related to the polymer backbone structure. It has been shown [31] that the modulus and strength of an epoxy resin is dependent on the backbone cohesive energy and not crosslink density. In order to maintain high levels of strength and modulus values and to increase the strain capability, the flexibility must be introduced through the backbone structure or in the crosslinkers.

In order to retain strength and stiffness in the polymer, the use of flexibilizers seems to be unacceptable. It may be that decreasing the crosslink density or flexibilizing the crosslinkers may enhance the resin toughness and also improve the composite toughness. The linear thermoplastic polymers have always shown promising potential as matrices for tougher composites, but the potential has seldom been attained. It may be that slight backbone structural alterations, a fiber sizing,

or an additive to the linear polymer may be feasible as a way of enhancing the fiber/polymer interfacial bond efficiency. This may then allow these polymers to reach their potential as effective, tough composite matrices.

V-2. Composite Residual Stresses

Composite residual stresses, due to resin volume changes during curing, differences in matrix and fiber thermal expansion coefficients (TEC) and the cooling of the composite from its processing temperature to room temperature, could have an effect on the composite toughness. Thermal expansion coefficients of the resins and their corresponding unidirectional and crossplied composites were measured to estimate the magnitude of the composite residual stress. The TEC's for the Celion 6000 fiber have not been measured. It is known that the longitudinal TEC is slightly negative (-0.3×10^{-6} °C^{-1}) and the transverse TEC is slightly positive ($\sim 3.0 \times 10^{-6}$ °C^{-1}). The neat resin and unidirectional composite TEC data were used with Rule of Mixtures relationships developed by Schapery [32] to calculate the longitudinal and transverse TEC's for the Celion 6000 fiber. The transverse TEC values ranged from $+5.5 \times 10^{-6}$ °C^{-1} to -1.5×10^{-6} °C^{-1}. Both values can be taken as zero without introducing any significant errors in residual stress calculations.

The radial stress around a fiber in a matrix, σ_R, is given by the following relationship:

$$\sigma_R = \frac{(\alpha_m - \alpha_f)\ (\Delta T)\ (E_m)}{(1 + \nu_m) + (K_{\nu f})\ (E_m/E_f)} \tag{8}$$

α_m = matrix TEC

α_f = fiber TEC

subscript m = matrix property

subscript f = fiber property

T = temperature

For graphite fiber reinforcement, E_m/E_f is small so it can be omitted. The values for ν for each of the resins are about the same. With α_f taken as zero, the radial stress, σ_r, is related to the matrix properties as follows:

$$\sigma_r \approx \alpha_m\ \Delta T\ E_m, \tag{9}$$

The strains, ε_r, are then related to the resin properties by: ε

$$\varepsilon_r \approx \alpha_m\ \Delta T \tag{10}$$

The residual strains vary by about 3 to 1 for the highest and lowest strain matrices. The expression above does not account for interactions between neighboring fibers. The calculated radial compression stresses range from 600 psi (4.14 MN/m^2) to 3770 psi (26.0 MN/m^2) for the 956 resin and the P-1700 resin, respectively.

The interlaminar stress can be estimated from the TEC's of the crossplied and unidirectional composites.

Daniel [34] and Pagano [35] have shown that the thermal strains due to differences in fiber orientations in a composite are equal to the difference between the free expansion and the constrained expansion of a ply. The free expansion can be taken from the TEC values in the Y and X direction of Table 13. The restrained value can be taken as the X direction TEC in Table 12. The difference in the two values times the ΔT can then be taken as the strain due to restraint of the crossplies. Since the fiber axial modulus is so much greater than the modulus of the matrix, the strain is taken up in the transverse direction of the composite. When one calculates Kies strain magnification to estimate the matrix strains due to the constraint of the cross ply composite design, for a hexagonal fiber packing array, the tensile strains in the 930, 956, and 940 matrices are about the same with a value of 0.0007. The strains in the P-1700 matrix is about double that of the other three matrices.

Because of the relatively large TEC's of the flexibilized resins, there are no great differences in estimated residual strains between the three epoxy resins in either the unidirectional or the crossplied composites. Due to its high processing temperature, the linear P-1700 matrix does experience significantly larger strains than the three epoxies. The residual strains are transverse tensile strains and all are well below

the level which would result in matrix cracking. No transverse cracks were observed on a microscopic level.

Relaxation test data have shown that the 840 and 956 resins relax rapidly. It is highly probable that the small residual stresses, caused by differences in TEC's and differences between processing temperatures and normal ambient temperature, would almost completely disappear by relaxation. By similar reasoning, it would be expected that residual stresses were present in the 930 and P-1700 composites during all testing.

Another source of residual stresses in a composite is the change in volume of the monomer/hardener mixture as it polymerizes. Polymerization volume changes of the four resin systems studied were estimated from calculated monomer/hardener densities, using the Law of Mixtures and measured cured polymer densities. The 930 and 840 systems underwent a volume decrease of about 2.7 percent. The 956 system decreased in volume by about 4.1 percent. Since all three of the epoxy systems were processed at a temperature of at least 50° C above their T_G's, it would be expected that the residual stresses caused by the resin shrinkage would relax out almost instantaneously as the resins cured. In line with this reasoning, it is assumed that no residual stress contributors from resin shrinkage are present in the processed composites.

The point to be made from this evaluation of residual stresses is that there are no unusual or extreme strain states set up in any of the composite materials which could be rationalized as having significant effects on their impact behavior.

V-3. Resin-Matrix Structural Differences

Changes in polymer properties from the introduction of a particulate or fibrous second phase into the bulk polymer have been observed as an upward shift in the glass transition temperature of the polymer and also as a suppression of the polymer dampening mechanisms. In order for these changes to occur, either the proposed bonding of the polymer functional groups with the graphite surface groups has an effect on the crosslinking within the bulk of the matrix itself, or the ratio of surface area bonds to polymer crosslinks is of such a magnitude that the in-situ structure is altered [19].

For this study, interactions between the fibers and the polymers were compared by noting the magnitude of the upward shift of the T_G and the relative suppression of the damping mechanism (loss modulus) for the four fiber-resin composite systems.

If the interaction between the polymer matrix and the fiber were solely chemical in nature, the relative

density of functional groups on the chain of each polymer may correlate with the relative magnitude of T_G shift in each corresponding composite system. The polymer with the most functional groups may experience the greatest shift of T_G when processed into a composite with graphite fibers. However, the number of active surface groups on the fiber may be the controlling factor and no difference in T_G shifts may be observed with changes in matrices. When considering the polysulfone structure, where no functional groups are available for interaction with fiber, there should be no T_G shift in either of the above cases.

Investigators who have used DMA to study resins and composites associate the damping peak with the partial loosening of the polymer structure, so that groups and small chain segments can move. At low frequencies, this occurs near T_G. This loosening of the polymer structure also results in a change in the thermal expansion coefficient of the bulk resin and its corresponding composite. This can be measured by TMA. Both DMA and TMA were used to measure T_G for each of the resins. Only DMA was used to measure composite T_G's because the TMA data did not produce thermal expansion transitions which were sharp enough to be used accurately in determining the T_G values for the composites.

Nielson [30] states that the G" curve, generated by the DMA instrumentation, goes through its maximum at a slightly lower temperature than the peak of the damping (tan δ) curve, and that the damping curve peak occurs at a temperature 9° F (5° C) to 27° F (15° C) above that measured using TMA instrumentation. Data from both methods are presented in Tables 8 and 11. In Table 8, two T_G values are listed for each of the bulk resins and the composites. One value was measured from the G" peak and the other was measured from the damping peak.

From the data in Table 8 it is evident that the P-1700 resin does not produce a G" curve which peaks out at a lower temperature than the damping curve. Both curves appear to peak out at the same temperature. The P-1700 is a linear polymer with no crosslinking in its structure. The crosslinked epoxy resins do produce G" curves which peak out slightly above the tangent delta curve. The data in this table does not indicate a relationship between peak differences and crosslink density.

When one compares the T_G values for the resins in Table 8 with those in Table 11, one can see that the damping peaks from DMA indicate lower T_G's for the 930, 840, and 956 resins than the data measured by TMA. The P-1700 resin data indicate a higher T_G from DMA tests than the value measured by TMA.

From the data in Table 8 and 11, one is able to compare the bulk resin T_G's with the matrix T_G's. The P-1700 resin and 930 resin differences are negligible. There are significant increases in the matrix T_G over the neat resin T_G from the low frequency modulus measurements of the 840 and 956 specimens. Based on this data, the magnitude of T_G shift is as follows:

$$956 = 840 > 930 \geq \text{P-1700}$$

Scanning electron microscopy of fracture surfaces of the 10° off-axis specimens was used to assess the completeness or effectiveness of the matrix-fiber bond qualitatively for each of the four types of composites. The P-1700 specimen surface is shown in Figure 12(b). Only small traces of matrix material are visible on the exposed fiber surface. This indicates either a very weak bond (Van de Waals or hydrogen) or no bond at all--other than a possible mechanical bond. In contrast, Figure 12(a) shows large amounts of 930 matrix on the surfaces of the exposed fibers. This indicates a significant matrix-fiber bond. Both the 840 and 956 composites show some evidence of bonding but not as much as was observed for the 930 composite. This qualitative assessment of interfacial strength or bonding efficiency does not appear to be in agreement with the DMA data in confirming that the magnitude of the upward shift of

the T_G increases as the matrix-fiber interfacial bond increases.

The absence of bonding found by examining the P-1700 composite fracture surface can be attributed to the absence of functional groups along the polysulfone chain. This has been discussed previously.

The 930 resin polymerizes to produce a highly crosslinked structure because it has a high concentration of functional groups per weight of resin. In contrast, the 840 and 956 resins should have lower crosslink densities than the 930 resin. Their interfacial bonding with the graphite fibers appears to be not as complete as that of the 930 resin. These results indicate the possibility of a relationship between crosslink density matrix fiber interfacial bond strength. These results also indicate that there is no relationship between crosslink density and T_G elevation. The results suggest that the fiber surface active site density does not correlate with the degree of interfacial bonding.

From Table 8 there are some indications that strain rate increases also increase T_G values in the bulk resin and in the matrix resin. It could very well be that a triaxial stress state, due to the thermal changes, is imposed on the matrix during composite testing (DMA and TMA) and can cause this phenomenon.

The magnitude of the stress state would be dependent on the amount of relaxation in the matrix in the time interval between composite processing and composite testing. If no relaxation occurs, no significant residual stresses should be present at T_G. If complete relaxation occurs, then the thermal expansion mismatch between the matrix and the fibers could cause a buildup of stresses within the composite as the specimen is heated. The two resins with the shorter relaxation times (840 and 956) experienced greater T_G elevations than the two resins with the greater relaxation times.

The DMA and TMA data show that differences do exist between the T_G's of the resins in the bulk state and resin matrices. Although the data do indicate that there is no difference between bulk resin and matrix T_G's when no strong matrix-fiber interfacial bond exists, the results of this study imply that there is no relationship between monomer functional group density and T_G change. However, if there is a chemical bonding between the monomer functional groups and fiber active sites, then it is possible that triaxial stresses set up by differences in thermal expansion between the matrix and the fiber, the magnitude of the difference between ambient temperature and the cure temperature and

the degree of matrix relaxation may cause bond distortions which could possibly alter the resin T_G. The depth of this investigation is insufficient to produce any conclusive evidence as to the cause of the T_G shift in some of the composites. It may be that the information and speculations resulting from this study will be of help in planning future studies which are specifically directed toward determining the cause of resin-matrix differences.

CHAPTER VI

IMPACT RESISTANCE ANALYSIS

VI-1. Neat Resin Impact Resistance

VI-1.1. General Observations

One can rank the toughness of the neat resin specimens studied in this program by any of the following bases:

(1) Area under tensile stress-strain curve.

(2) G_{IC} values, determined using compact tensile specimens.

(3) Dropweight impact test results using load to failure and energy absorbed at failure as criteria.

There is no correlation between the ranking based on 1 and those of 2 and 3. The rankings of 2 and 3 are the same, showing the order P-1700 > 956 > 840 > 930.

It would be convenient to know what resin properties significantly influence the neat resin impact test results so that preliminary screening of candidate resins for use in tougher composite structures could be accomplished confidently.

There are three criteria which one can use to assess resin impact toughness. These are (a) load at failure, (b) energy absorbed up to failure, and (c)

extent of damage. The first two can be conveniently measured with the instrumentation of the impact tester. The third can be partially assessed by dimensional measurements of the damaged area, but the extent of damage within the damaged area is assessed only qualitatively by this method.

VI-1.2. Load at Failure

The loads at failure for the four resins studied appear to correlate with the tensile strains at yield. For the 930 resin, which exhibits no tensile yield point, the fracture strain is utilized for correlation. The relationship between load at failure and yield or fracture strain is shown in Figure 42. The load at failure also correlates with the fraction of the load carried by membrane action (Figure 43).

VI-1.3. Energy Absorbed at Fracture

The energy absorbed by the neat resin impact specimens up to the point of failure can also be correlated with the fraction of the specimen load at failure carried by the membrane action of the plate. This is illustrated in Figure 44.

VI-1.4. Membrane Action

At failure, each specimen which was tested experienced a deflection greater than one-half of the specimen

thickness. As the deflection of a clamped plate exceeded about one-half of its thickness, the plate started carrying the load as a direct, in-plane tensile stress. As the amount of membrane action (direct stress) increases, the energy absorbed by the plate increases because the full cross section of the plate is being utilized in sustaining a portion of the total load. The portion of the load supported by membrane action increases as shown by the following empirical equation [37]:

$$K = 1 - \frac{1}{1 + 0.12\ e^2/t^2} \qquad (11)$$

K = fraction of the load carried by diaphragm action

e = deflection

t = specimen thickness

VI-1.5. Damage Area

The resin damage areas do not correlate with any of the resin properties. Three types of damage occurred within the group of four resins that were impacted. The P-1700 specimen was not cracked at all. The damage was only from deformation with three zones apparent by visual examination. These zones have been described previously. The 956 specimen actually exhibited two damage areas. These were a central 0.67 inch (1.7 cm) diameter punched out hole concentric within a 4.2 inch (10.7 cm) diameter circular crack which only extended part way

through the specimen. No signs of shear lips, which would indicate a shear failure, are evident in SEM photographs of the fracture surfaces. The fracture surfaces of the punched hole indicate a brittle tensile fracture. Crack propagation initiating from the punched out hole evidently caused the secondary failure to occur. The other two samples (840 and 930) did not exhibit punched-out central holes, but did exhibit circular damage areas with sharp pie-shaped pieces (Figures 23 and 24).

VI-1.6. Summary

Under the conditions established for this study, the impact resistance of neat resins appears to be dependent on the ability of the impacted plate to withstand enough deflection during impact to allow a significant amount of membrane action to develop in the plate. The maximum amount of deflection that a plate can experience is, in part, dependent on the maximum amount of strain that the material can sustain before failure occurs. Naturally, the loading is also dependent on the polymer tensile modulus and the strain rate.

At the calculated strain rate produced by the drop weight impact tests, the shear moduli increase over the static value was 5, 3, 55, and 56 percent for the 930, P-1700, 840, and 956 resins, respectively. The very

short relaxation times of the two flexibilized resins, resulting from their rather "loose", disarrayed structure, are reflected in the strain rate sensitivity exhibited by these two resins. It is reasonable to assume that the strains to failure for all the resins also shift with the increase in strain rate. Therefore, the relationship depicted by the plot in Figure 42 does not describe the actual failure strains existing during the test; however, the similarity between Figures 42 and 43 suggest that the relative magnitudes of the failure strains may remain the same under static and dynamic conditions.

VI-2. Unidirectional Composite Impact Resistance

When one impacts a unidirectional composite, the impact load is borne almost totally by the strip of fibers in contact with the impactor. Some of the load is transferred by the matrix to neighboring fibers, but because of the fact that the transverse moduli of unidirectional composites are so much less than the longitudinal moduli, most of the strain energy is absorbed by the fibers in direct contact with the impactor.

The measured data and the normalized data (normalized to 60 volume percent of fiber) from the impact tests are presented in Tables 15 to 18. Basically, the composites failed in two different ways. The first

failure mode was that of the cracking and punching out of a central strip of longitudinal fibers. This type of failure is shown in Figure 25(a). The second mode of failure was that of the propagation and opening up of a central crack in the composite and the subsequent wedging of the impactor through the crack. This type of failure is shown in Figure 25(b). No fiber breakage occurred except for compressive fiber shear on the impacted surface of the specimens in the latter mode of failure. For composites of approximately the same thickness, the composites with the stronger matrices sustained the punch out damage, and the weaker matrix composites sustained splitting damage. When the thicknesses of the latter composites were increased, punch out damage occurred during impact. It appears that the amount of composite deflection that occurs during the test, and the resin strength control the type of damage which is incurred. The splitting type of failure appears to occur with the thinner composites which sustain greater deflections during impact. This is probably due to significant membrane action within the specimen which produces in-plane stresses large enough to cause interfiber cracking to occur before flexural fiber fracture occurs.

When the load at failure values are normalized to 60 volume percent of fiber, they correlate very well

with thickness as shown in Figure 45. If one treats the central strip as a beam clamped at both ends, the deflection of the beam, e, can be computed as shown below:

$$e = \frac{Pl^3}{16\ Ebt^2} \tag{11}$$

E = Young's Modulus

P = load

l = span of the beam

b = width of the beam

t = thickness of the beam

Upon rearranging, the load exhibits the following relation with thickness

$$P = \frac{16\ eb\ Et^2}{l^3} \tag{12}$$

If one substitutes $E_mK_{vm} + E_fK_{vf}$ for E

where:

E_m = Young's modulus of the matrix

E_f = Young's modulus of the fiber

K_{vm} = Volume fraction of matrix

K_{vf} = Volume fraction of fiber

then, since $E_fK_{vf} >> E_mK_{vm}$, the load is a function of $K_{vf}t^2$. Actual loads at failure are plotted against K_{vf} x t^2 in Figure 46 There is considerable scatter but the trend suggests the relationship does hold, and that the load at failure is dependent on the fiber properties

and not on the matrix properties. When the width of the damaged area is included as b, there is no improvement in reducing the scatter.

Figures 45 and 46 also indicate that the type of failure that occurs has no apparent effect on the failure load. This suggests that the initiation of failure is the same for both types of damage-appearances. The punch out or splitting occurs as part of the failure propagation.

The energy of penetration, which is the difference between the total energy, Q_t, and the energy at maximum load, Q_m, is the energy required to break through the composite after failure initiates. The energy of penetration appears to correlate somewhat with the composite thickness (Figure 47). There are similar correlations of Q_m or Q_t with the laminate thickness.

The unidirectional composite test results indicate that the penetration test is one which is not sensitive to matrix properties. It is a fiber dominated test when the basis for impact resistance is chosen to be load to failure. The test itself can be classified as a dynamic flexural test, much like the Charpy or the Izod swinging pendulum tests. The unidirectional construction may not be desired when one wishes to simulate actual composite structural response to impact or to assess the impact resistance of composites. Since the unidirectional

impact test can be compared with a flexural test, when the span to thickness ratio becomes small enough (less than ≈15), significant shear stresses can be generated within the specimen to cause failure by either shear or a mixture of shear and compressive or tensile flexural failure. No specimens of thicknesses of sufficient magnitude to cause such failures were tested because of the large magnitude of the thickness which would be required to produce such failures.

VI-3. Crossplied Composite Impact Resistance

VI-3.1. Load at Initiation of Failure

Figure 48 presents load at initiation of damage, normalized to 60 volume percent fiber, as a function of crossplied composite thickness. Data for each of the four types of composites that were studied can be grouped separately and represented by four individual first order curves as shown in the figure. The curve fits appear to be good for the 930 and 840 matrix composites. The 956 matrix composites show data scatter at the high thickness end of the curve. The P-1700 specimens exhibit noticeable scatter at that part of the curve representing the thinnest composite data.

When the data are plotted on a log-log plot, the data also show a linear correlation. The slopes are close to 1.0 for the 930 and 840 matrix composites and

0.5 for the 956 matrix composites. The P-1700 matrix composite retains the slope of zero. From these results, one can assume that the two composites with the 930 and 840 matrices initiate failure by similar mechanisms. The failure mechanism for the P-1700 composite is of a different type. The 956 composite system possibly initiates failure by a combination of these two different mechanisms.

If the load at inception of failure were dependent on the plate flexure, the load would vary as the square of the thickness as shown in Equation 12. The initial failure mechanism, shear type compressive failure, occurs at the area of contact between the impactor and the compressive failure is due to a combination of stresses. The two primary stresses are the flexural compressive stresses on the surface fibers of the laminate and the bearing stresses caused by contact with the impactor. The bearing stresses are not a function of thickness, but determined by the load applied and the contact area. It therefore seems probable that the differences in the slopes of the load-thickness curves for the composites are due to the differences in the combination of stresses which caused failure to initiate. More of a proportion of flexural stresses are involved in causing the failure of the 930 composite than in the 956 or P-1700 composites.

From the impact test load-deflection curve, as shown in Figure 49, it appears that a different type of damage propagation is occurring during the impact failure of the P-1700 composites. Instead of the initial failure producing a decrease in linear slope in the load-deflection curve, the curve is not linear, but smoothly and continually decreases up to the point of maximum load.

If one examines Figures 50 to 52 which show cross sections of impacted composites, one may see there are differences in the types of failures. The 840 composite in Figure 50 has a fiber fracture failure from the surface to a point about one-third of the way through the composite and an interply delamination extending from this fracture toward the end of the composite laminate. No other delaminations are visible. The 956 composite cross section shown in Figure 51 exhibits a different type of localized damage. One can see fiber breakage at the impacted surface with interlaminar delaminations extending outward from the end of the crack through the fibers. Beneath this large delamination are a number of separate delaminations throughout the remaining section of the laminate. The 30-ply P-1700 matrix composite was tested by through penetration impact because an impact energy low enough to reach only to the point of maximum load would not be sufficient to produce damage in the

crosslinked epoxy matrix composites. It was desired to perform these tests at the same energy level for the four composites. However, by viewing Figure 52, which shows the damage area for a P-1700 matrix composite subjected to through penetration impact testing, one can see that there is only one main delamination and it appears to be located in the midplane between the two surfaces of the specimen (Figure 52(b)). If this is where the damage was initiated by interlaminar shear, the area of the specimen under the penetrator could be viewed on a two dimensional basis as two separate beams. The loss of the midplane shear stiffness would result in a loss in the load supporting capability of the damaged section to about one-half of that of the undamaged spec- imen. This is what one can see in Figure 48 when one compares the load of initiation of failure of the P-1700 matrix composites with that of the 930 matrix composites. This type of failure is discussed by Chamis [15].

The P-1700 composites have the lowest interlaminar shear strength of all the composites that were studied. As previously discussed, this low interlaminar shear strength is typical of linear resins which contain no functional groups that may react with the active sites on the fiber surfaces. This results in a very weak interfacial bond. This is worthy of note because possible correlations of composite properties, including

impact failure mechanisms and neat resin properties, can break down in the case of composites with low interfacial bonding, like the P-1700 matrix composites, because of the structure of the resin itself.

Figure 53 shows a linear correlation between load at initiation of damage and calculated composite shear strength for laminates of different thicknesses. Also plotted in the figure is the data point for the P-1700 composite. There is only one point plotted for the P-1700 laminate because the load stays constant with changes in thickness. It is interesting to note that the curves for the three thicknesses converge near this data point. It may be the result of the fact that, because of the combination of fiber selection and test equipment design, the load at initiation of damage ceases to be a function of shear strength, since the effective span-to-thickness ratio becomes too large for the generation of significant shear stresses during bending.

The results of this analysis indicate that localized damage at the area of contact of the impactor with the composite specimen may cause local shear induced compression failure. This failure in turn may initiate delamination, causing the change in the slope of the load-deflection curve. For the P-1700 composites, interlaminar shear failure at the composite midplane initiates damage.

VI-3.2. Analysis of Maximum Impact Load

Normalized maximum impact load is plotted as a function of specimen thickness in Figure 54. The maximum loads were all normalized to 60 volume percent fiber. Three points of interest are apparent from this figure. (a) The data for the three crosslinked epoxy resins are grouped closely together and can be reasonably represented by a single curve. (b) When the epoxy matric composites are represented by individual curves as in Figure 54, slopes of the linear curves gradually decrease with the 930 matrix composite data having the greatest slope and the 956 matrix composite data having the least slope. In contrast, the P-1700 matrix composite data is represented by a linear curve which has a significantly lower slope than the three crosslinked epoxies. (c) The four curves appear to converge at a thickness of about 0.60 inch (0.15 cm).

Since the relation between the load and the composite thickness is linear and not as shown in Equation 12, the mechanism is probably a result of the combined bearing stresses and flexural stresses. The results of other low velocity impact and static plate deflection testing [5,36] indicate this failure could be a flexural failure. Because of the apparent convergence of the four curves at a thickness of about 0.060 inch (0.15 cm), matrix effects on composite impact resistance

or response would not be observed when specimens with thicknesses below this value are tested. Also, laminate impact test geometric design must be given careful consideration, so that the impact conditions simulate those conditions of the structure under study, otherwise completely irrelevant results can be obtained.

VI-3.3. Extent of Internal Damage

Just as the specimen thickness affects the load at initiation of failure and the composite damage progression through the impacted specimen, it also has a significant effect on the internal damage sustained by the composite. Figure 39 shows ultrasonic through transmission C-scans of four thin impact specimens after being impacted and fully penetrated. It is apparent that the internal damage is small and also that there is not much difference in the sizes of damages areas. The area of internal damage appears to coincide with the observable external damage. In contrast, Figure 34 shows the damaged areas of four thick impacted specimens. The differences in areas are apparent. From these results, one can infer a direct relationship between thickness and extent of internal damage.

A correlation between composite internal damage area and composite shear modulus is evident from the data plotted in Figure 55. The shear modulus values are

calculated values using the constitutive equation previously presented in the discussion of the 10° off-axis test results. The thicknesses of these specimens range from 0.174 to 0.20 inch (0.44 to 0.51 cm). It is of interest to note that composite shear modulus has a pronounced effect on damage size when the modulus is below 600 ksi (4.14 GPa). However, when the modulus is above this value, no great advantage is realized by increasing the shear modulus for composites of this thickness. The impactor cross-sectional area is 0.196 in^2 (1.27 cm^2) and the damage area appears to approach this value asymptotically as the composite shear strength increases.

VI-3.4. Impact Energy Absorption

The impact energy data for the materials investigated in this study exhibit a significant amount of scatter which make a clear analytical evaluation difficult. The data are presented in Table 18. The energy values that are listed are:

(1) Energy at initiation of damage, Q_i

(2) Energy at maximum load, Q_m

(3) Total energy, Q_t

(4) Energy from damage, $Q_d = Q_m - Q_i$

(5) Energy of penetration, $Q_p = Q_t - Q_m$

The energy at initiation of damage is determined by the load at initiation of failure, P_i, and the deflection of the plate at the point of impact, e. For the crossplied graphite fiber reinforced composites, dP/de is very nearly linear. The load at failure, P_f, is controlled by the initial failure mechanism, and the maximum load possible for a composite is attained when failure initiates by flexural tensile failure of the fibers. For this type of failure, the energy at initiation of failure is also equal to the maximum energy at maximum load. The total energy absorbed is the total amount of energy that is needed to deflect and penetrate the sample enough so that the impactor load returns to zero. The energy of damage is a function of the size of the damaged area and the type of failure. The decrease in the effective section, resulting from the initial damage, causes a decrease in stiffness of the damaged area. The penetration energy is the energy required to break through or fracture all the fibers in the effective section of the specimen after the maximum load has been reached.

The energy at initiation of damage, normalized to 60 volume percent fiber, is plotted for each specimen as a function of thickness in Figure 56. Only the energy data for the crosslinked 930 matrix composite show a correlation with thickness. The data for the other three

types of composites are insensitive to the variation in thickness and are bound within a rather narrow energy range of about 3.0 to 8.0 ft-lb (4.1 to 10.9 J).

Normalized energies at maximum load (Q_m) are plotted in Figure 57 as a function of thickness for all the specimens that were tested. All the composites show trends of a correlation of energy at a maximum load with thickness. It appears that the four curves will converge at the origin.

When the normalized damage energies ($Q_m - Q_i$) are plotted as a function of thickness as in Figure 58, the P-1700, 840 and 956 matrix composites show a correlation between the two variables. The P-1700 matrix composite data is also correlatable when the actual energies of damage are plotted as a function of composite shear modulus as shown in Figure 59.

The total energies absorbed are listed in Table 18, but no attempt has been made to correlate these values with either thickness or fiber content. The values listed for the thickest specimens are not true total values since full penetration of the specimens did not occur for any of the crosslinked epoxy specimens. Full penetration did occur during testing of the thick P-1700 matrix specimens.

The analysis of the energies absorbed during impact indicate that the energies absorbed at maximum load are

dependent on the composite fiber content and the composite thickness. Also, it does confirm the observation, discussed previously, that the internal damage area increases with increasing composite thickness. This conclusion is based on the assumption that an increase in damage energy reflects an increase in damage area. When significant internal damage is caused by impact, it appears that the energy absorbed at the initiation of damage is almost constant for all the composites studied and the energy absorbed at maximum load is a strong function of the damage energy. The data from the 930 composite impact data shows that the thickness of the composite has a very strong influence on the energy absorbed by the material. At thicknesses below 0.1 inch (0.254 cm) the energy absorbed at maximum load is less than that of the other epoxy composites. When the thickness is increased to about 0.20 inch (0.508 cm) the energy absorbed is at least equal to that of the most energy absorbing composite material (956). This is significant because it demonstrates that impact energy absorption by plate deflection alone can be equivalent to that which occurs by the propagation of internal damage. This could possibly be due to the possibility that some membrane action developed during the impact of the 30-ply 930 composite.

Chamis has presented equations defining impact energy contributions by different failure mechanisms [15]. They are as follows:

$$\text{Flexural energy} = \frac{1 S_F^2}{18E} \tag{13}$$

$$\text{Interlaminar shear energy} = \frac{1}{15} \frac{S_F^2}{E} \left(\frac{t}{\ell}\right)^2 \left(\frac{E}{G}\right) \tag{14}$$

$$\text{Delamination energy} = \frac{N}{16} \left(\frac{t}{\ell}\right) \frac{E}{\tau} \frac{S_F^2}{E} \tag{15}$$

S_F = failure strength

N = number of delaminations

τ = interlaminar shear strength

ℓ = span of damaged area (measured from ultrasonic C scan)

t = thickness

These expressions are on a unit volume basis.

The damage energy from in-plane stress failure can be expressed as $\frac{S_F^2}{2E}$. This energy can become significantly greater than the flexural energy. It was estimated, using the formula presented by Sturm and Moore [37], that about 20 percent of the load sustained by the 30-ply 930 composite was borne by in-plane membrane stresses. Using the expressions presented above, the impact energy absorbed by membrane action was calculated to be about two and one-half times the energy absorbed by the flexural response of the composite.

This illustrates the importance of the development of in-plane stresses to improve the impact resistance of composites.

The dependance of shear energy and delamination energy on the composite thickness to span ratio is also illustrated in the expressions presented above. As the specimen thickness becomes thinner, while maintaining a constant span, it can be seen that these two shear property related energies can become insignificant, and that the energy absorbed by the impacted laminate becomes dependent on the composite tensile properties. These properties are dominated by the fiber properties.

VI-3.5. Analysis of Plate Deflections

The major portion of the analysis of composite impact resistance from the test results of this study has as its basis the data generated by the microprocessing unit of the drop-weight impact tester. Actually, two test variables are measured. These variables are the load and the impactor velocity at the initiation of impact. The time after initiation of impact was also measured. The energy values and the deflection values are calculated from the equations given in Appendix E.

Static plate deflection tests were conducted to assess the reliability of the data generated by the impact test equipment, and to measure the plate strains

as a function of plate deflections. It was considered advisable to experimentally measure the strain resulting from the plate deflections because there is no convenient analytical relationship in the literature for predicting backside strains for orthotropic laminated plates.

Static plate deflection tests were run using both neat resin and crossplied composite specimens. Strain gages were bonded to the backside (opposite the impacted side) of the specimens to measure the surface strains opposite the point of loading. The specimens were clamped to the impact tester anvil and the anvil was placed on a compression load cell in an Instron Tensile Test Machine. The load was measured with the load cell. A dial gage was used to read the crosshead position. The indenter used was a 0.5 inch (1.27 cm) diameter steel ball. The specimens were loaded, the crosshead position was recorded, and then the specimen was unloaded. When the load read zero, the crosshead position was again recorded. The difference between the crosshead position before loading and after loading was taken to be the distance of indentation of the penetrator into the specimen.

Figure 60 shows the data for the 840 resin along with the impact test data and values calculated using the equation of Sturm and Moore [37]. The calculated

values and the static test data, corrected for penetration by the penetrator, show very good agreement. The impact test data lie above the calculated curve showing the strain rate effect on the dynamic test results. In contrast, Figure 61 presents calculated data and impact test data for the 930 epoxy resin. No indication of strain rate affects are evident in this figure. Dynamic mechanical analysis tests showed no appreciable strain rate sensitivity of this resin at low strain rates. The other two resins reacted similarly. The 956 epoxy resin shows greater strain rate influence in its dynamic response, and the linear P-1700 resin shows minimal strain rate effects, but does show indications of indentation and plastic deformation at the higher loads.

Figure 62 shows dynamic and static load-deflection data for the Celion 6000/840 crossplied composite. There is very good agreement between the static deflection values and the impact induced deflection values. The impact data curve is not corrected for penetrator indentation.

These data do indicate that the data generated from the impact tests are reliable data and also that load-deflection response of graphite fiber reinforced composites due to low velocity impact can be simulated by

static tests. The latter conclusions have also been observed by Bostaph and Elber [36].

The correlation between backside strain and impact specimen deflection is shown graphically in Figure 63 for both a 0.109 inch (0.28 cm) thick Celion 6000/840 composite and a 0.130 inch (0.33 cm) 840 epoxy resin plate. None of the data are corrected for impactor penetration. Each data point is the average of two readings. The resin plate shows greater strain than the composite plate for the same deflection. This can be due, in part, to the differences in thickness of the two specimens, but is most likely due to the large differences in magnitude of the Young's moduli of the two specimens. Figure 64 is a plot of load for the Celion 6000/840 composite as a function of backside strain (determined statically). This composite failed at a load of about 650 lb (2891 N) which corresponds to a backside strain of about 1.47 percent.

Specimens measuring 0.5 inch (1.3 cm) by 6 inch (15.2 cm) were cut from portions of the impacted thick crossplied specimens which ultrasonic transmission C-scans showed were undamaged and tested in three point flexure. The tests were conducted to measure the fiber strain at failure for each of the types of composites. The span was 4 inch (10.2 cm) giving a span to depth ratio of about 20 to 1. The test data are presented in

Table 25. All of the specimens failed by compressive failure. The calculated compressive failure strains are much less than the fiber ultimate strain and they range from about one-half to two-thirds of the fiber ultimate strain. These strains are also less than the failure strain of the 840 composite as measured by the static deflection tests. This may be due to the fact that the ends of the beams were not clamped. The greatest interlaminar shear stress calculated was that for the P-1700 composite and its value is 2400 psi (16.5 N/m^2). This value is about one-half the shear strength measured by the 10° off-axis test.

The failure stresses for the 930 composites and the Celion P-1700 composites are considerably higher than those measured by compression tests and presented in Table 26. The values for the other two composites are close to those values measured by the compression tests, but much lower than the values for the 930 and P-1700 composites.

Davis [38] has shown that the compressive shear failure, in which fracture across the fibers occurs, is dependent on the composite shear modulus. The initial waviness of the fibers in the composite allows microbuckling of the fibers to occur under compressive loads. This then creates a shear strain on the composite. He has also shown experimentally that the composite shear

modulus changes with compressive loading. The composite shear modulus then is the modulus at that point of strain on the shear stress-strain curve resulting from the combination of the compression stress with the shear stress. For those composites with extremely nonlinear shear stress-strain curves (such as the 840 and 956 composites), the failure point can be reached very quickly when the composite is subjected to an increasing compression load. The failure stresses are then considerably lower than those calculated from the appropriate constitutive equation using the initial composite shear modulus.

The static clamped plate deflection tests do simulate the low velocity impact response of graphite fiber reinforced composites. Composite impact damage threshold strains cannot be simulated by the three point bend test, nor can all composite compressive flexural failure stresses be determined by standard composite compression tests. From the results of this study it appears that flexural failure of composites with the stronger, high modulus matrices may not be simulated by compression tests, but flexural failure of the composites with the more flexible, loosely crosslinked and long chain polymer matrices can be simulated by this type of testing.

The instrumented drop weight impact test appears to produce reliable deflection and energy data. The deflections of composites can be simulated with static tests, but composite damage thresholds cannot be simulated by simple mechanical tests.

CHAPTER VII

ANALYSIS OF FRACTURE TOUGHNESS DATA

VII-1. Neat Resin Fracture Toughness

The fracture touchness data for the four neat resins were reproducible for each of the resins. There is no correlation between resin fracture toughness and resin impact resistance. When impact resistance is considered as a basis, the resins are ranked as follows:

P-1700 > 956 > 840 > 930.

When K_{IC} is used as the criterion, the ranking is:

P-1700 > 956 > 930 > 840.

The ranking, based on G_{IC} values, is as follows:

956 > P-1700 > 840 > 930.

The large G_{IC} value for the 956 resin could be a result of a significant amount of plastic deformation at the crack tip during the testing. There was some nonlinearity in the load-deflection curve for this resin at high loads. When one compares fracture toughness test data with impact test data, one must consider that the comparison is between a dynamic test and a pseudo static test. The flexibilized resins, which are very strain-rate sensitive, exhibit different mechanical

properties under each of these two testing conditions and therefore it would be expected that differences in rankings could result when comparing the data from these two tests.

Analysis of the neat resin fracture toughness data also indicate that there is no correlation between resin fracture toughness and composite impact resistance.

VII-2. Composite Fracture Toughness

The results of this study show no direct relationship between composite double cantilever beam fracture toughness and composite impact resistance. One would expect a strong relationship between the interlaminar fracture toughness and extent of damage. The 930 composite exhibits the lowest fracture toughness of the four composite materials, but it also sustains the least amount of internal damage. Under the conditions of the drop weight impact test, it appears that the mechanism for propagation of impact damage is not Mode I fracture.

It is of interest to note some observations that were made during the double cantilever beam fracture toughness testing. In analyzing these tests, one assumes that all the strain energy is utilized in creating two new surfaces which results from the separation of the two halves of the beam. The P-1700, 840 and 956 composite specimens did sustain permanent deformation

during the tests. The two separating beams of some specimens were permanently separated as much as 0.75 inches (1.92 cm) at the aluminum loading blocks after the specimens were removed from the tensile tester at the conclusion of the testing. It was evident that some of the strain energy was dissipated as energy of deformation and not as new surface energy. This was reflected in the calculated K_{IC} values which first increased as the crack propagated through the specimen, and then decreased as the crack continued growing. The results of this study indicate that the double cantilever beam fracture toughness list is not suitable for the composites with flexibilized resins. Apparently, the short relaxation times of the two flexibilized resins and the extended amount of time necessary to conduct the tests allowed a considerable amount of relaxation to occur in the composite matrices.

CHAPTER VIII

SUMMARY OF THE STUDY

VIII-1. Summary of Composite Impact Response

During the initial period of low velocity impact (up to the point where the slope first changes, point A, on the load deflection curve), the response of the laminate is a function of the thickness and the fiber volume fraction of the composite. No significant effects from differences in matrices are apparent. The composite stiffness, which is fiber controlled, controls the reaction of the laminate.

Prior to the attainment of the maximum load point (point B) on the load-deflection curve, the P-1700, 840, and 956 composites experienced localized damage and the areas of damage appeared to increase with increasing laminate thickness. The area of damage caused a change in the load-deflection relationship for each of the composite materials and the change was different for each of the composites that were studied. Because of the damage, which was either delamination, initiated by compressive flexural failure, or interlaminar shear failure, the stiffness of the damaged area became less than that of the undamaged portion of the plate and the subsequent

absorbtion of energy was localized in the damaged portion of the plate. With the initiation of damage, a new set of effective plate dimensions were created. There were the effective section (thickness) of the damaged area and also the effective span which extended to the boundary of the damaged area. These parameters then controlled the slope of the load-deflection curve to the point of maximum load.

The initiation of failure of the 840 and 956 cross-plied composites was found to be due to compressive failure on the impacted surface. The failure appeared to be shear failures across the fibers. Davis [38] has shown that this type of failure is dependent on the composite shear modulus and that the composite shear modulus changes as the compressive loading changes. In effect, it moves up the shear stress-strain curve. For those composites with nonlinear stress-strain curves, like the 840 and 956 composites, the failure stresses can be considerably lower than those predicted by a laminate theory which does not take this fact into account. The P-1700 composite exhibits a more linear shear stress-strain curve. Because of this and its low interlaminar shear strength, interlaminar shear failure occurs before compressive failure does. The initial failure for all the composites can therefore be related to the composite

shear properties and to the matrix moduli and strengths through the appropriate constitutive relationships.

It was found that the energy absorbed at maximum load increased with increasing thickness for all the composites that were studied. The composites with the linear polysulfone matrix absorbed the least amount of energy up to the point of maximum load. This is the result of the fact that almost all the energy absorbed up to this point was flexural energy. The effect of shear energy release on the total energy absorbed at maximum load for these composites was not realized because the shear failure occurred at the point of maximum load. The flexibilized matrix composites absorbed most of damage energy over the range of thicknesses studied. The increase in damage energy with increasing thickness infers that the damage area increases with increasing thickness also. This was confirmed by C-scan evaluation of the impacted composites. The most significant result from the energy absorption data is that the thicker 930 composites, with the relatively strong crosslinked matrix, actually absorbed at least as much energy at maximum load as the composites with the flexibilized matrices even though the flexibilized composites sustained extensive internal damage. This energy absorption by the 930 composite occurred with only a

relatively small amount of internal damage being generated. The 930 composites also sustained the greatest loads at failure in comparison with the other three types of composites. This superiority in impact resistance is apparently due to the development of some membrane action in the composite prior to failure. These results indicate that a high strength matrix, which forces the composite impact failure into fiber controlled mechanisms, can produce tougher composites. It also appears that toughness can be increased by the utilization of membrane action within the composite structure during the impact event.

The unidirectional composite impact tests do not appear to provide information which is applicable or useful in evaluating the effects of the matrices on composite impact properties. This appears to be a result of the highly anisotropic nature of the composite which does not allow the impact load to be distributed over the full area of the laminate. Interfiber cracking occurred in a direction parallel to the fiber direction. This isolated the fiber directly in contact with the impactor and forced them to support the full force of the impact load. The reaction of unidirectional composites to impact is highly dependent on the laminate stiffness in both the transverse direction and the fiber

axial direction. The laminate stiffness is a function of both the laminate thickness and the tensile moduli.

From the results of this study it appears that there is no relationship between crossplied composite low velocity impact response and either resin or composite Mode I fracture toughness.

VIII-2. Polymer Structure

During this study it was found that the composite impact response could be related to the matrix structure through the properties of the matrices. Basically, the matrices differed in backbone or chain structure, crosslinking density, and hardener structure. The data from the resin properties measurements do agree with structural properties relationships that have been presented in the literature.

Increasing the strain to yield or strain to fracture by decreasing the crosslink density or by adding flexibilizers, while it did increase the neat resin toughness, did not increase the graphite fiber reinforced composite toughness. The addition of flexibilizers decreases the polymer strength and modulus sufficiently to allow resin controlled failure to occur at low loading values. The linear polymer (P-1700), which contains no crosslinking,

does not effectively bond with the fiber surfaces possibly because of the lack of active pendant groups which could react with the fiber active sites.

The crosslinked polysulfone resin possesses strength properties almost as great in magnitude as the crosslinked 930 epoxy. The polysulfone does have a modulus of about one-half of the modulus of the crosslinked epoxy and a greater strain to yield. It appears that the high strength of both of the polymers can be attributed to the backbone structures which are highly aromatic. The differences in moduli can probably be attributed to the differences in crosslinking which also would affect the strains to yield and failure.

The results of this study indicate that the most probable way of successfully producing a tougher polymer which will impart toughness (minimal internal damage) to a graphite fiber reinforced composite would be to put the flexibility into the backbone chain and into the crosslinking molecules. The objective is one of increasing the matrix strain to yield or fracture value without decreasing the strength or modulus. This means that both the strain to yield or fracture and the tensile strength must be increased. This precludes the utilization of reductions in crosslinking density or flexibilizers as a means for toughening resins, since these

methods would most likely reduce the resin modulus and strength.

In order to prevent the type of internal damage observed in this study, it is not necessary to produce a composite with a shear modulus greater than 600 ksi (5.1 GPa). This modulus can be produced for a composite containing 60 volume percent of fiber by using a matrix with a shear modulus by about 200 ksi (1.4 GPa) or a tensile modulus of about 545 ksi (3.75 GPa). For those composites with shear moduli greater than 600 ksi (4.1 GPa), the initial failure should be a flexural tensile failure if the shear stress-strain curve is not excessively nonlinear. The failure loads should then depend on the tensile properties of the fiber and tenfold increase in the tensile strength of the 930 resin would only result in a 14 percent increase in the unidirectional flexural strength of a composite with a 930 matrix.

The fiber-matrix interfacial bonding efficiency has been shown to be of great importance in the reaction of crossplied composite plates to impact. When the interfacial bonding is very low as in the case with the P-1700 laminates, from the results of the 10° off-axis test, it appears that the initial shear modulus is not decreased but the shear strength is decreased significantly. The

bonding effectiveness must be taken into account in calculating composite properties from constitutive equations.

If one were to change the specification or definition of composite toughness to be the ability of a composite to absorb a significant amount of energy before total penetration, the promotion of high energy absorbing failure mechanism would be in order. These types of structures are called containment structures and are used as a means of preventing loose debris from being ejected into areas where it could result in a safety hazard or cause intolerable harm. Since the load at initiation of damage does not necessarily have to be an ultimate, it is possible to choose a matrix structure which would allow extensive delamination or interlaminar shear failure to occur.

The instrumented drop-weight impact tester has been shown to be a useful, accurate, and reliable research tool in assessing composite low velocity impact resistance.

CHAPTER IX

CONCLUSIONS

From the results of this study, the following conclusions can be made in relation to the response of graphite fiber reinforced composites to low velocity impact:

1. Composite failure initiates by compressive failure in the vicinity of the impact site on the impacted surface except when the matrix-fiber surface bond is of insufficient magnitude to prevent interlaminar shear to occur.

2. The load at initiation is a function of laminate thickness. The order of the relationship between the load and thickness appears to be dependent on the properties of the matrix.

3. The maximum load and the energy absorbed at maximum load are linearly dependent on the thickness of the impacted laminate.

4. The area of internal damage increases with increasing thickness.

5. Under the conditions of the impact tests used in this study, when the thickness of the laminate is below 0.06 to 0.07 inches (0.15 to 0.18 cm) all graphite fiber

reinforced laminates respond identically to low velocity impact in respect to loading capabilities and amount of internal damage.

6. The impact testing of unidirectional composites does not provide information which is applicable in evaluating the effects of matrices on composite impact properties.

7. No relationship was found between composite low velocity impact response and either resin or composite Mode I fracture toughness.

Conclusions regarding the effect of polymer matrix properties on the low velocity impact resistance of graphite fiber reinforced composites which were gained from this study are as follows:

1. When the drop-weight impact test is used to evaluate material impact resistance, resin impact resistance, based on load to failure appears to be a function of the resin strain to failure. When energy absorbed at failure is used as a criterion for impact resistance, polymer ranking appears to be dependent on the amount of membrane action sustained by the polymer prior to failure.

2. The results of drop-weight impact testing show no relationship between polymer toughness and the toughness of a composite having the identical polymer as a matrix. This is probably due to the limited amount of

membrane action which occurs during the impacting of the inherently stiff graphite fiber reinforced laminates.

3. Polymer matrix shear modulus has a significant effect on the amount of internal damage incurred by impacted laminates when the laminate thickness is greater than 0.07 inch (0.18 cm) and the matrix shear modulus is less than 200 ksi (1.4 GPa).

4. In order to increase the impact resistance of a graphite fiber reinforced composite, both the matrix modulus and the matrix tensile strength must be increased. The matrix strain at yield naturally increases also.

5. The use of flexibilizers to produce a more ductile polymer does not necessarily increase the impact resistance of a graphite fiber reinforced composite having the flexibilized polymer as a matrix. Flexibilizers normally lower the T_G, modulus and tensile strength of a polymer.

6. Linear polymers do not usually impart their toughness to graphite fiber reinforced composites in which they are used as matrices. The reason for this is probably because of the absence of active pendant groups on the linear chain which are necessary to react with reactive sites on the graphite fiber surfaces to produce strong interfacial bonding.

7. From the results of this study one can conclude that the toughening of a polymer matrix may best be realized by increasing the toughness of the polymer backbone.

REFERENCES

1. Serafini, T. T., "PMR Polyimide Composites for Aerospace Applications," NASA TM-83047, November (1982).

2. Bowles, K. J., "Impact Behavior of Filament Wound Graphite/Epoxy Fan Blades," NASA TM-78845, May (1978).

3. Graff, J., Stoltze, L., and Yarholak, E. M., "Impact Resistance of Spar Shell Composite Fan Blades," NASA CR-134521 (1973).

4. "Impact Resistance of Composite Fan Blades," NASA CR-134707, December (1974).

5. Ramkumar, R. L., "Composite Impact Damage Susceptibility," NADC-79068-60, pg. 2, January (1981).

6. Chamis, C. C., Hanson, M. P., Serafini, T. T., "Impact Resistance of Unidirectional Fiber Composites," Composite Materials Testing and Design, ASTMSTP-497, pp. 324-349, (1972).

7. Miller, A. G., Hertzberg, P. E. Rantala, V. W., "Toughness Testing of Composite Materials," 12th National SAMPE Technical Conference, pp. 279-291 (1980).

8. Winsa, E. A., Petrasek, D. W., "Pendulum Impact Resistance of Tungsten Fiber/Metal Matrix Composites," Composite Materials: Testing and Design, ASTM STP-497, pp. 350-362 (1972).

9. Novak, R. C., DeCrescente, M. A., "Impact Behavior of Unidirectional Resin Matrix Composites Tested in the Fiber Direction," Composite Materials: Testing and Design, ASTM STP-497, pp. 311-323, (1972).

10. Mallick, P. K., Broutman, L. J., "Impact Properties of Laminated Angle Ply Composites," S.P.I., Anniversary Technical Conference, Section 9-C, pp. 1-8, (1975).

11. Sykes, G. F., Stoakley, D. M., "Impact Penetration of Graphite/Epoxy Laminates," 12th National SAMPE Technical Conference, pp. 482-493, (1980).

12. Cristescu, N., Maluern, L. E., and Sierakowski, R. L., "Failure Mechanisms in Composite Plates Impacted by Blunt-Ended Penetrators," Foreign Object Impact Damage to Composites, ASTM STP-568, pp. 159-172, (1975).

13. Whitney, J. M., "Free Edge Effects in the Characterization of Composite Materials," Analysis of the Test Methods for High Modulus Fibers and Composites, ASTM STP-521, pp. 167-180, (1973).

14. Greszczuk, L. B., "Response of Isotropic and Composite Materials to Particle Impact," Foreign Object Damage to Composites, ASTM STP-568, pp. 183-211, (1975).

15. Chamis, C. C., and Sinclair, J. H., "Impact Resistance of Fiber Composites: Energy Absorbing Mechanisms and Environmental Effects," NASA TM-83594, May (1984).

16. Lee, H., and Neville, K., Handbook of Epoxy Resins, 2nd ed., McGraw-Hill Book Co., New York (1967).

17. Bucknall, C. B., Page, C. J., and Young, V. O., "Quantitative Studies of Toughening Mechanisms in ABS and ASA Polymers," Toughness and Brittleness of Plastics, American Chemical Society, Washington, D.C., p. 179, (1976).

18. Zang, B. Z., Uhlmann, D. R., and Vander Sande, J. B., "The Rubber Particle Size Dependence of Crazing in Polypropylene," Society of Plastics Engineers, 42nd Technical Conference Proceedings, pp. 523-525, (1984).

19. Yoon, S. K., "Carbon Reinforced Composites: Effects of Fiber Surface on Polymer Properties," Polymer Engineering and Science, vol. 22, no. 13, pp. 805-806, (1982).

20. Fitzer, E., Weiss, R., "Surface Treatment of Carbon Fibers," Processing and Uses of Carbon Fibre Reinforced Plastics. VDSl-Verlag GmbH, pp. 45-64, (1981).

21. Chamis, C. C., and Sinclair, J. H., "10° Off-Axis Tensile Test for Intralaminar Shear Characterization of Fiber Composites," NASA TND-8215, April (1976).

22. Legg, M. J., "Effect of Resin Flexibility on the Properties of Glass Filament Wound Pipes," Ph.D. Thesis, University of Liverpool, pp. 81-82, March (1980).

23. Jones, R. J., Vaughan, R. W., and Burns, E. A., "Thermally Stable Laminating Resins," NASA CR-72984, pp. 179-180 (1972).

24. Lange's Handbook of Chemistry, edited by Dean, J. A., Eleventh Edition, McGraw-Hill Book Co. (1973).

25. Chamis, C. C., "Simplified Composite Micromechanics Equations for Hygral, Thermal and Mechanical Properties" SAMPE Quarterly, vol. 15, no. 3, pp. 14-23, April (1984).

26. Smith, R. E., "Ultrasonic Constants of Carbon Fibers and Their Composites," Journal of Applied Physics, vol. 41, no. 6, pp. 2555-2560, June (1972).

27. Chamis, C. C., "Simplified Composite Micromechanics Equations for Strength, Fracture Toughness, and Environmental Effects". NASA TM-83320, January (1984).

28. Design Engineering Data-Udel Polysulfone, Union Carbide Corp., Section 2, page 1, (1979).

29. Advanced Composite Materials - hyE, Fiberite Corp., Sheet E-1.

30. Nielson, L. E., Mechanical Properties of Polymers and Composites, vol. 1, Marcel Dekker, Inc., New York, (1974).

31. Misra, S. C., Manson, J. A., and Sperling, L. H., "Effects of Cross-Link Density Distribution on the Engineering Behavior of Epoxies," Epoxy Resin Chemistry, ACS Symposium 114, pp. 137-156, 1979.

32. Saxena, A., Hudak, S. J., "Review and Extension of Compliance Information for Common Crack Growth Specimens," International Journal of Fracture, vol. 14, pp. 453-468, (1978).

33. Wang, A. S. D., Pipes, R. B., and Anmadi, A., "Thermoelastic Expansion of Graphite-Epoxy Unidirectional and Angle-Ply Composites," Composite Reliability, ASTM STP-580, pp. 574-585, (1975).

34. Daniel, I. M., Liber, T., and Chamis, C. C., "Measurement of Residual Strains in Boron-Epoxy and Glass-Epoxy Laminates," Composite Reliability, ASTM STP-580, pp. 340-351, (1975).

35. Pagano, N. J., Hahn, H. T., "Evaluation of Composites Curing Stresses," Composites Materials: Testing and Design (Fourth Conference), ASTM STP 617, pp. 317-329, (1977).

36. Bostaph, G. M., and Elber, W., "Static Indentation Tests on Composite Plates for Impact Susceptibility Evaluation," Proceedings of the Army Symposium on Solid Mechanics Problems 1982 - Critical Mechanics Problems in Systems Design, AMMRC MS 82-4, pp. 288-317, (1982).

37. Sturm, R. G., and Moore, R. L., "The Behavior of Rectangular Plates Under Concentrated Loads," Journal of Applied Mechanics, Vol. 4, No. 2, (1937).

38. Davis, J. G., Jr., "Compressive Strength of Fiber Reinforced Composite Materials," Composite Reliability, ASTM STP 580, pp. 364-377, (1975).

39. Sattar, S. A., and Kellogg, D. H., "The Effect of Geometry on the Mode of Failure of Composites in the Short-Beam Shear Test," Composite Materials: Testing and Design, ASTM STP 460, pp. 62-71, (1969).

40. Han, K. S., and Koutsky, J., "The Interlaminar Fracture Energy of Glass Fiber Reinforced Polyester Composites," Journal of Composite Materials, Vol. 15, pp. 371-388, (1981).

41. Devitt, D. F., Schapery, R. A., and Bradley, W. L., "A Method for Determining Mode I Delamination Fracture Toughness of Elastic and Viscoelastic Composite Materials," Journal of Composite Materials.

42. Hulsey, R. C., "Delamination Fracture Toughness of a Unidirectional Graphite/Epoxy Composites," M.S. Thesis, Texas A M University, December (1980).

43. Kreiger, R. B., "The Relationship Between Graphite Composite Toughness and Matrix Shear Stress-Strain," SAMPE, 29th National Symposium, pp. 1570-1584, April (1984).

44. Mallick, P. K., and Broutman, L. J., "The Influence of the Interface on the Fracture Toughness of Low Aspect Ratio Fiber Composite," SPI 29th Annual Technical Conference, Section 13-B, (1974).

45. Yeung, P., and Broutman, L. J., "The Effect of Glass-Resin Interface Strength on the Impact Strength of Fiber Reinforced Plastics," Polymer Engineering and Science, Vol. 18, p. 62 (1978).

46. Berry, J. P., "Determination of Fracture Surface Energies by the Cleavage Technique," Journal of Applied Physics, Vol. 34, p. 62 (1963).

47. Whitney, J. M., Browning, C. E., and Hoogsteden, W., "A Double Cantilever Beam Test for Characterizing Mode I Delamination of Composite Materials," Journal of Reinforced Plastics and Composites, Vol. 1, pp. 297-313, (1982).

48. Pipes, R. B., Kaminski, B. E., and Pagano, N. J., "Influence of the Free Edge Upon the Strength of Angle Ply Laminates," Analysis of the Test Methods for High Modulus Fibers and Composites, ASTM STP-521, pp. 218-229, (1973).

49. Adams, D. F., "Impact Response of Polymer Matrix Composite Materials," Composite Materials: Testing and Design (Fourth Conference), ASTM STP-617, pp. 409-426, (1977).

APPENDIX A

THE 10° OFF-AXIS TENSILE TEST

The 10° off-axis tensile test was developed to measure unidirectional fiber reinforced composite shear properties. The three point, short-beam-shear test has been the most commonly used test for measuring composite interlaminar shear strength. While this test is very suitable for composite quality control, it does not produce fundamental information on deformation or fracture mechanics, nor does it give design data. The reasons for this are:

1. Nonuniform shear stresses are produced through the specimens thickness during testing [38].

2. The test produces only shear stress at fracture and not shear-strain information from which shear-modulus can be computed.

The thin wall tube torsion test, while useful in generating basic information, is very expensive and time consuming both in test piece fabrication and test conduct and thus has been used very little as a standard test. The 10° off-axis test bridges the gap between these two other tests since it does produce shear stress-strain

data and it is relatively simple to fabricate test specimens.

A schematic of a 10° off-axis tensile specimen is shown in Figure 3. The unidirectional fibers are oriented 10° off the specimen axis along which the test load is applied. The test piece dimensions are selected to insure an adequate gage length for the failure to occur within the gage length. Strains are measured with two 60° strain gage rosettes bonded on opposite sides of the specimen.

The stresses in a ply with angles oriented at an angle of 10° from the load direction as a function of the applied stress, σ_{xx} are given by the following equations:

$$\sigma_{11} = \sigma_{xx} \cos^2 10° \tag{14}$$

$$\sigma_{22} = \sigma_{xx} \sin^2 10° \tag{15}$$

$$\sigma_{12} = \sigma_{xx} \sin^2 20 \tag{16}$$

σ_{11} = the stress along the axis of the fibers

σ_{22} = the transverse stress perpendicular to the axis of the fibers

σ_{12} = the intralaminar shear stress

When the trigonometric values are substituted into the above equations, they become

$$\sigma_{11} = 0.970\ \sigma_{xx} \tag{17}$$

$$\sigma_{22} = 0.030\ \sigma_{xx} \tag{18}$$

$$\sigma_{12} = 0.171\ \sigma_{xx} \tag{19}$$

One can see that the transverse tensile stress, σ_{22}, is very small -- about one-sixth the value of the intralaminar shear stress.

Since there is a combined-stress interaction involved, by examining a combined-stress-failure relationship, one can determine which stress initiates fracture. Using the combined-stress failure criterion derived from a modified distortion energy principle [21]:

$$\sigma = 1 - \left(\frac{\sigma_{11}}{\sigma_{11F}}\right)^2 + \left(\frac{\sigma_{22}}{\sigma_{22F}}\right)^2 - K_{12}\left(\frac{\sigma_{11}\sigma_{22}}{\sigma_{11F}\sigma_{22F}}\right) + \left(\frac{12}{\sigma_{12F}}\right)^2 \leq 0 \tag{20}$$

where σ_{11F}, σ_{22F}, and σ_{12F} are the fracture strength in the 11, 22, and 12 directions respectively, that the intralaminar shear stress initiates fracture of the 10° off-axis tensile specimen. K_{12} is a coupling coefficient which depends on the elastic constants of the composite material [21].

APPENDIX B

DYNAMIC MECHANICAL PROPERTIES MEASUREMENTS

The dynamic mechanical analyzer utilizes the measurement of torque in forced torsion of the flat specimen to calculate the stored shear modulus (G'), the loss shear modulus (G"), and the tangent delta (tan Δ). The complex modulus (G*) is related to the stored modulus and the loss modulus by the following relations:

$$(G^*)^2 = (G')^2 + (G'')^2 \qquad (21)$$

$$\tan \Delta = \frac{G''}{G'} \qquad (22)$$

The term, tan Δ, denotes the tangent of the angle that the shear strain lags the applied stress and represents the damping of the material. The stored modulus is representative of the energy stored during the torquing of the specimen. The loss modulus is representative of the energy lost as heat from the movement of the polymer chains relative to one another during the torquing of the specimen.

For the testing equipment used in this study, the relations between the two moduli and the variables of the test are:

G' = K [real M/θ]

G" = K [imaginary M/θ]

where

$$K = \frac{980.7\ L}{(t/10)^3\ W[1/3-0.21\ T/W]} \qquad (23)$$

L = length

t = thickness

W = width

M = torque of transducer

The maximum strain (ϵ) imposed on the sample is defined as:

$\epsilon = \theta t/L$

θ = angle of strain

Tests were run varying frequency at constant temperature and varying temperature at a constant frequency. Temperature scans were run at three different maximum strain values. These were 0.1, 0.5, and 0.1 percent strain. The temperature was controlled by heated nitrogen gas supplied from a liquid nitrogen Dewar.

APPENDIX C

THERMAL ANALYSIS

The principle of operation of the thermal analyzer is the measurement of the expansion of a material as a function of temperature. A flat ended quartz probe is positioned to sit on one surface of the sample being studied. Both the sample and the quartz probe are situated within a flat bottomed quartz tube. As the specimen changes dimension, the probe is displaced either upward or downward along its axis (Figure 65). The specimen, probe and quartz tube are surrounded by a furnace which is a cylindrical heater containing a control thermocouple. The furnace is driven by a temperature programmer-controller. A thermocouple is positioned to touch the sample and provides an output proportional to the sample temperature The quartz probe is connected at its upper end to a LVDT which provides a dc output proportional to the linear displacement core. Both the specimen thermocouple output and the LVDT output are applied directly to an x-y-y' recorder, thus providing a displacement-temperature trace of the data.

The instrument is calibrated in two steps. First the apparatus is run without a sample to determine the

inherent expansion differences between the quartz probe and the quartz tube over the temperature range of interest. Then a calibrated aluminum test piece is positioned within the tube and a displacement-temperature trace is recorded. Using the known thermal expansion coefficient for the aluminum block, the LVDT output is converted to linear displacement data.

All samples measured about 0.25 inch (0.635 cm) by 0.25 inch (0.635 cm) by 0.10 to 0.13 inch (0.254 to 0.330 cm) in thickness. Composite samples were measured across the thickness and across the width and along the length of the sample. Both unidirectional composites and 0°/90° composites were studied.

The heating rate was 9° F (5° C) per minute and the temperature range was limited to the difference between room temperature and the temperature at which the particular resin or composite was cured or molded.

APPENDIX D

COMPOSITE INTERLAMINAR FRACTURE TOUGHNESS TESTS

The double cantilever beam Mode I interlaminar fracture toughness test is currently being used by a large number of investigators to study Mode I fracture of fiber reinforced composites [40 to 44]. The advantages of the DCB specimen are:

1. It offers a direct approach to determining Mode I interlaminar fracture toughness.
2. It produces stable crack growth during the test.
3. A large amount of data can be measured from one test.
4. It does not require special equipment or instrumentation.

With the high level of interest for this test, there is also a significant amount of activity being directed toward evaluating the effect of variables and analysis procedures on the results of this test method. A modified DCB specimen, called the width tapered double cantilever beam (WTCB) specimen was found to give results sensitive to the taper ratio and the beam thickness [40]. This is attributed to viscoelastic-plastic behavior in the specimens. As the beams become wider or thicker,

the percent of viscoelastic-plastic energy absorbed becomes smaller and the GIC value approaches a constant value.

Viscoelastic behavior in the DCB specimen has been studied also [41]. It was concluded that the test was applicable to composite materials which exhibit a linear tensile stress-strain relationship parallel to the fiber direction and viscoelastic effects are limited to a small area around the crack tip. High modulus filament composites generally meet these requirements and the composites evaluated in this study meet these requirements under both tensile and bending modes of testing.

An error analysis of the double cantilever beam fracture toughness test indicates that the critical measurement is the load measurement [42].

The specimens were cut from 22 ply unidirectional panels. A 0.003 inch (0.008 cm) thick by 1.75 inch (4.45 cm) long piece of Teflon film was placed between the eleventh and twelfth plies. The film provided a starter crack extending 1.25 inch (3.18 cm) from the point of loading into the specimen. The plates from which the specimens were cut were cured or molded as previously described.

The aluminum loading blocks were bonded to the test specimen ends with an epoxy adhesive after the bonding surfaces were grit blasted with alumina powder. The

edges of the specimens were sprayed with white enamel. After the enamel had dried, the sides were indexed with markings every 0.025 inch (0.635 cm). The white paint and the indexing aided in the following the progress of the crack front as it proceeded through the specimen.

The load was traced as a function of time on an x-y recorder. Crack lengths were notated on the traces at the time of measurement on the load-displacement traces. The crack opening displacement was calculated from the crosshead speed and the chart speed. The accuracy of this method was checked by measuring the bending modulus of two samples of each of the composites using a dial gage fixture shown in Figure 66. The specimens were loaded in three point bending with the dial gage located at the point of loading. The beam deflection was limited to a maximum not exceeding the thickness of the specimen. The measured deflections and the deflections calculated from the crosshead speed and the chart speed agreed.

Analysis of the data can be accomplished by a number of methods. Among these are:

1. Compliance change [45].
2. Linear beam analysis.
3. Nonlinear beam analysis [41].
4. Empirical analysis [46].

Whitney, et al. [47] have investigated the applicability of each of these methods for calculating G_{IC}

based on the assumptions required for their utilization. They determined that the compliance change method was the most direct approach to use in the calculation of G_{IC} values. The only assumption made is that all of the energy change goes into interlaminar crack propagation. This is the analysis that was used to calculate the values in this study.

APPENDIX E

DROP WEIGHT IMPACT TEST

Many tests have traditionally been used to assess impact resistance of materials including the simple and inexpensive Charpy, Izod and falling dart tests. The Charpy and Izod tests are constrained significantly by sample geometry and dimension and the results available from these tests are not really applicable as models for end-use conditions because there are significant edge effects [48] and geometry effects [49] which are not present in real structural components.

Both the neat resins and the composites, having these neat resins as matrices, were impact tested with an instrumented Dynatup Falling Weight Impact Tester. Automated electronic data analysis in the Dynatup system provides graphical and tabular records of applied load and energy absorbed as functions of either time or specimen deflection during impact. Impact performance can be evaluated in terms of all of the characteristics of the fracture process. For example, total absorbed energy is simply segmented into that required for initiating failure and that for propagating the failure. The drop weight impact test requires the use of a relatively

large sample, but past experience seems to indicate that it produces more realistic impact modeling than either the Izod or Charpy tests.

The impact test machine is shown in Figure 67. It is composed of a weighted crosshead containing a 0.50 inch (1.27 cm) diameter cylindrical penetrator with a spherical end. Figure 68 shows the details of the penetrator configuration and the mode of interaction with the sample. The penetrator is fitted with strain gages which measure the load history experienced by the penetrator as the impact event occurs. By varying the height from which the crosshead is dropped and the weight of the crosshead, a wide range of impacting energies can be produced using this machine. The rest of the system functions include: direct measurement and computation of pretest parameters, use of transient recording methods, microprocessor analysis of raw data, temporary storage of the analyzed results of a series of lists, permanent storage of raw data on magnetic recording media (floppy disc recorder).

The load (P) is measured directly while energy (Q) and deflection (d) are incrementally calculated from the measured velocity at the start of impact (V), known crosshead weight (W), and the load value. The recording of the load is initiated by a fiber optics flag/detector

assembly which also measures the velocity of the cross-head at impact. The relationships utilized for these calculations are:

$$v_i = v_{i-1} + g \frac{P_{i-1}}{W} \Delta t \tag{24}$$

$$\bar{v} = \frac{1}{2} (v_i + v_{i-1}) \tag{25}$$

$$d_i = d_{i-1} + \bar{v}_i \Delta t \tag{26}$$

$$O_i = O_{i-1} + \frac{1}{2} W (v_{i-1}^2 - v_i^2) Wg \Delta x \tag{27}$$

subscript i = increment being calculated

subscript i-1 = previous increment

g = acceleration due to gravity

TABLE 1

MECHANICAL PROPERTIES OF CELION 6000 GRAPHITE FIBER

Lot Number	1231	2531
Modulus, MSI (GN/m^2)	34.4 (3.5)	34.7 (3.7)
Tensile Strength, KSI (MN/m^2)	513 (237.2)	533 (239)
Elongation, Percent	1.49	1.54

TABLE 2

PROCESSING PARAMETERS FOR COMPOSITE LAMINATES

Matrix Material	Temperature °C	Pressure PSI (MN/m^2)	Cure Time HR
930	350	200[B] (1.4)	2
P-1700	650	500 (3.4)	1
840	121	2[B] (0.014)	2
956	100	1.5[B](.010)	1.5

A. Plies placed into a cold mold and heated to temperature at a rate of 2-3°C per minute.
B. Pressure slowly increased to level which produced slight flashing of resin. After gelling reached desired stage, maximum pressure was applied.

TABLE 3

TENSILE PROPERTIES OF RESINS

Resin	Modulus KSI(GN/m^2)	Strength KSI(MN/m^2)	Yield Strain	Ultimate Strain	Poisson's Ratio
930	657 (4.53)	12.9(88.9)	----	0.019	0.36
P-1700	344.6(2.40)	11.9(82.0)	0.057	0.50*	0.37
840	255 (1.76)	4.9(33.8)	0.03	0.35	0.44
956	160 (1.10)	3.2(22.0)	0.05	0.50	0.365

*Local necking precedes fracture

TABLE 4

INTRALAMINAR SHEAR PROPERTIES OF COMPOSITES

MEASURED BY A TEN DEGREE OFF-AXIS TENSILE TEST

Matrix	K_{vf}	Initial Modulus KSI(GN/m^2)b	Strength KSI(MN/m^2)	Max. Strain
930	0.509	560(3.86)	9.72(67.0)	0.0107
P-1700	0.615	359(2.48)	4.36(30.1)	0.0325
840	0.556	273(1.88)	7.50(51.7)	0.0225
956	0.528	174(1.20)	6.36(43.8)	0.0540

TABLE 5

COMPRESSION PROPERTIES OF RESINS

Resin	Modulus KSI(GN/m^2)	Strength at Yield KSI(MN/m^2)	Strain at Yield	Poisson's Ratio
930	598 (4.12)	26.0(179.3)	0.033	0.360
P-1700	365 (2.52)	13.6 (93.8)	0.060	0.389
840	301 (2.10)	9.0 (62.0)	0.042	0.396
956	164 (1.13)	8.2 (56.5)	0.058	0.411

TABLE 6

RESIN DENSITIES MEASURED BY WATER IMMERSION

Resin	Density(gm/cc)	Standard Deviation
930	1.335	±0.001
P-1700	1.240	±0.001
840	1.146	±0.012
956	1.179	±0.008

TABLE 7

RESIN RELAXATION TEST DATA

Resin	T_g (°C)	Initial Stress PSI (KN/m^2)	Initial Strain	Relaxation Time* MIN
930	121.0	2639 (11.74)	0.0050	55,065
P-1700	187.0	3495 (15.54)	0.0880	30,608
840	58.5	1283 (5.71)	0.0054	2,955**
956	42.8	736 (3.27)	0.0036	1,863**

* Relaxation times calculated assuming each resin has only one relaxation time.

**Relaxation time calculated at 1000 hours.

TABLE 8

GLASS TRANSITION TEMPERATURES (Tg) OF NEAT RESINS AND COMPOSITES AS MEASURED BY DYNAMIC MECHANICAL ANALYSIS

Resin or Matrix	Strain Rate Radians/Sec	Resin Tg, °F (°C)		Composite Tg, °F (°C)	
		G"*	Tan**	G"*	Tan**
930	0.1	241 (116.5)	270 (132)	244 (117.5)	292 (141)
930	6.28	268 (131)	297 (144)	246 (119)	270 (132)
P-1700	0.1	378 (192)	378 (192)	378 (192)	378 (192)
840	0.1	108 (42)	126 (52)	115 (46)	128 (53)
840	6.28	115 (46.5)	136 (58)	138 (59)	153 (67.5)
956	0.1	100 (38)	115 (46)	107 (41.5)	115 (46)
956	6.28	109 (43)	123 (51)	122 (49)	130 (54)

* Temperature at the maximum of the G" curve.

**Temperature at the maximum of the tangent delta curve.

TABLE 9

DYNAMIC MODULI OF POLYMERS AND COMPOSITES AT DIFFERENT STRAIN RATES AND A MAXIMUM STRAIN OF 0.1

Polymer or Composite	Strain Rate	G' KSI	G' GN/m^2	G" KSI	G" GN/m^2	E'(Calc) KSI	E'(Calc) GN/m^2
930	0.01	236.4	1.63	4.4	0.30	642.9	4.43
	0.10	245.0	1.69	3.7	0.25	666.4	4.59
	1.00	248.0	1.71	3.2	0.21	674.6	4.65
	10.00	252.3	1.74	3.3	0.22	686.3	4.73
	100.00	255.2	1.76	---	----	694.1	4.79
P-1700	0.01	134.6	0.92	2.2	0.15	370.0	2.55
	0.10	136.6	0.94	1.4	0.09	375.6	2.59
	1.00	138.6	0.95	1.2	0.08	381.2	2.63
	10.00	139.9	0.96	1.1	0.07	384.7	2.65
	100.00	140.6	0.97	1.1	0.07	386.8	2.67
840	0.01	82.6	0.57	18.0	1.24	225.6	1.56
	0.10	109.0	0.75	14.9	1.03	301.6	2.18
	1.00	128.3	0.88	12.8	0.88	348.2	2.40
	10.00	145.0	1.00	11.3	0.78	394.4	2.72
	100.00	161.0	1.11	10.8	0.75	437.8	3.02
956	0.01	52.2	0.36	11.3	0.78	146.2	1.00
	0.10	62.4	0.43	10.2	0.70	174.7	1.20
	1.00	79.0	0.54	9.3	0.64	221.2	1.52
	10.00	92.2	0.63	8.7	0.60	258.2	1.78
	100.00	104.1	0.71	8.6	0.59	291.5	2.01
930/	0.01	1063.5	7.36	33.6	0.23		
Celion	0.10	1100.6	7.59	22.4	0.15		
	1.00	1120.8	7.73	21.7	0.15		
	10.00	1138.2	7.85	18.2	0.13		
	100.00	1151.3	7.94	17.8	0.12		
P-1700/	0.01	725.0	5.00	23.2	0.16		
Celion	0.10	743.2	5.13	11.6	0.08		
	1.00	758.0	5.23	7.3	0.05		
	10.00	765.0	5.28	7.3	0.05		
	100.00	768.0	5.30	4.3	0.03		
840/	0.01	658.3	4.54	61.7	0.43		
Celion	0.10	726.5	5.01	46.4	0.32		
	1.00	774.3	5.34	38.0	0.26		
	10.00	812.0	5.60	31.9	0.22		
	100.00	845.4	5.83	30.5	0.21		
956/	0.01	416.2	2.87	185.9	1.28		
Celion	0.10	464.0	3.20	140.8	0.98		
	1.00	523.4	3.63	114.7	0.79		
	10.00	580.0	4.00	92.9	0.64		
	100.00	623.5	4.30	83.1	.057		

TABLE 10

DYNAMIC MODULI OF RESINS AT

DIFFERENT STRAIN RATES AND STRAINS

Polymer	Frequency Radians/Sec	Strain Percent	G' KSI	G' GN/m^2	G" KSI	G" GN/m^2
930	1.0	0.1	285.0	1.967	3.03	2.093
	1.0	0.5	282.5	1.948	4.96	3.420
	1.0	1.0	285.4	1.982	5.09	3.510
	10.0	0.1	290.0	2.000	2.75	1.895
	10.0	0.5	286.8	1.978	4.13	2.845
	10.0	1.0	281.0	1.945	5.03	3.469
	100.0	0.1	293.0	2.021	3.77	2.600
	100.0	0.5	290.0	2.000	4.90	3.380
	100.0	1.0	284.2	1.960	5.48	3.780
P-1700	1.0	0.1	143.0	0.986	0.92	0.634
	1.0	0.5	142.0	0.979	1.16	0.798
	1.0	1.0	140.4	0.968	1.61	1.13
	10.0	0.1	144.0	0.993	0.69	0.476
	10.0	0.5	143.0	0.986	0.96	0.662
	10.0	1.0	141.2	0.974	1.41	0.971
	100.0	0.1	144.6	0.997	0.83	0.574
	100.0	0.5	143.6	0.990	1.01	0.693
	100.0	1.0	141.8	0.978	1.32	0.910
840	1.0	0.1	120.1	0.812	13.18	9.090
	1.0	0.5	123.1	0.848	13.66	9.420
	1.0	1.0	130.9	1.03	14.79	10.200
	10.0	0.1	141.4	0.975	11.60	8.000
	10.0	0.5	138.7	0.957	12.05	8.310
	10.0	1.0	165.3	1.14	13.48	9.300
	100.0	0.1	156.6	1.08	11.24	7.750
	100.0	0.5	152.3	1.05	11.77	8.120
	100.0	1.0	174.0	1.20	12.89	8.890
956	1.0	0.1	94.9	0.655	9.16	6.320
	1.0	0.5	94.2	0.650	9.32	6.430
	1.0	1.0	92.1	0.635	9.63	6.640
	10.0	0.1	108.0	0.745	8.53	5.880
	10.0	0.5	106.7	0.736	8.77	6.050
	10.0	1.0	103.4	0.713	9.16	6.320
	100.0	0.1	120.0	0.828	8.64	5.960
	100.0	0.5	117.2	0.808	8.93	6.160
	100.0	1.0	111.2	0.767	9.25	6.380

TABLE 11

GLASS TRANSITION TEMPERATURES AND THERMAL EXPANSION COEFFICIENTS OF POLYMERS AS MEASURED BY TMA

Polymer	Type of Resin	Processing Temp. °F	Processing Temp. °C	T_G °F	T_G °C	Coefficient of Thermal Expansion in/in °F	Coefficient of Thermal Expansion mm/mm °C	Temperature Range or Temperature °F	Temperature Range or Temperature °C
930	Epoxy	350	177	250	121	30.6×10^{-6} 42.1×10^{-6}	55.0×10^{-6} 75.8×10^{-6}	70-158 241	21- 70 116
P-1700	Polysulfone	650	343	369	187	32.9×10^{-6} 36.1×10^{-6} 38.1×10^{-6}	59.2×10^{-6} 65.0×10^{-6} 68.6×10^{-6}	90-284 284-305 305-366	32-140 140-152 152-185
840	Epoxy	250	121	137	58.5	55.0×10^{-6} 78.6×10^{-6} 83.8×10^{-6}	99.1×10^{-6} 141.4×10^{-6} 150.9×10^{-6}	86 122 131	30 50 55
956	Epoxy	212	100	109	42.8	43.9×10^{-6}	79.0×10^{-6}	70-102	21- 39

TABLE 12

COEFFICIENTS OF THERMAL EXPANSION OF

CROSSPLIED CELION 6000 REINFORCED COMPOSITES

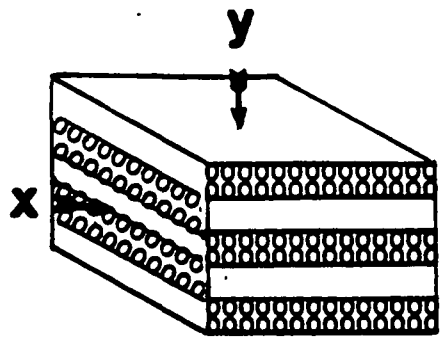

Matrix	Direction	Fiber Volume %	T °C	T °F	Coefficient of Thermal Expansion mm/mm°C	Coefficient of Thermal Expansion in/in °F
930	X	58.6	44	111	3.3×10^{-6}	1.8×10^{-6}
	Y		44	111	66.0×10^{-6}	36.6×10^{-6}
P-1700	X	60.7	98	208	1.2×10^{-6}	0.6×10^{-6}
	Y		98	208	38.0×10^{-6}	21.1×10^{-6}
840	X	71.5	26	79	2.5×10^{-6}	1.3×10^{-6}
	Y				78.1×10^{-6}	43.4×10^{-6}
956	X	67.1	16	61	5.2×10^{-6}	2.9×10^{-6}
	Y		16	61	127.0×10^{-6}	67.8×10^{-6}

TABLE 13

COEFFICIENTS OF THERMAL EXPANSION OF

UNIDIRECTIONAL CELION 6000 REINFORCED COMPOSITES

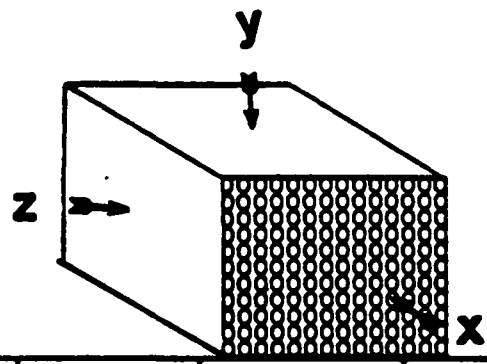

Matrix	Direction	Fiber Volume %	T °F	T °C	Coefficient of Thermal Expansion mm/mm°C	Coefficient of Thermal Expansion in/in °F
930	X	61.9	111	44	-0.3×10^{-6}	-0.2×10^{-6}
	Y	61.9	111	44	36.1×10^{-6}	20.0×10^{-6}
	Z	61.9	111	44	30.1×10^{-6}	16.7×10^{-6}
P-1700	X	60.8	208	98	0.9×10^{-6}	0.5×10^{-6}
	Y	60.8	208	98	35.3×10^{-6}	19.6×10^{-6}
	Z	60.8	208	98	28.8×10^{-6}	16.0×10^{-6}
840	X	68.0	79	26	3.2×10^{-6}	1.8×10^{-6}
	Y	68.0	79	26	69.0×10^{-6}	38.3×10^{-6}
	Z	68.0	79	26	68.5×10^{-6}	38.0×10^{-6}
956	X	67.0	61	16	-1.9×10^{-6}	-1.0×10^{-6}
	Y	67.0	61	16	62.4×10^{-6}	34.7×10^{-6}
	Z	67.0	61	16	64.4×10^{-6}	35.8×10^{-6}

TABLE 14

RESIN IMPACT TEST DATA

Resin	Maximum Load Lb (N)	Maximum Energy Ft-Lb (J)	Load Carried By Membrane Action Percent	Thickness In (Cm)	Maximum Deflection In (Cm)
930	150 (667)	1.0 (1.4)	15.8	.112 (.284)	.140 (.346)
P-1700	750 (3336)	15.0 (20.3)	77.2	.118 (.300)	.700 (1.778)
840	185 (823)	2.2 (3.0)	38.7	.134 (.342)	.308 (.782)
956	443 (1970)	6.5 (8.8)	53.6	.130 (.330)	.400 (1.016)

TABLE 15

UNIDIRECTIONAL COMPOSITE IMPACT TEST LOAD DATA

Matrix	Thickness In (Cm)	K_{vf}	P_i Lb^i(N)	P_m LB^m(N)	Maximum Deflection In (Cm)
930	.107 (.256)	.520	764 (3398)	764 (3398)	.307 (0.780)
930	.107 (.256)	.520	567 (2522)	600 (2669)	.314 (0.798)
P-1700	.094 (.239)	.598	599 (2664)	599 (2664)	.336 (0.853)
P-1700	.094 (.239)	.598	450 (2002)	512 (2277)	.329 (0.836)
P-1700	.099 (.251)	.580	525 (2348)	542 (2411)	.290 (0.737)
840	.131 (.332)	.420	670 (2980)	670 (2980)	.289 (0.734)
840	.131 (.332)	.420	630 (2802)	630 (2802)	.256 (0.650)
840	.087 (.221)	.638	367 (1632)	392 (1744)	.400 (1.016)
840	.087 (.221)	.638	556 (2473)	609 (2709)	.488 (1.240)
956	.143 (.363)	.390	804 (3560)	804 (3560)	.278 (0.706)
956	.143 (.363)	.390	691 (3074)	691 (3074)	.314 (0.798)
956	.107 (.272)	.548	538 (2393)	556 (2473)	.305 (0.775)
956	.107 (.272)	.548	600 (2669)	611 (2718)	.355 (0.902)

TABLE 16

UNIDIRECTIONAL COMPOSITE IMPACT TEST LOAD

DATA NORMALIZED TO 60 VOLUME PERCENT FIBER

Matrix	Thickness In (Cm)	K_{vf}	P_i Lb (N)	P_m Lb (N)
930	.107 (.256)	.520	882 (3921)	882 (3921)
930	.107 (.256)	.520	654 (2910)	692 (3080)
P-1700	.094 (.239)	.598	601 (2673)	601 (2673)
P-1700	.094 (.239)	.598	452 (2009)	514 (2285)
P-1700	.099 (.251)	.580	543 (2429)	561 (2494)
840	.131 (.332)	.470	957 (4257)	957 (4257)
840	.131 (.332)	.470	900 (4003)	900 (4003)
840	.087 (.221)	.638	345 (1535)	369 (1640)
840	.087 (.221)	.638	523 (2326)	573 (2548)
956	.143 (.363)	.390	1237 (5477)	1237 (5477)
956	.143 (.363)	.390	1063 (4729)	1063 (4729)
956	.107 (.272)	.548	600 (2669)	609 (2708)
956	.107 (.272)	.548	657 (2922)	669 (2976)

TABLE 17

UNIDIRECTIONAL COMPOSITE IMPACT TEST ENERGY DATA

Matrix	Thickness In (Cm)	K_{vf}	Q_i Ft-Lb(J)	Q_m Ft-Lb(J)	Q_f Ft-Lb(J)
930	.107 (.256)	.520	8.8 (11.8)	8.8 (11.8)	14.5 (19.7)
930	.107 (.256)	.520	7.5 (10.2)	7.5 (10.2)	11.0 (14.9)
P-1700	.094 (.239)	.598	8.8 (11.9)	8.8 (11.9)	17.0 (23.0)
P-1700	.094 (.239)	.598	5.0 (6.8)	8.4 (11.3)	15.1 (20.5)
P-1700	.099 (.251)	.580	6.8 (9.2)	6.8 (9.2)	25.0 (35.1)
840	.131 (.332)	.420	7.8 (10.6)	7.8 (10.6)	18.0 (24.4)
840	.131 (.332)	.420	7.8 (10.6)	8.2 (11.1)	18.0 (24.4)
840	.087 (.221)	.638	5.0 (6.8)	6.7 (9.1)	19.0 (25.8)
840	.087 (.221)	.638	8.6 (11.7)	12.5 (17.0)	11.5 (15.6)
956	.143 (.363)	.390	10.0 (13.6)	10.0 (13.6)	21.0 (28.5)
956	.143 (.363)	.390	9.1 (12.3)	9.1 (12.3)	15.0 (20.3)
956	.107 (.272)	.548	6.8 (9.2)	10.1 (13.7)	16.0 (21.7)
956	.107 (.272)	.548	7.5 (10.2)	12.5 (16.9)	15.0 (20.3)

TABLE 18

UNIDIRECTIONAL COMPOSITE IMPACT TEST ENERGY DATA

NORMALIZED TO 60 VOLUME PERCENT FIBER

Matrix	Thickness In (Cm)	K_{vf}	Q_f Ft-Lb(J)	Q_m Ft-Lb(J)	Q_f Ft-Lb(J)
930	.107 (.256)	.520	10.2 (13.6)	10.2 (13.6)	16.7 (22.7)
930	.107 (.256)	.520	8.7 (11.8)	8.7 (7.5)	12.7 (17.2)
P-1700	.094 (.239)	.598	8.8 (11.9)	8.8 (11.9)	17.1 (23.1)
P-1700	.094 (.239)	.598	5.0 (6.8)	5.0 (6.8)	15.2 (20.6)
P-1700	.099 (.251)	.580	7.0 (9.5)	6.8 (9.5)	25.9 (35.2)
840	.131 (.332)	.420	11.1 (15.1)	11.1 (15.1)	25.7 (34.9)
840	.131 (.332)	.420	11.1 (15.1)	11.7 (15.9)	25.7 (34.9)
840	.087 (.221)	.638	4.7 (6.4)	6.3 (8.6)	17.9 (24.3)
840	.087 (.221)	.638	8.1 (11.0)	11.8 (16.0)	10.8 (14.7)
956	.143 (.363)	.390	15.4 (20.9)	15.4 (20.9)	32.3 (44.0)
956	.143 (.363)	.390	14.0 (18.9)	14.0 (18.9)	23.1 (31.2)
956	.107 (.272)	.548	7.4 (10.1)	10.9 (15.0)	17.5 (23.8)
956	.107 (.272)	.548	8.2 (11.2)	13.7 (18.5)	16.4 (22.2)

TABLE 19

CROSSPLY COMPOSITE IMPACT TEST LOAD DATA

Matrix	Thickness In (Cm)	K_{vf}	P_i Lb^i (N)	P_m LB^m (N)	Maximum Deflection In (Cm)
930*	.174 (.442)	.746	2114 (9403)	2486 (11058)	.238 (.604)
930*	.175 (.444)	.746	2222 (9883)	2332 (10373)	.290 (.737)
930	.102 (.259)	.586	1033 (4595)	1033 (4595)	.204 (.518)
930	.099 (.251)	.586	1047 (4657)	1047 (4657)	.- ---
930	.120 (.305)	.443	910 (4048)	910 (4048)	.210 (.533)
930	.120 (.305)	.443	861 (3830)	861 (3830)	.290 (.737)
P-1700*	.168 (.428)	.703	1000 (4448)	1306 (5809)	.056 (.142)
P-1700*	.170 (.432)	.703	944 (4199)	1383 (6152)	.091 (.231)
P-1700	.101 (.256)	.607	826 (3674)	826 (3674)	.175 (.444)
P-1700	.102 (.259)	.607	869 (3865)	869 (3865)	.210 (.533)
P-1700	.094 (.239)	.651	775 (3447)	775 (3447)	.200 (.508)
P-1700	.094 (.239)	.651	742 (3300)	742 (3300)	.230 (.584)
840*	.190 (.483)	.598	1480 (6583)	1930 (8584)	.112 (.286)
840*	.202 (.513)	.602	1601 (7121)	2118 (9420)	.100 (.254)
840	.088 (.224)	.715	800 (3558)	1037 (4613)	.200 (.508)
840	.088 (.224)	.715	800 (3558)	1062 (4724)	.218 (.554)
840	.109 (.277)	.669	779 (3464)	779 (3464)	.150 (.381)
956*	.176 (.447)	.655	717 (3189)	1879 (8358)	.056 (.142)
956*	.174 (.442)	.655	1222 (5435)	2058 (9154)	.076 (.193)
956	.099 (.252)	.671	800 (3558)	1037 (4613)	.160 (.406)
956	.089 (.276)	.671	726 (3229)	1200 (5338)	.160 (.406)
956	.143 (.363)	.442	585 (2602)	1250 (5560)	.100 (.254)
956	.150 (.381)	.442	650 (2891)	785 (3492)	.143 (.363)

*Limited energy impact tests

TABLE 20

CROSSPLY COMPOSITE IMPACT TEST LOAD DATA

NORMALIZED TO 60 VOLUME PERCENT FIBER

Matrix	Thickness In (Cm)	K_{vf}	P_i Lb (N)	P_m LB (N)
930*	.174 (.442)	.746	1700 (7563)	2000 (8894)
930*	.175 (.444)	.746	1787 (7949)	1876 (8343)
930	.102 (.259)	.586	1058 (4705)	1058 (4705)
930	.099 (.251)	.586	1072 (4768)	1072 (4768)
930	.120 (.305)	.443	1232 (5483)	1232 (5483)
930	.120 (.305)	.443	1166 (5187)	1166 (5187)
P-1700*	.168 (.428)	.703	854 (3796)	1115 (4958)
P-1700*	.170 (.432)	.703	806 (3584)	1180 (5251)
P-1700	.101 (.256)	.607	826 (3674)	826 (3674)
P-1700	.102 (.259)	.607	869 (3865)	869 (3865)
P-1700	.094 (.239)	.651	714 (3177)	714 (3177)
P-1700	.094 (.239)	.651	684 (3041)	684 (3041)
840*	.190 (.483)	.598	1485 (6605)	1936 (8613)
840*	.202 (.513)	.602	1606 (7145)	2125 (9452)
840	.088 (.224)	.715	671 (2986)	870 (3871)
840	.088 (.224)	.715	671 (2986)	891 (3964)
840	.109 (.277)	.669	699 (3107)	699 (3107)
956*	.176 (.447)	.655	657 (2921)	1721 (7656)
956*	.174 (.442)	.655	1119 (4979)	1885 (8385)
956	.099 (.252)	.671	715 (3182)	927 (4125)
956	.089 (.276)	.671	649 (2887)	1073 (4773)
956	.143 (.363)	.442	794 (3532)	1697 (7547)
956	.150 (.381)	.442	882 (3924)	1066 (4740)

*Limited energy impact tests

TABLE 21

CROSSPLY COMPOSITE IMPACT TEST ENERGY AND DAMAGE AREA DATA

Matrix	Thickness In (Cm)	K_{vf}	Q_i Ft-Lb(J)	Q_m Ft-Lb(J)	Damage Area In^2 (Cm^2)
930*	.174 (.442)	.746	26.1 (35.1)	30.1 (40.8)	0.67 (4.32)
930*	.174 (.444)	.746	20.5 (27.8)	32.2 (43.7)	0.75 (4.84)
930	.102 (.259)	.586	8.6 (11.7)	8.6 (11.7)	1.10 (7.10)
930	.099 (.251)	.586	6.2 (8.4)	9.4 (12.8)	1.23 (7.94)
930	.120 (.305)	.443	8.8 (11.9)	8.8 (11.9)	0.81 (5.22)
P-1700*	.168 (.428)	.703	6.3 (8.5)	12.6 (17.2)	1.00 (6.45)
P-1700*	.170 (.432)	.703	6.7 (9.1)	14.7 (20.1)	0.97 (6.26)
P-1700	.101 (.256)	.607	3.4 (4.6)	6.8 (9.3)	1.41 (9.09)
P-1700	.102 (.259)	.607	3.7 (5.0)	8.5 (11.6)	1.35 (8.71)
P-1700	.094 (.239)	.651	7.3 (10.0)	7.3 (10.0)	---- ----
P-1700	.094 (.239)	.651	6.9 (9.4)	6.9 (9.4)	1.41 (9.09)
840*	.190 (.483)	.598	5.1 (7.0)	22.6 (30.8)	2.20 (14.19)
840*	.202 (.513)	.602	6.4 (8.7)	30.4 (41.5)	2.35 (15.16)
840	.088 (.224)	.715	6.5 (8.9)	13.3 (18.2)	1.00 (6.45)
840	.088 (.224)	.715	7.4 (10.1)	14.5 (19.8)	1.00 (6.45)
840	.109 (.277)	.669	5.1 (7.0)	8.0 (10.9)	---- ----
956*	.176 (.447)	.655	2.9 (4.0)	28.7 (39.2)	2.62 (16.90)
956*	.174 (.442)	.655	1.7 (2.3)	30.1 (40.8)	2.80 (18.06)
956	.099 (.252)	.671	5.9 (8.0)	15.9 (21.7)	0.95 (6.13)
956	.089 (.276)	.671	5.6 (7.6)	15.6 (21.3)	1.00 (6.45)
956	.143 (.363)	.442	4.7 (6.4)	19.6 (26.8)	1.21 (7.80)
956	.150 (.381)	.442	5.0 (6.8)	16.5 (22.5)	---- ----

*Limited energy impact tests

TABLE 22

CROSSPLY COMPOSITE IMPACT TEST ENERGY DATA

NORMALIZED TO 60 VOLUME PERCENT FIBER

Matrix	Thickness In (Cm)	K_{vf}	Q_i Ft-Lb(J)	Q_m Ft-Lb(J)
930*	.174 (.442)	.746	21.0 (28.2)	24.2 (32.8)
930*	.174 (.444)	.746	16.5 (22.4)	25.9 (35.1)
930	.102 (.259)	.586	8.8 (12.0)	8.8 (12.0)
930	.099 (.251)	.586	6.3 (8.6)	9.6 (13.1)
930	.120 (.305)	.443	11.9 (16.1)	11.9 (16.1)
P-1700*	.168 (.428)	.703	5.4 (7.2)	10.8 (14.7)
P-1700*	.170 (.432)	.703	5.7 (7.8)	12.5 (17.2)
P-1700	.101 (.256)	.607	3.4 (4.5)	6.8 (9.3)
P-1700	.102 (.259)	.607	3.7 (5.0)	8.5 (11.6)
P-1700	.094 (.239)	.651	6.7 (9.2)	6.7 (9.2)
P-1700	.094 (.239)	.651	6.4 (8.7)	6.4 (8.7)
840*	.190 (.483)	.598	5.1 (7.0)	22.6 (30.8)
840*	.202 (.513)	.602	6.4 (8.7)	30.4 (41.5)
840	.088 (.224)	.715	5.5 (7.5)	11.2 (15.3)
840	.088 (.224)	.715	6.2 (8.5)	12.2 (16.6)
840	.109 (.277)	.669	4.6 (6.3)	7.2 (9.8)
956*	.176 (.447)	.655	2.7 (3.7)	26.3 (35.9)
956*	.174 (.442)	.655	1.6 (2.1)	27.6 (37.4)
956	.099 (.252)	.671	5.3 (7.2)	14.2 (19.4)
956	.089 (.276)	.671	5.0 (6.8)	13.9 (19.0)
956	.143 (.363)	.442	6.4 (8.7)	26.6 (36.4)
956	.150 (.381)	.442	6.8 (9.2)	22.4 (30.5)

*Limited energy impact tests

TABLE 23

COMPACT TENSILE SPECIMEN FRACTURE TOUGHNESS DATA FOR MATRIX RESINS

Resin	Thickness In (Cm)	K_{IC} $Lb/In^{-1.5}$ $(N/CM^{-1.5})$	G_{IC} $In\text{-}Lb/In^2$ (J/Cm^2)
930	0.250 (0.64)	1830 (2010)	2.50 (0.044)
930	0.250 (0.640)	1965 (2160)	2.88 (0.050)
930	0.250 (0.640)	1950 (2143)	(0.0500) (12.63)
P-1700	0.250 (0.640)	3799 (4175)	20.62 (0.361)
P-1700	0.250 (0.640)	3802 (4179)	20.65 (0.362)
P-1700	0.300 (0.762)	3821 (4199)	20.86 (0.365)
840	0.475 (1.207)	1725 (1895)	6.61 (0.116)
840	0.475 (1.207)	1744 (1917)	6.76 (0.118)
840	0.475 (1.207)	1733 (1905)	6.67 (0.117)
956	0.575 (1.460)	3195 (3511)	31.90 0.559
956	0.750 (1.905)	3225 (3544)	32.50 0.569
956	0.750 (1.905)	3218 (3536)	32.16 (0.563)

TABLE 24

DOUBLE CANTILEVER BEAM FRACTURE TOUGHNESS DATA FOR GRAPHITE FIBER REINFORCED COMPOSITES

Matrix	K_{vf}	K_{IC} $Lb/In^{-1.5}$ ($N/Cm^{-1.5}$)	G_{IC} $In\text{-}Lb/In^2$ (J/Cm^2)
930	.619	2147 (2358)	0.60 (0.010)
930	.722	2284 (2509)	1.08 (0.019)
930	.722	2263 (2486)	0.73 (0.013)
P-1700	.668	4780 (5250)	2.08 (0.036)
P-1700	.668	4880 (5360)	2.83 (0.050)
P-1700	.668	5299 (5820)	3.20 (0.056)
840	.630	4001 (4395)	1.18 (0.021)
840	.630	3946 (4334)	1.00 (0.0175)
840	.680	2500 (2746)	0.88 (0.015)
956	.366	9199 (10104)	6.10 (0.107)
956	.635	5005 (5497)	2.25 (0.040)
956	.635	4482 (4923)	2.35 (0.041)

TABLE 25

STATIC BENDING PROPERTY DATA FOR

FOUR DIFFERENT CROSSPLIED GRAPHITE COMPOSITES

Specimen	Thickness In (Cm)	K_{vf}	Flexural Strength KSI (MN/m^2)	Strain x10^{-3}	Flexural Modulus KSI (GN/m^2)
930	0.175 (0.44)	0.731	107.8 (743.3)	9.2	14.0 (96.5)
930	0.176 (0.447)	0.731	110.0 (758.4)	9.2	13.9 (95.8)
930	0.176 (0.447)	0.731	99.2 (635.7)	8.4	14.6 (100.7)
P-1700	0.175 (0.444)	0.741	114.7 (790.8)	10.4	14.3 (98.6)
P-1700	0.173 (0.439)	0.741	114.4 (788.2)	12.6	14.8 (102.0)
P-1700	0.172 (0.439)	0.741	107.6 (741.9)	9.4	11.6 (80.3)
840	0.198 (0.503)	0.598	58.2 (401.3)	7.3	11.0 (80.3)
840	0.199 (0.505)	0.598	58.0 (399.9)	7.2	10.9 (75.2)
840	0.197 (0.500)	0.598	55.3 (381.0)	6.6	12.0 (82.7)
956	0.168 (0.427)	0.655	52.3 (360.6)	8.4	10.6 (73.1)
956	0.169 (0.429)	0.655	56.5 (389.6)	8.5	11.4 (78.6)
956	0.169 (0.429)	0.655	49.6 (342.0)	7.6	11.7 (80.7)

TABLE 26

CROSSPLIED COMPOSITE STATIC COMPRESSION TEST DATA

Matrix	K_{vf}	Compression Strength	
		Lb/in^2	MN/m^2
930	.586	60.33	416.0
930	.443	61.67	425.2
P-1700	.607	57.38	395.6
840	.715	62.22	429.0
840	.531	56.32	388.3
956	.586	54.10	373.0
956	.442	50.60	348.9

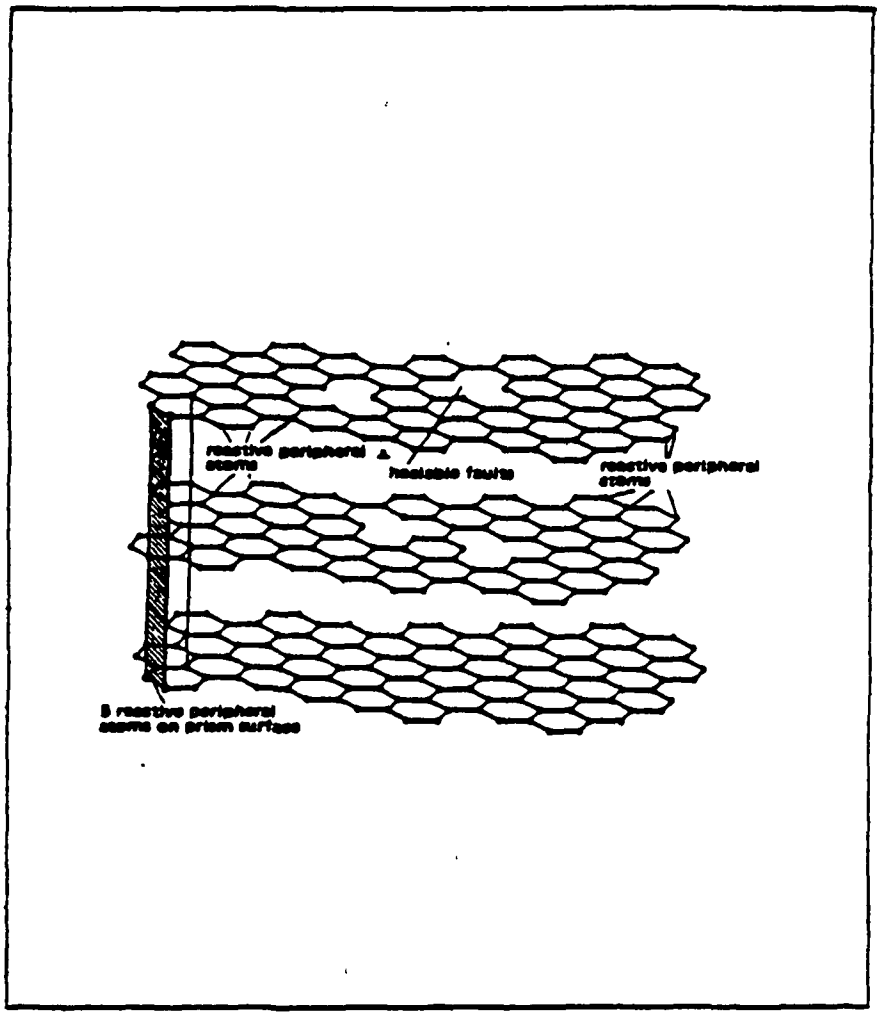

Figure 1. Schematic of graphite fiber surface showing free vacancies of graphitic carbon atoms where oxides become attached [19].

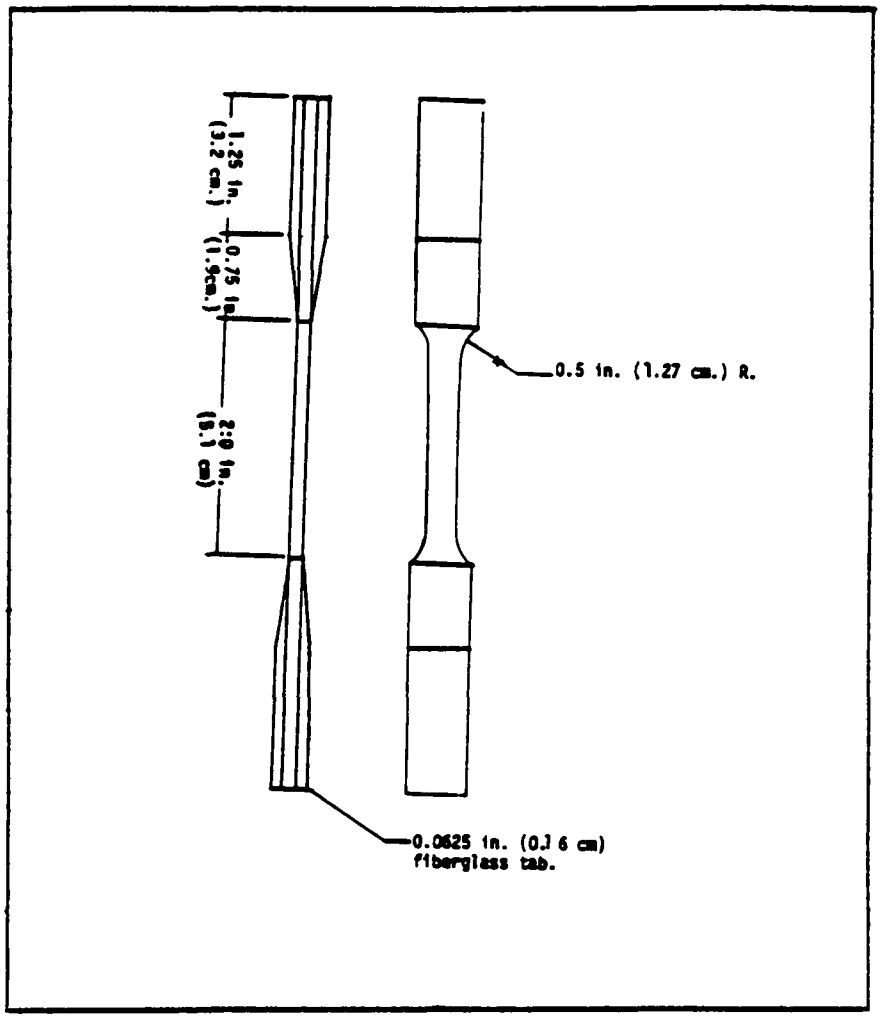

Figure 2. Dog bone tensile test specimen.

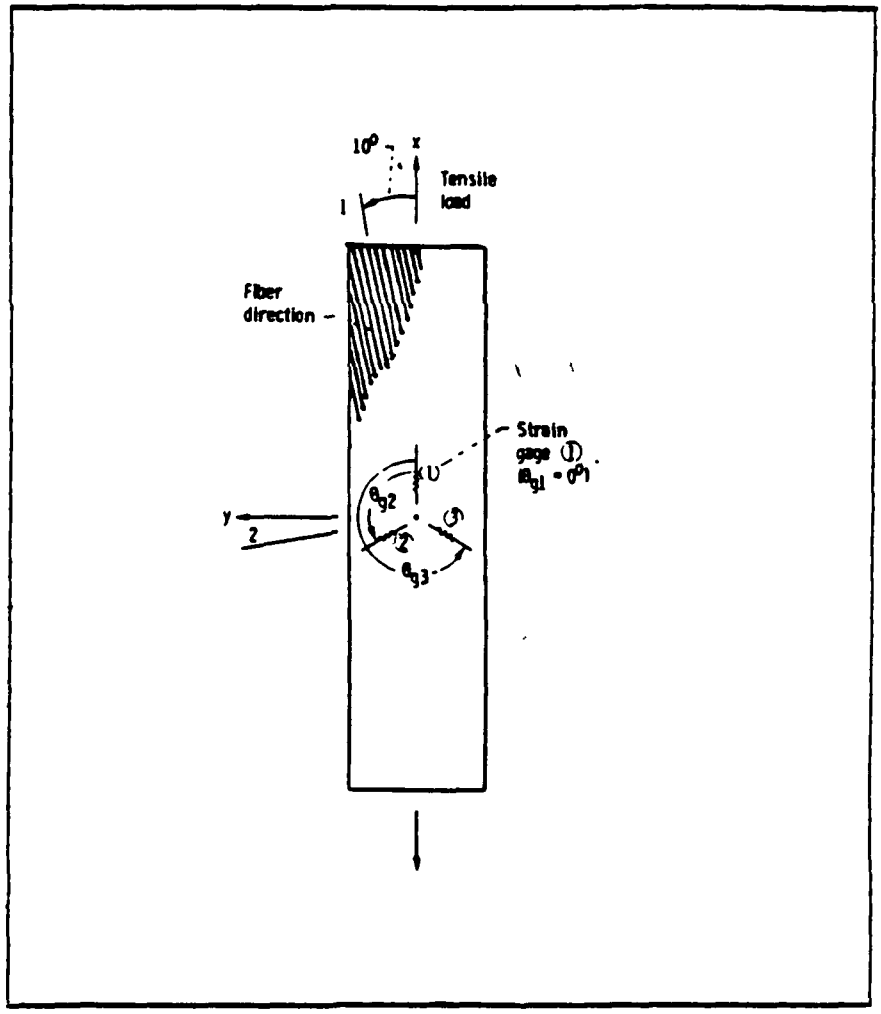

Figure 3. Schematic of the ten degree off-axis tensile test specimen and the 60° rosette strain gage orientation.

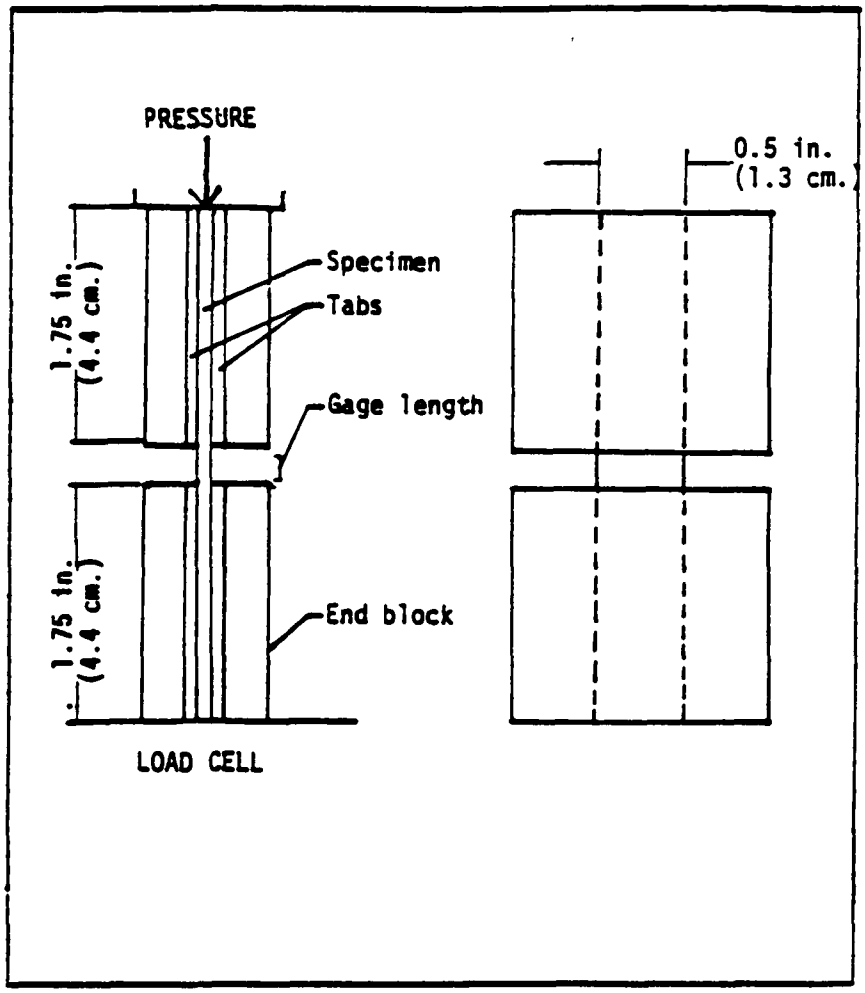

Figure 4. Schematic of the composite compression test fixture and specimen.

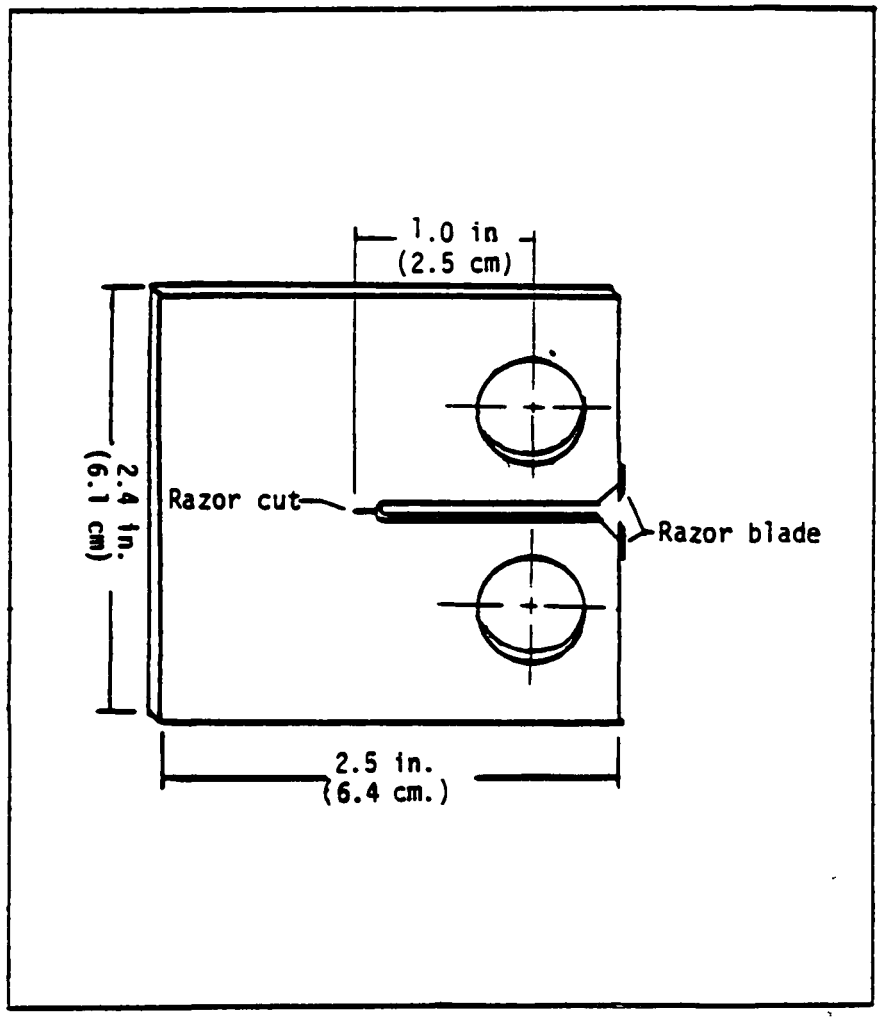

Figure 5. Schematic of the resin compact tensile test specimen for Mode I fracture toughness measurement.

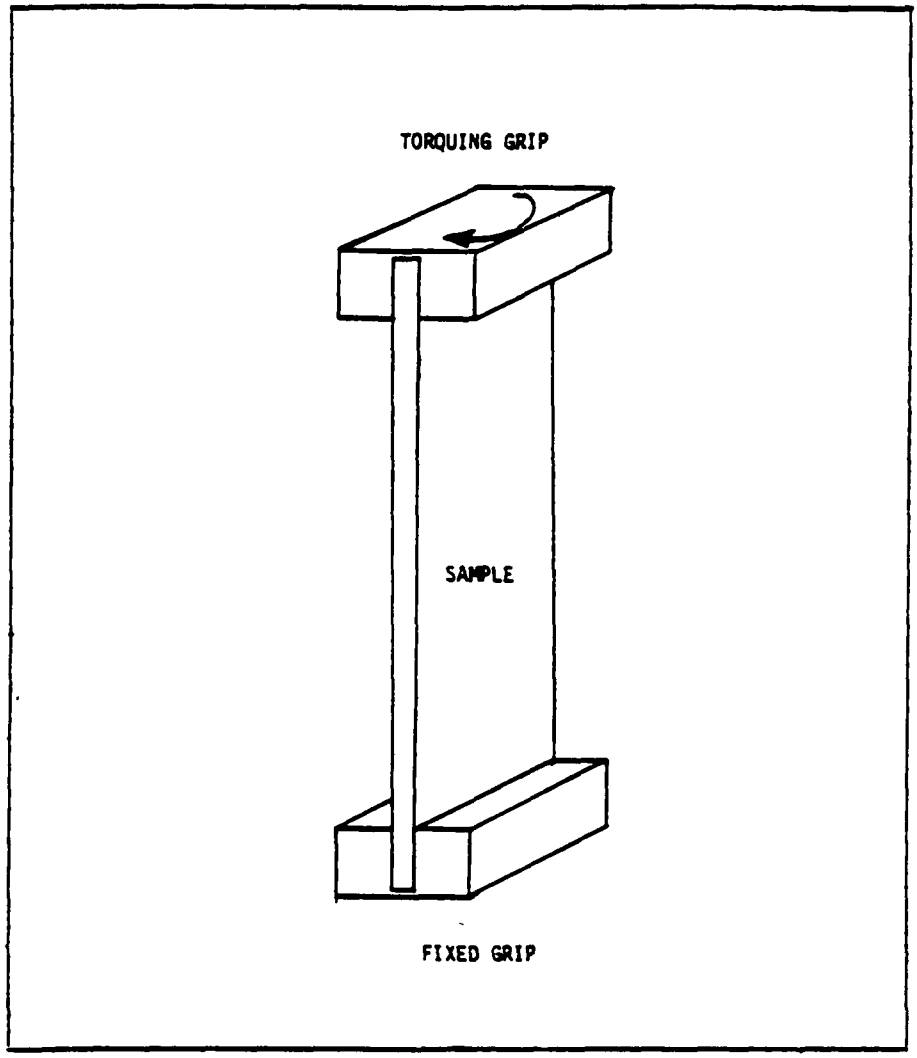

Figure 6. Schematic of the dynamic mechanical analyzer for measurement of dynamic shear moduli.

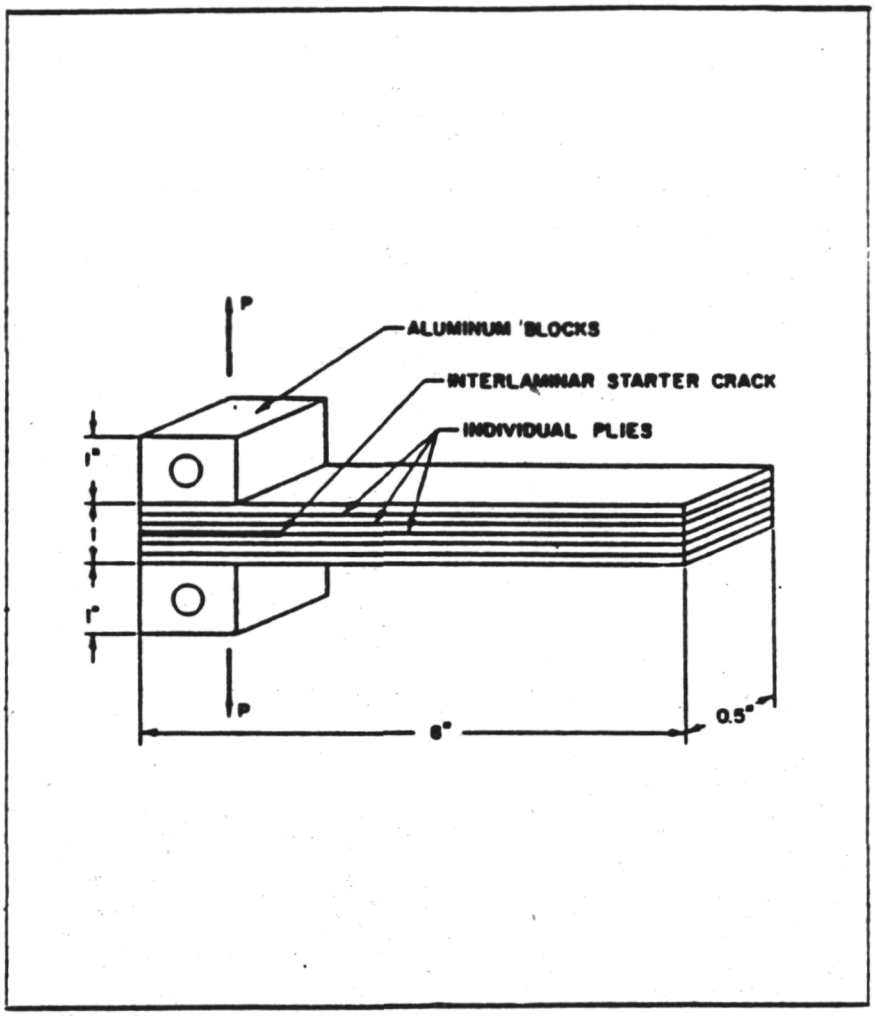

Figure 7. Schematic of the double cantilever beam specimen for measurement of the unidirectional composite Mode I fracture toughness.

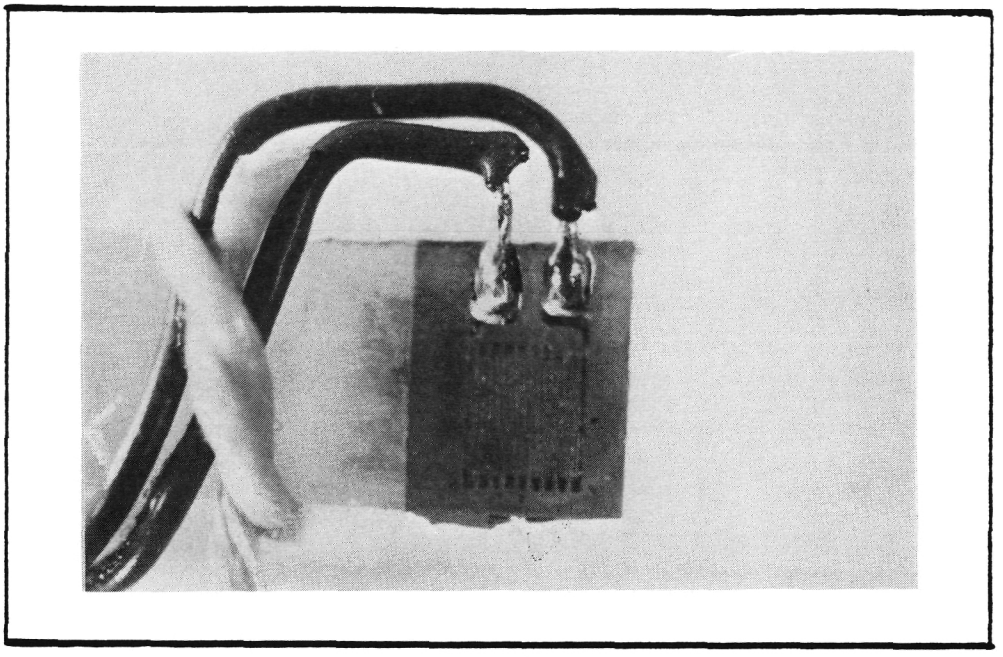

(a) Magnification 2X

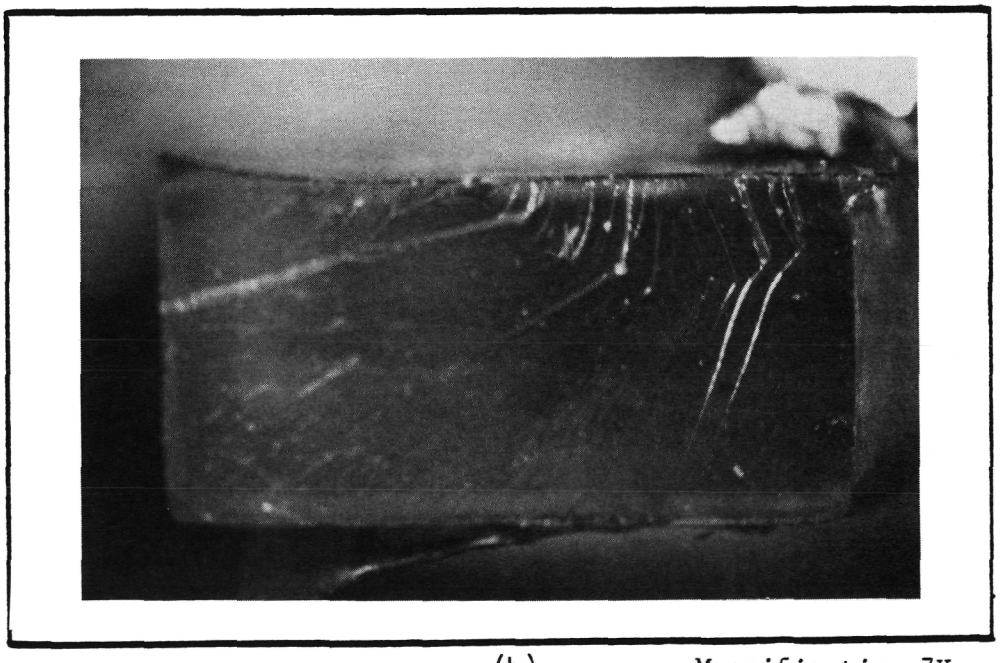

(b) Magnification 7X

Figure 8. P-1700 tensile test specimen. Typical fracture at the edge of the bonded strain gage. (a) Side view. (b) Fracture surface.

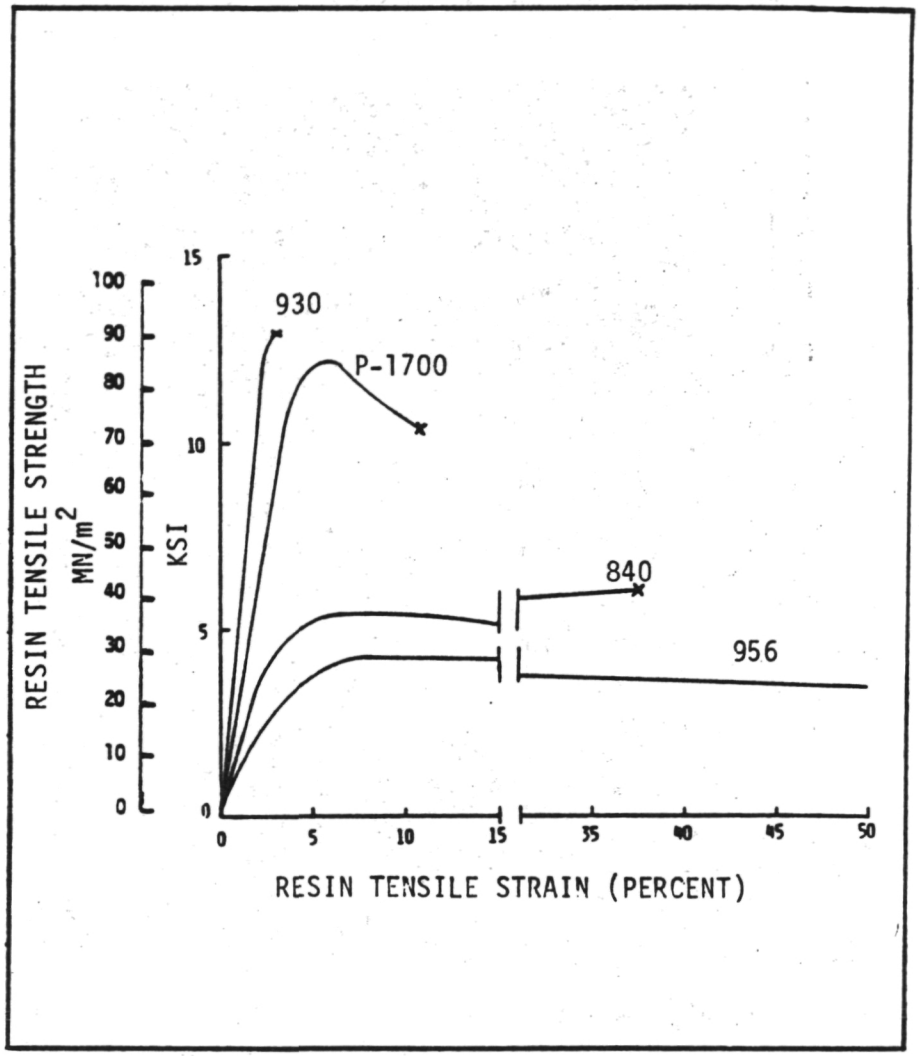

Figure 9. Tensile stress - strain curves for the composite matrix polymers used in this study.

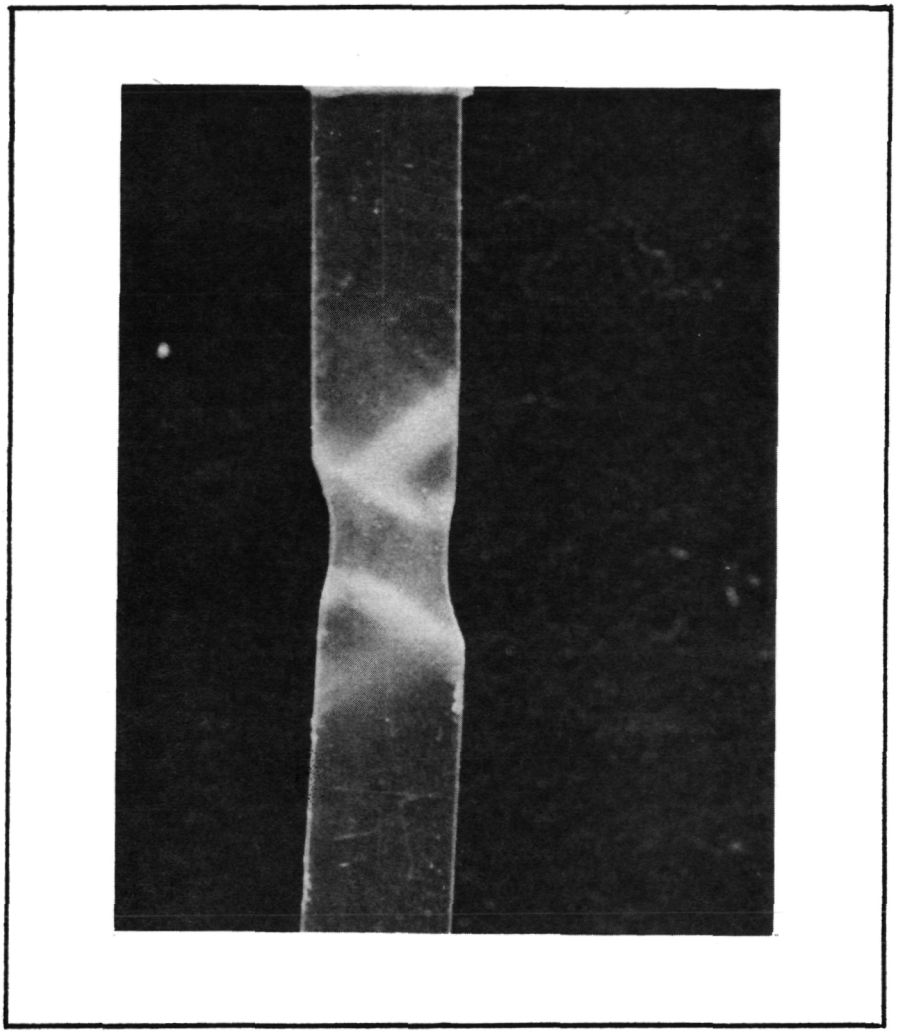

Magnification 1.5X

Figure 10. Localized necking of the P-1700 tensile test specimen. This is typical for a tough polymer.

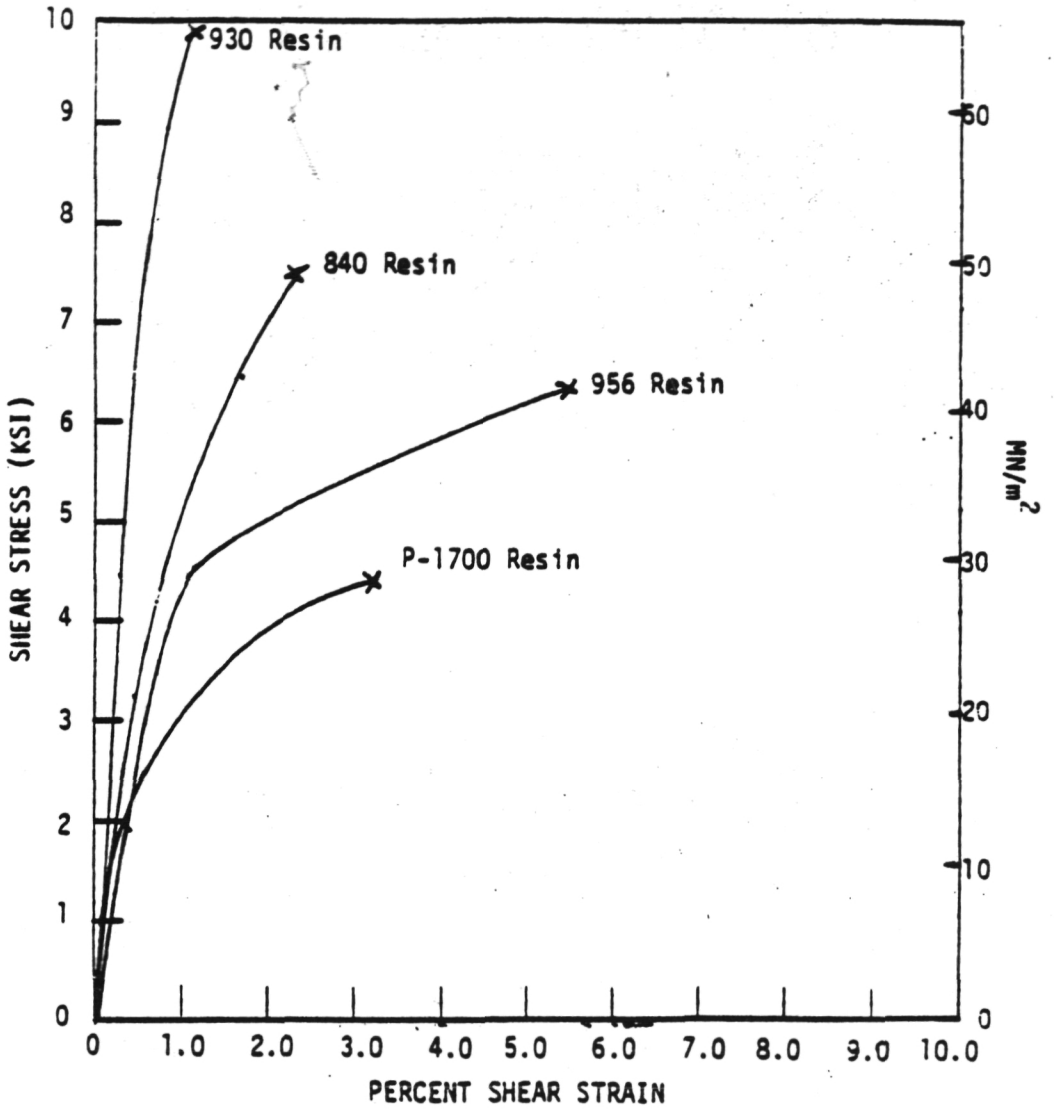

Figure 11. Unidirectional graphite fiber reinforced polymer matrix composite shear stress-strain curves as measured by the ten degree off-axis tensile test.

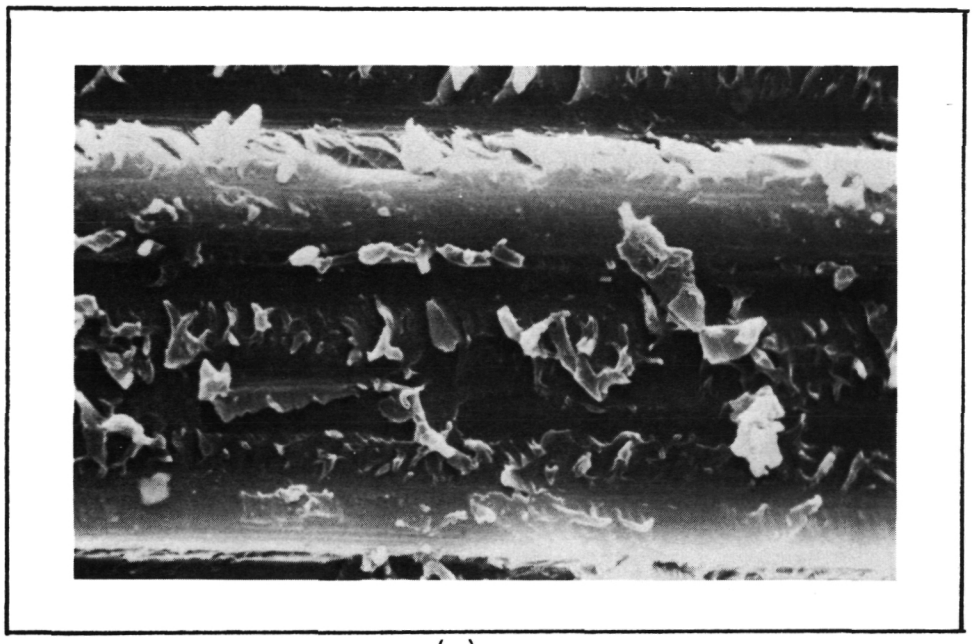

(a)

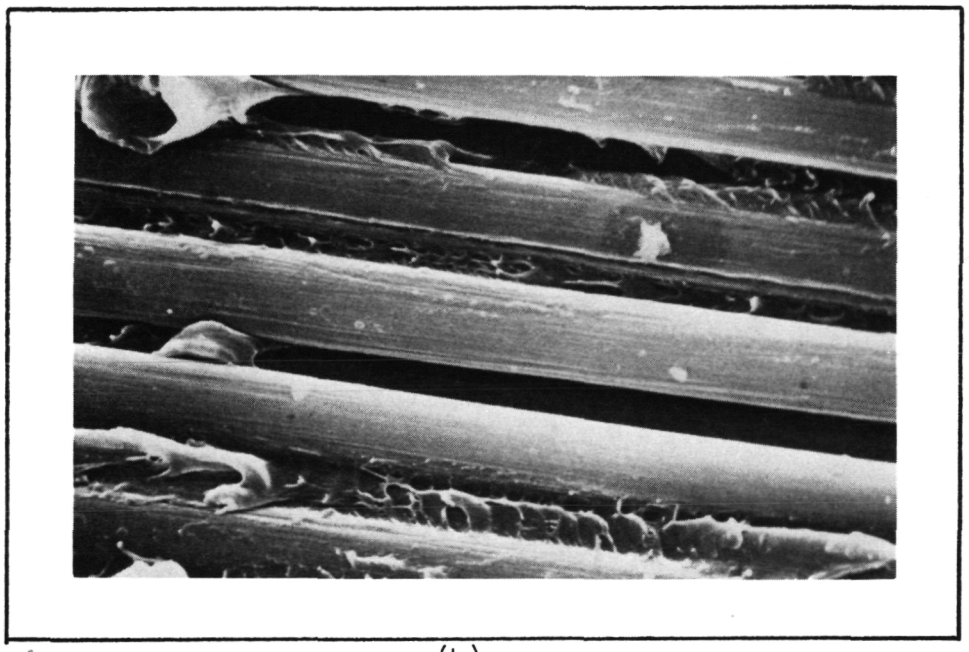

(b)

Figure 12. SEM photographs of fracture surfaces of ten degree off-axis composite tensile specimens. Erose fiber surfaces and shear lips in 12(a) indicate a strong matrix-fiber bond and shear failure respectively, for the 930 composite. The smooth, clean fiber surfaces in 12(b) indicate a very weak P-1700-fiber bond. (a) 5.9Kx. (b) 1.8Kx.

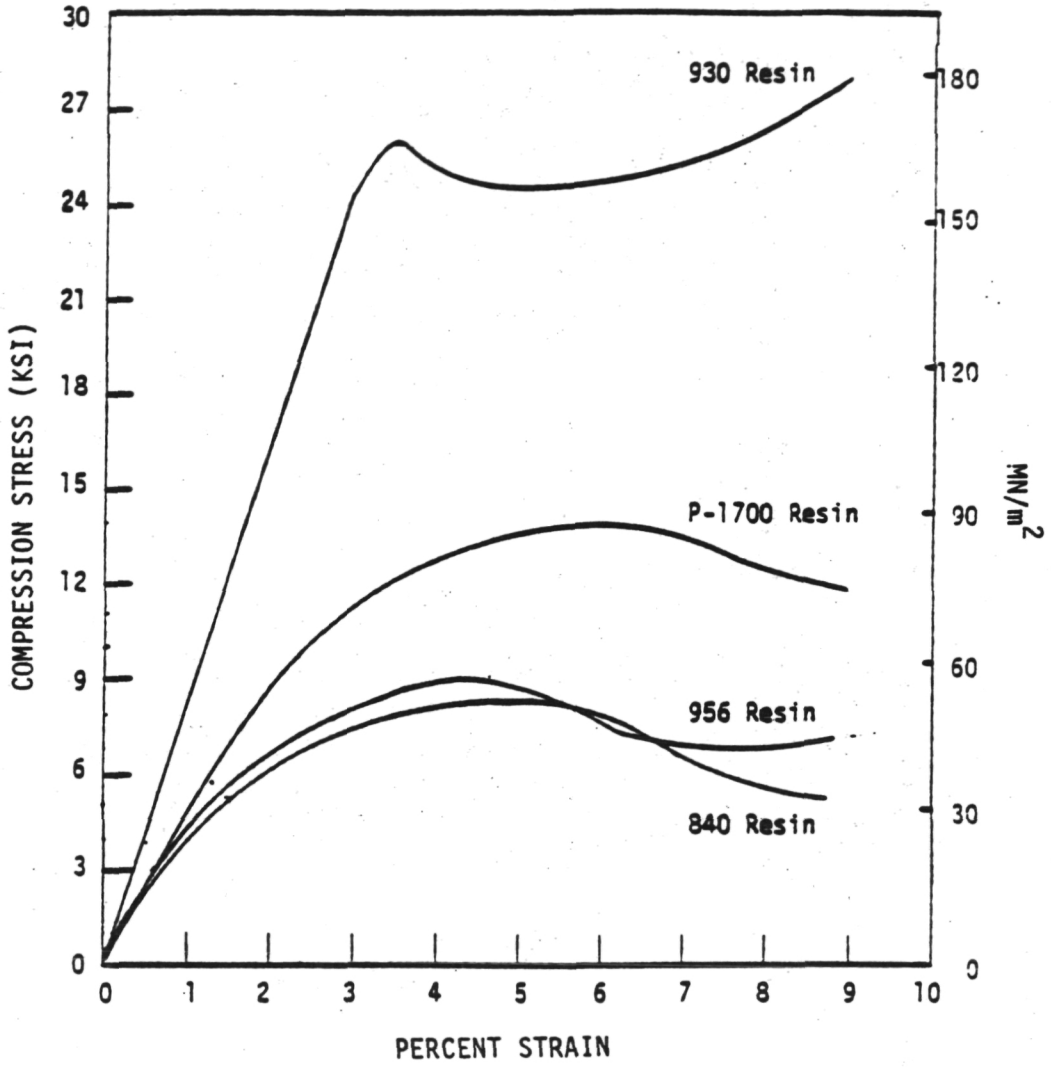

Figure 13. Compression stress - strain curves for the composite matrix polymers used in this study.

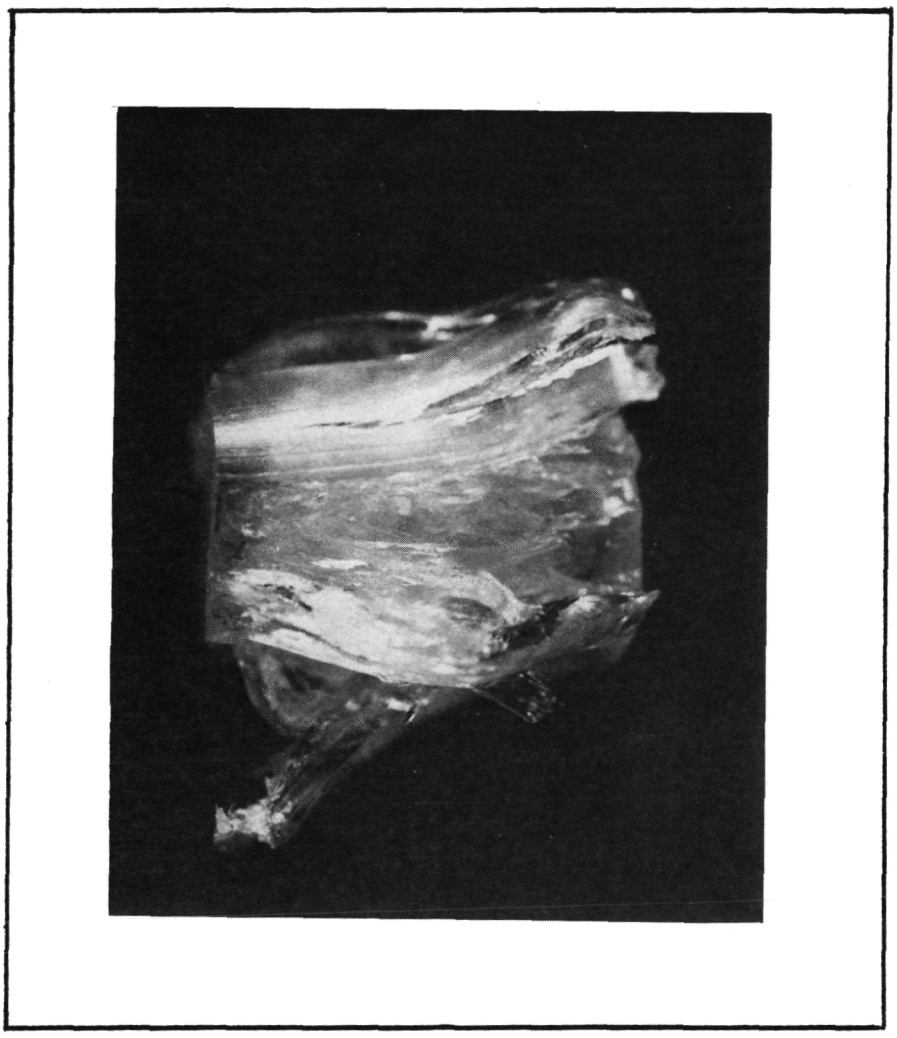

Magnification 2X

Figure 14. Typical epoxy compression failure. Note the longitudinal fiberous strands which are orientated from left to right in the photograph.

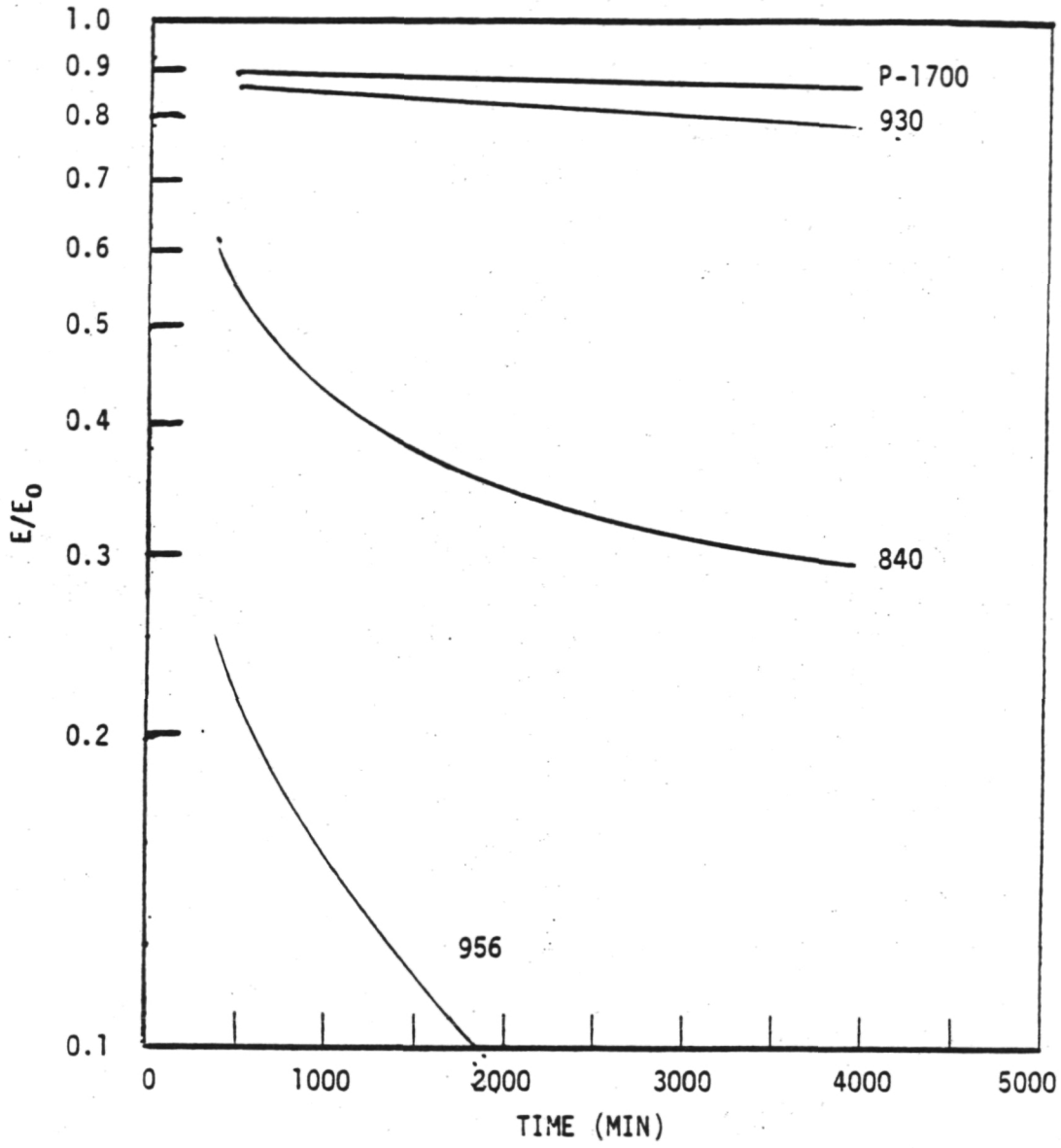

Figure 15. Relaxation curves measured for each of the four resins that were studied. E is the instantaneous tensile modulus and E_o is the initial tensile modulus.

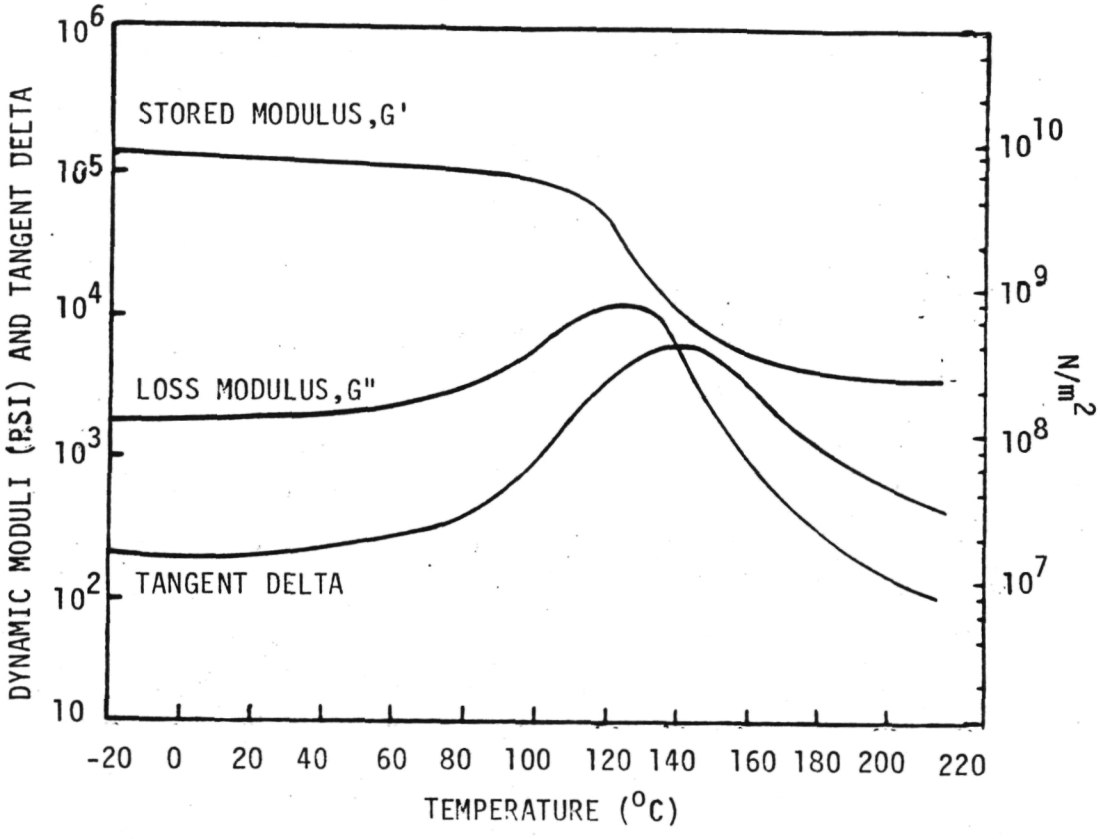

Figure 16. Dynamic moduli and damping factor of the 930 epoxy polymer as functions of temperature. The glass transition temperature is measured at the maximum peak of the loss modulus curve.

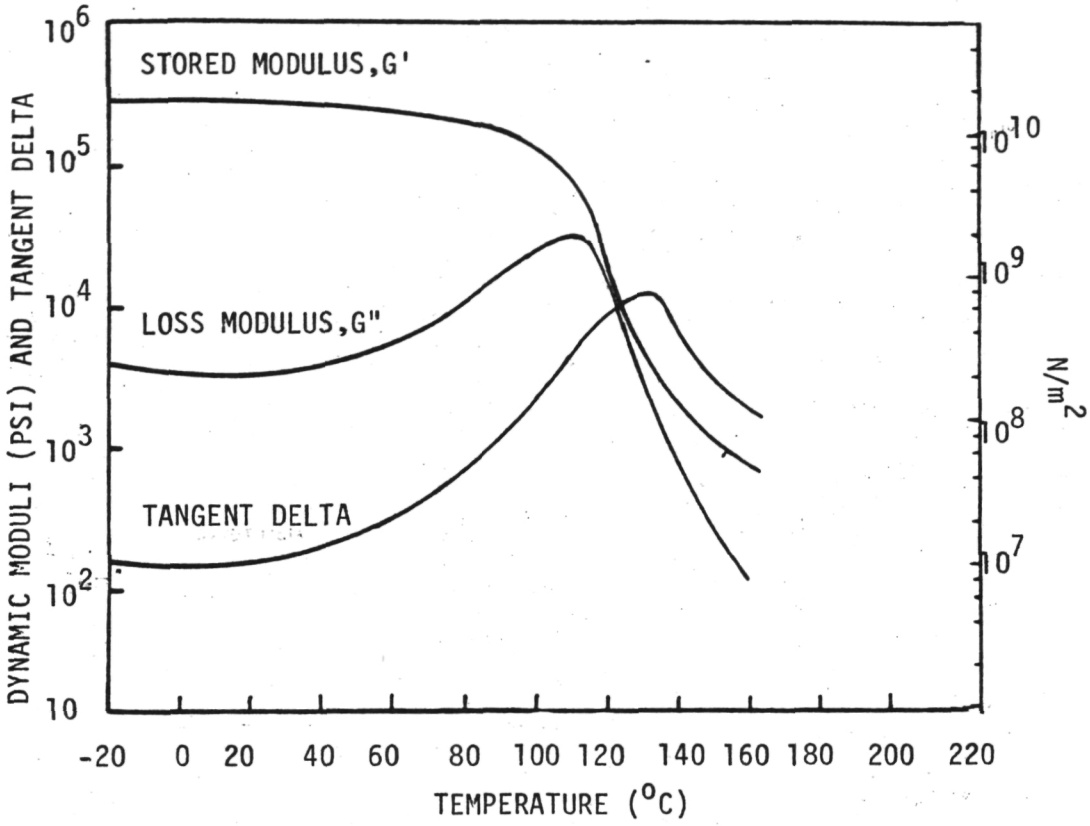

Figure 17. Dynamic moduli and damping factor of the 930 composite as functions of temperature. The glass transition temperature is measured at the maximum peak of the loss modulus curve.

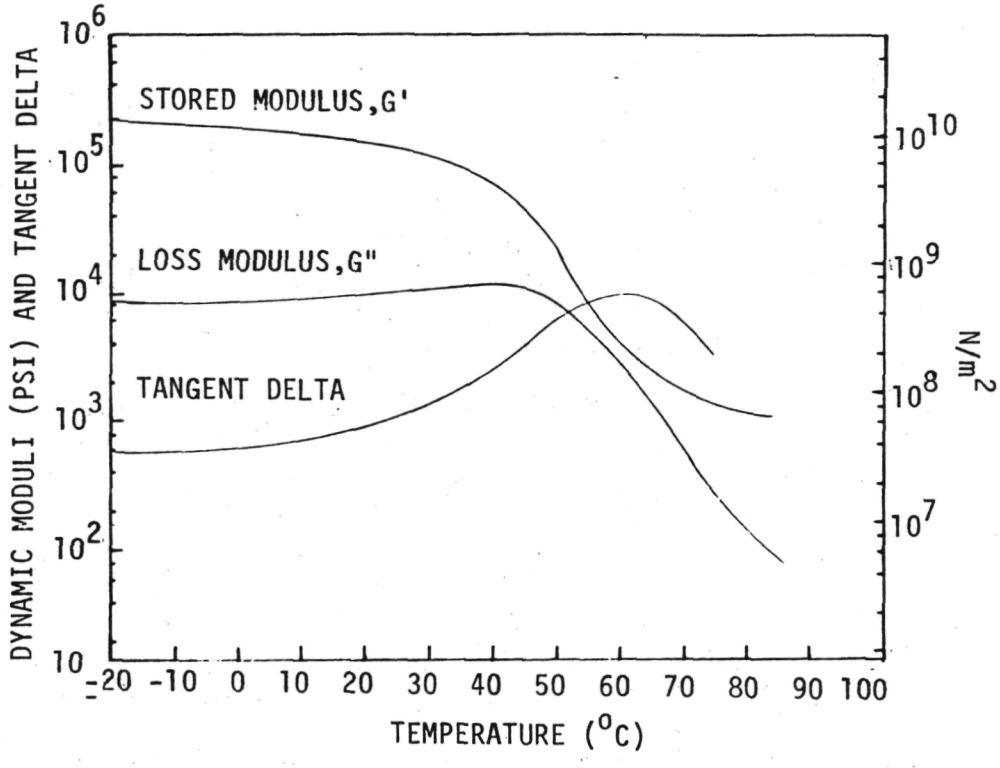

Figure 18. Dynamic moduli and damping factor of the flexibilized 840 polymer as functions of temperature. The glass transition temperature is measured at the maximum peak of the loss modulus curve.

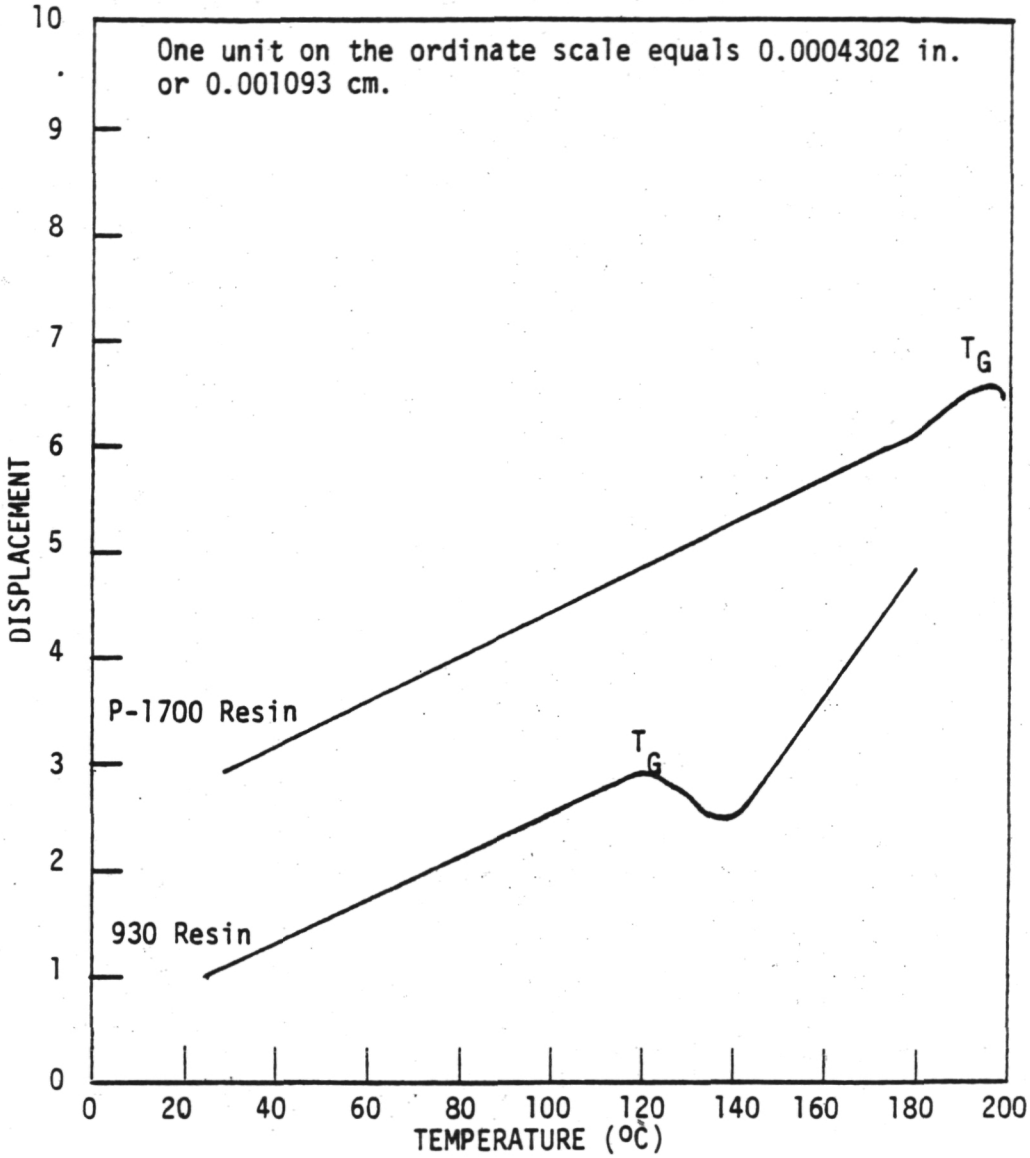

Figure 19. TMA trace of P-1700 and 930 resins showing the variation in linear expansion of the resins with temperature. T_g is measured at the first significant change in slope of each curve.

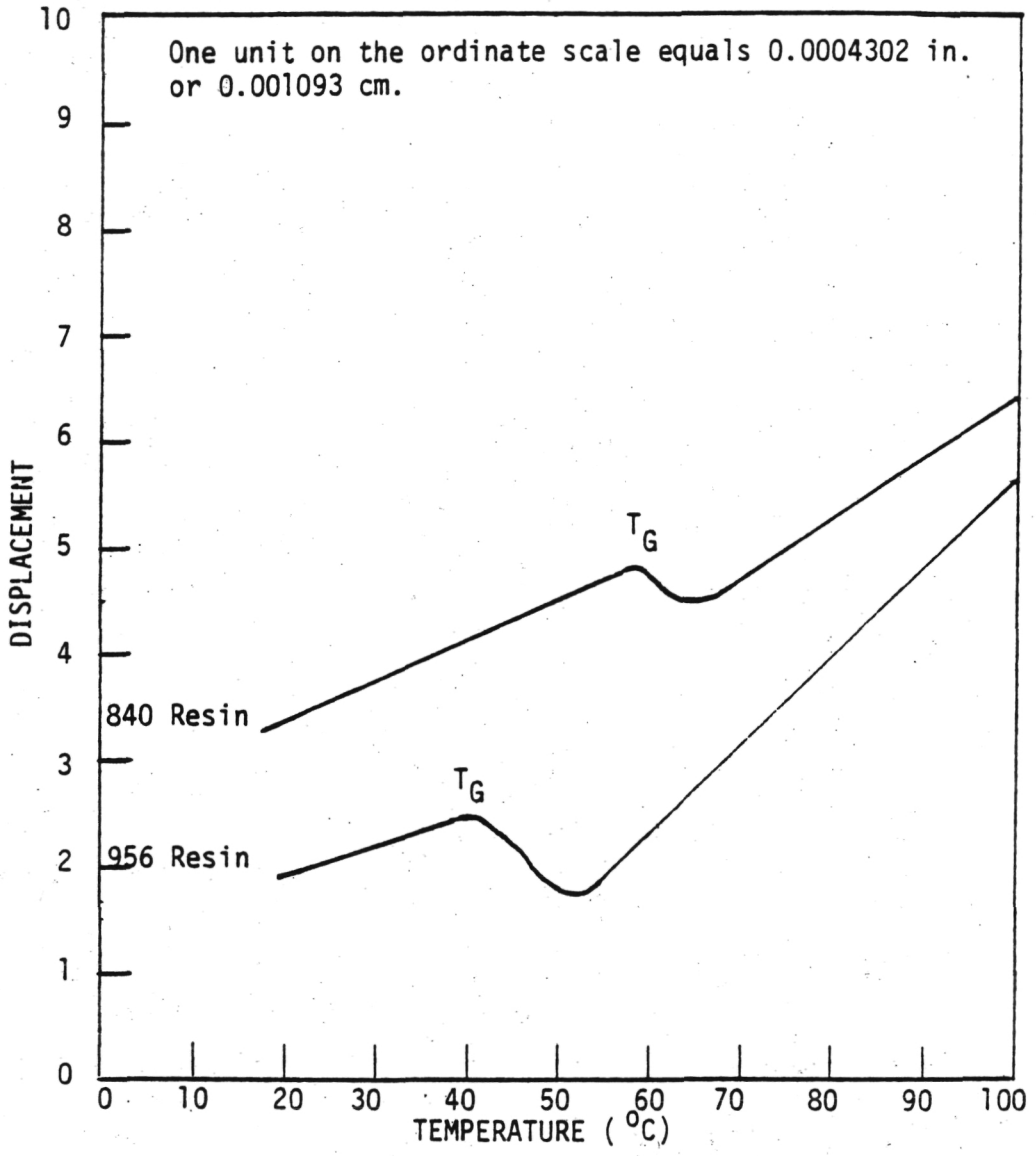

Figure 20. TMA traces of 840 and 956 resins showing the variation in linear expansion of the resins with temperature. T_g is measured at the first significant change in slope of each of the curves.

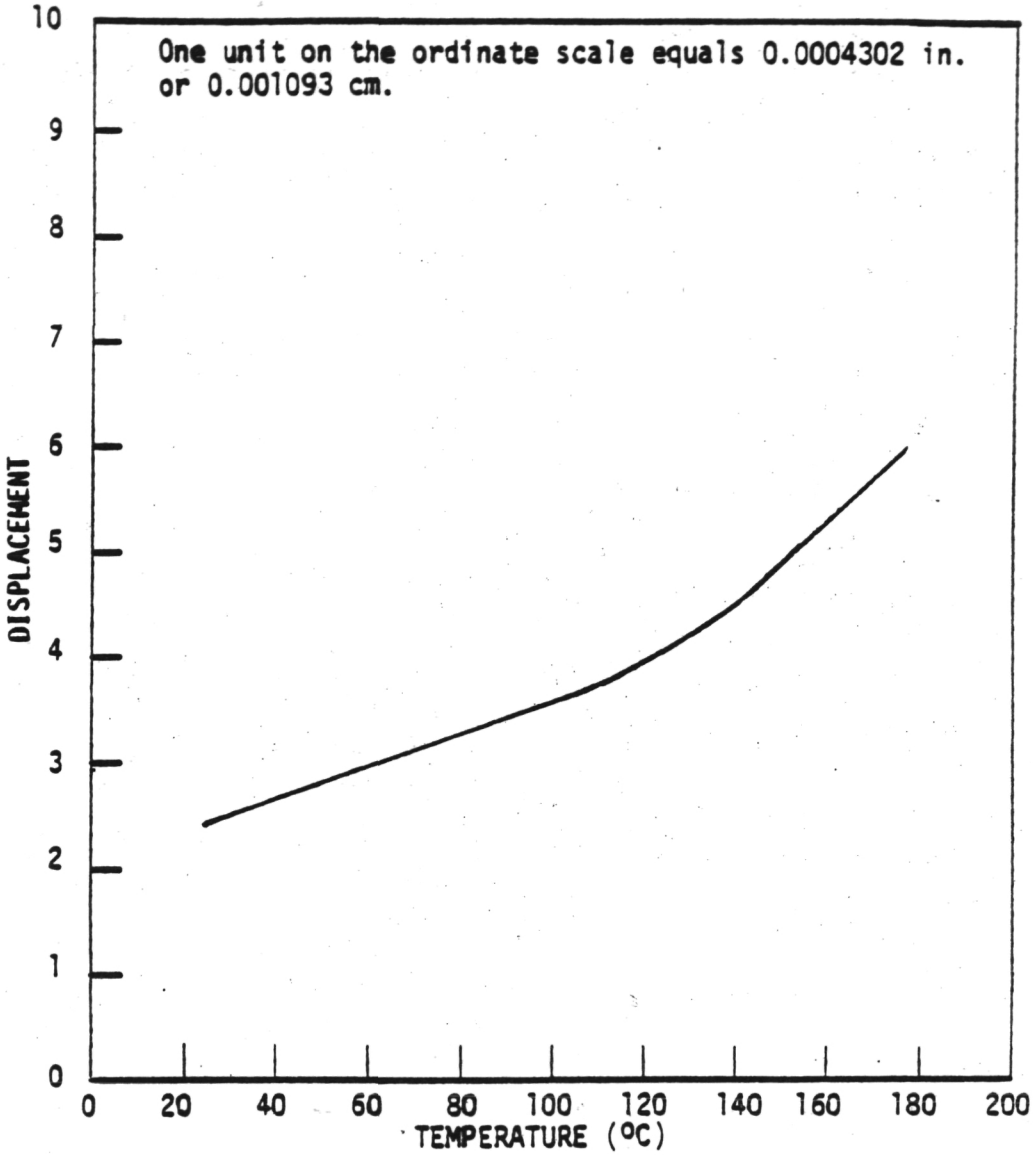

Figure 21. Typical TMA trace of a polymer matrix composite. Note the gradual change in slope which obscures the T_g point.

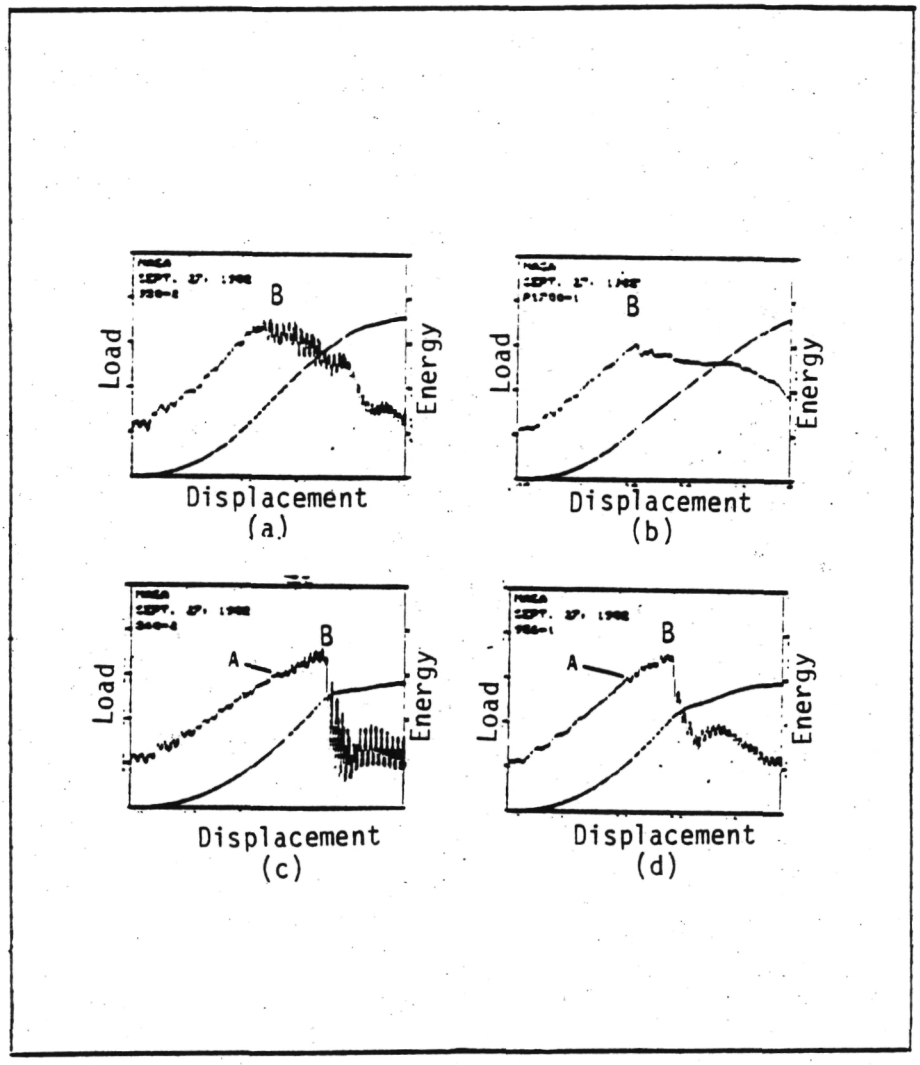

Figure 22. Load-deflection and energy-deflection traces for matrix resin plates. Lower curve is the energy curve. The resins tested are as follows: (a) 930. (b) P-1700. (c) 840. (d) 956. Load scale is the left ordinate.

C-3

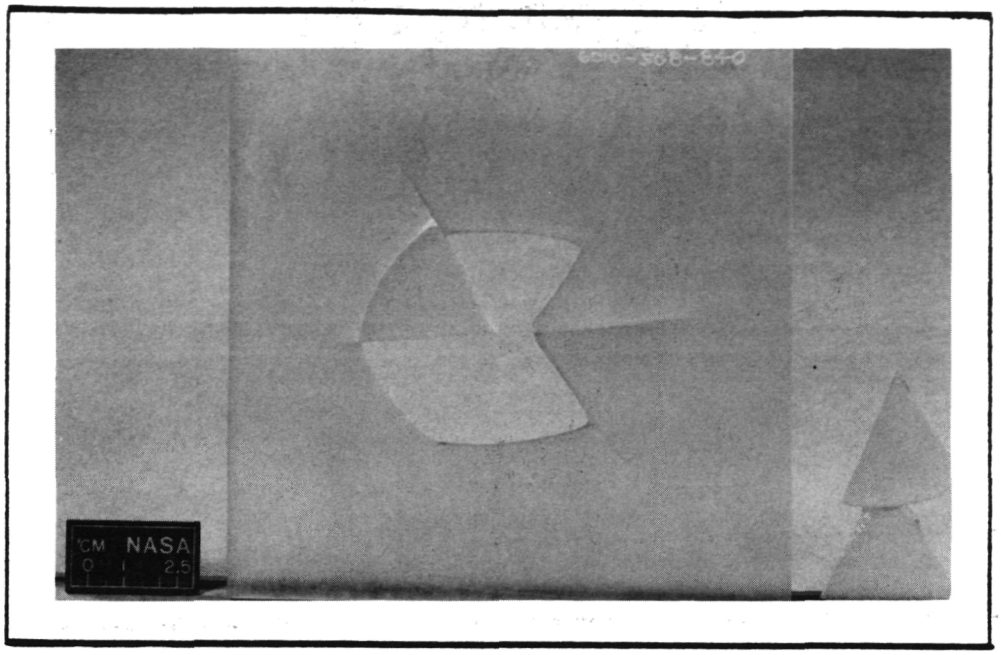

(a)

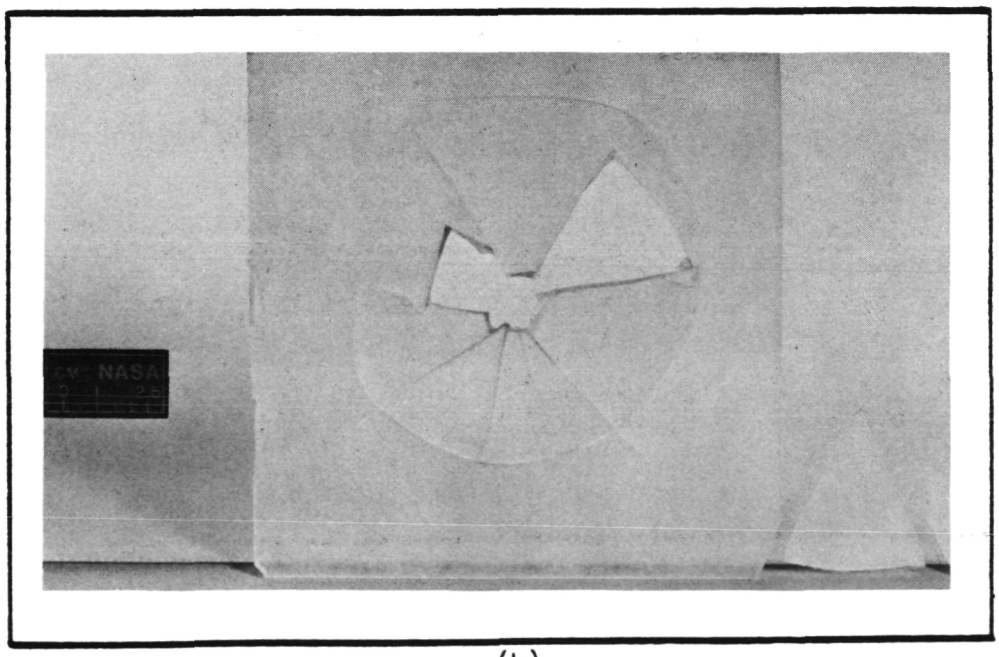

(b)

Figure 23. Impacted plates of matrix resins. Impacting occurred at a velocity of 8 ft/sec (244 cm/sec) with a 0.5 inch (1.27 cm) diameter spherical tipped penetrator. (a) 840 resin. (b) 956 resin.

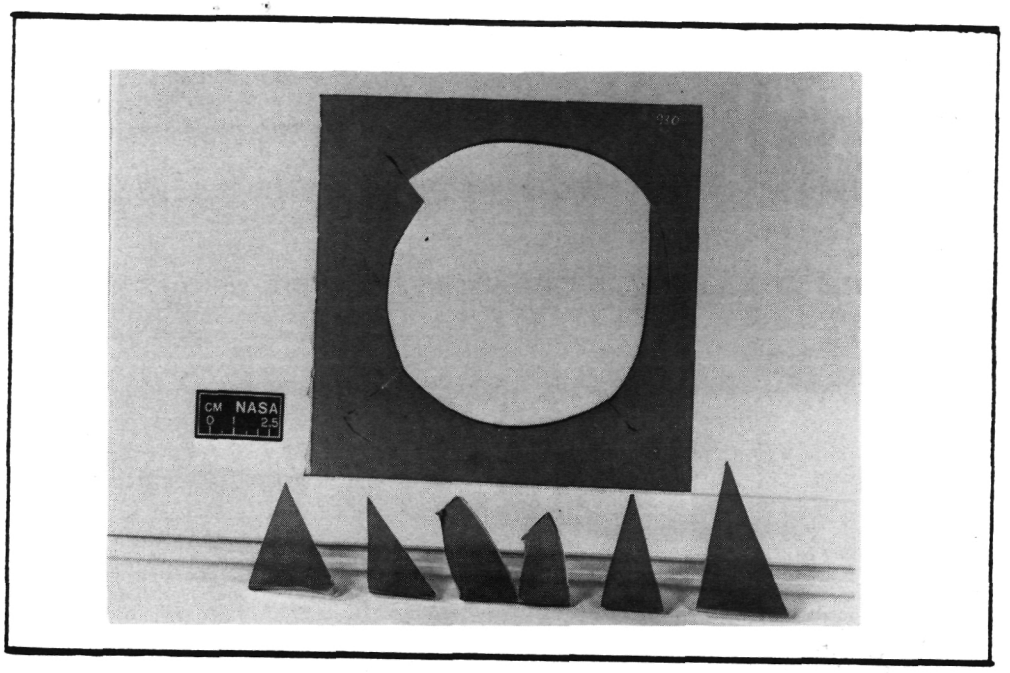

(a)

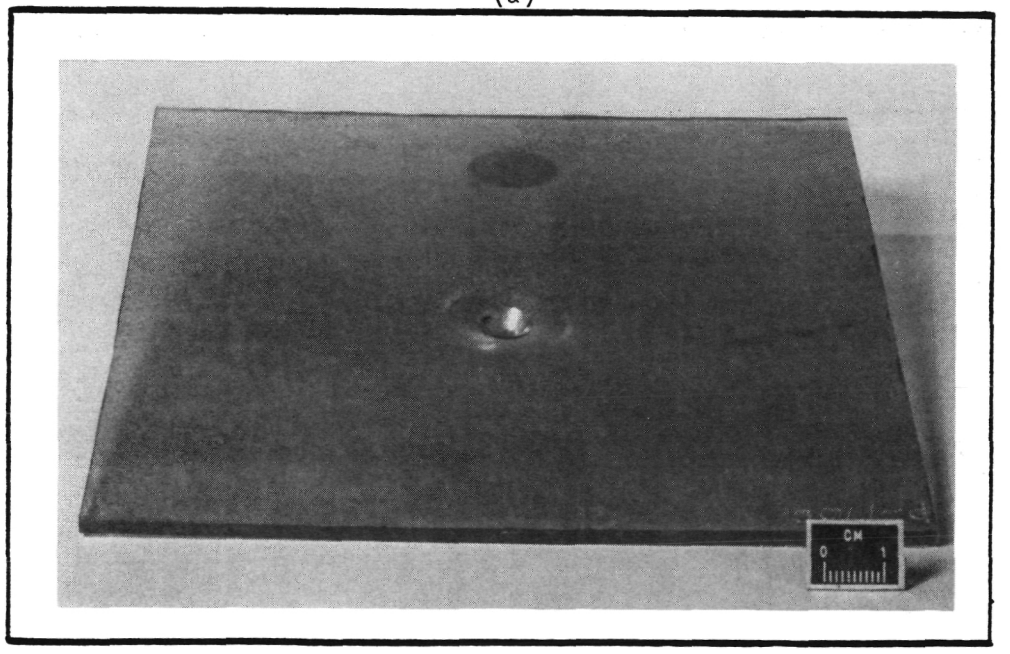

(b)

Figure 24. Impacted plates of matrix resins. Impacting occurred at a velocity of 8 ft/sec (244 cm/sec) with a 0.5 inch (1.27 cm) diameter spherical tipped impactor. (a) 930 resin. (b) P-1700 resin.

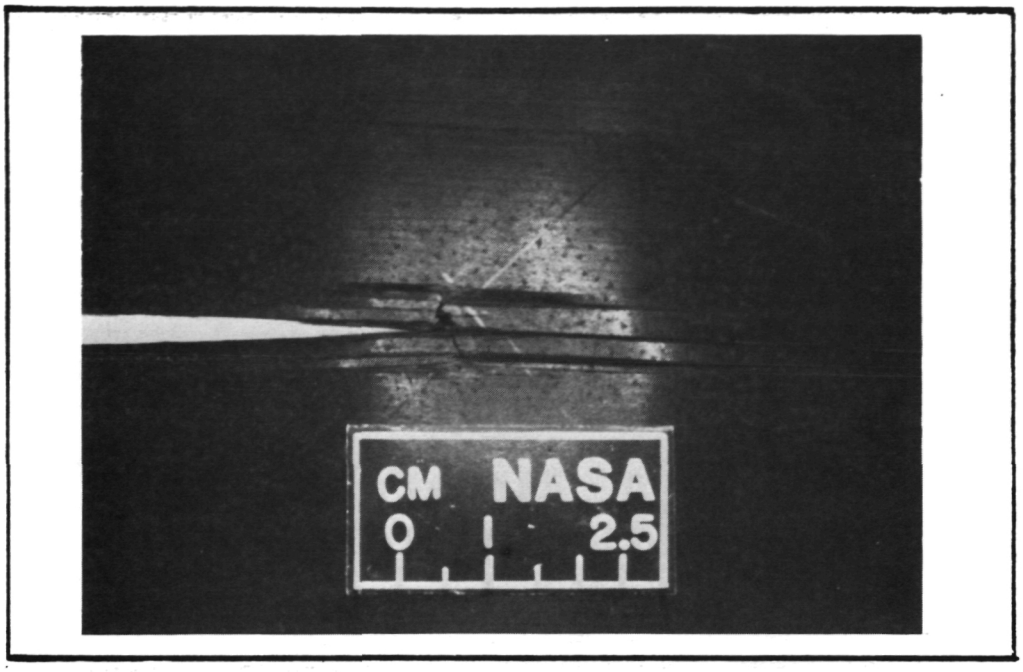

(a)

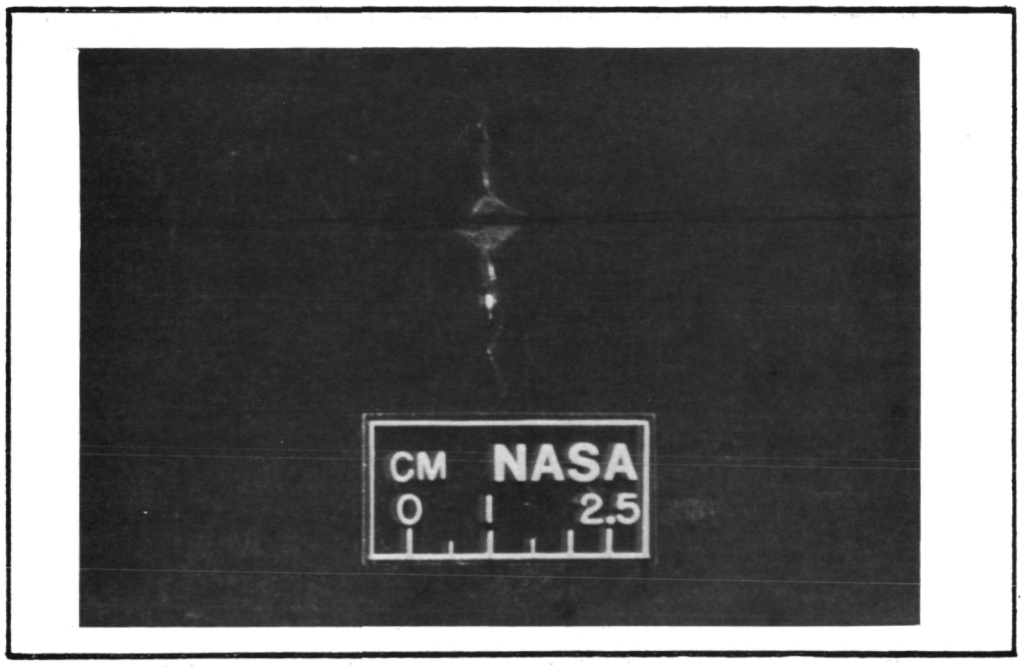

(b)

Figure 25. Unidirectional composite impact failure modes. Composites were impacted at a velocity of 8ft/sec (244cm/sec) with a 0.5 inch diameter spherical tipped impactor. (a) punch-out type of failure. (b) splitting and wedging type of failure.

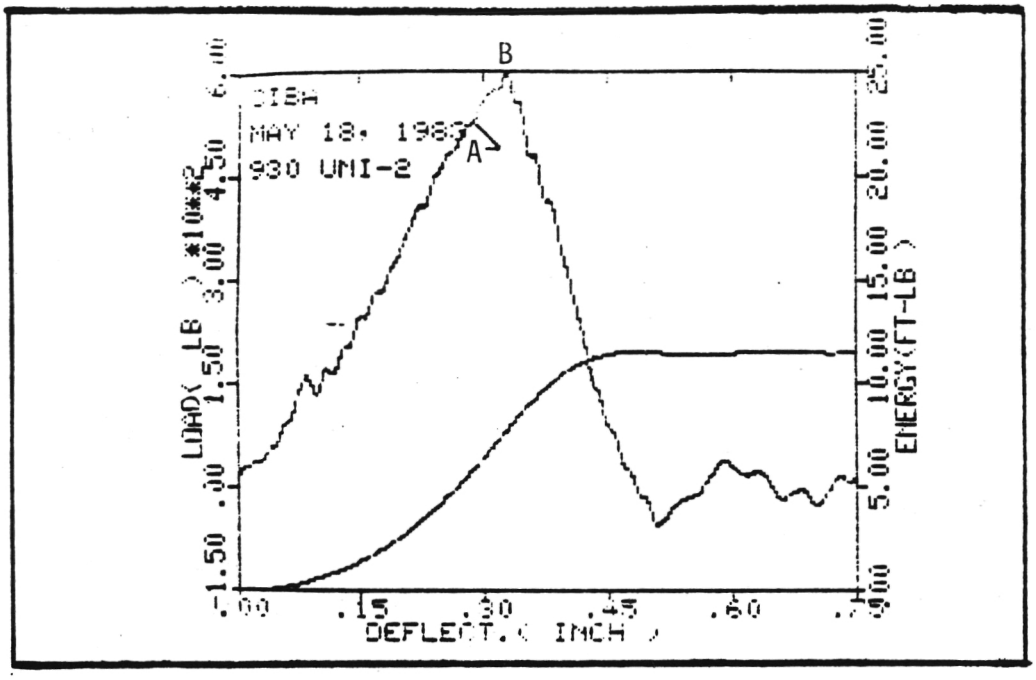

(a)

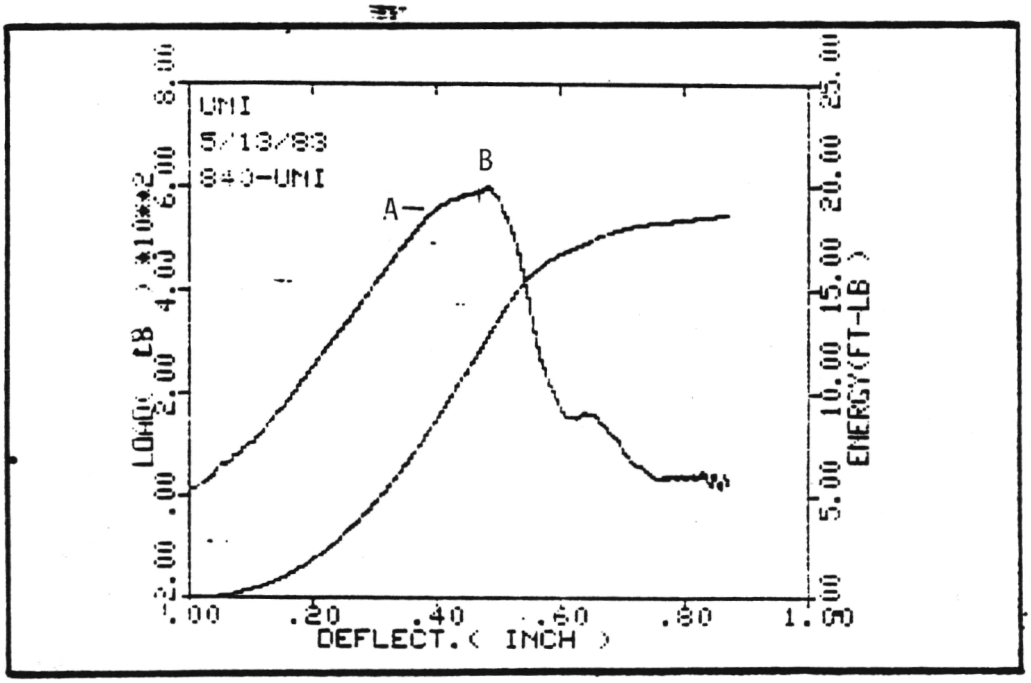

(b)

Figure 26. Load deflection and energy deflection curves for unidirectional composites. Lower curve is energy curve. (a) punch-out failure mode. (b) splitting and wedging failure mode.

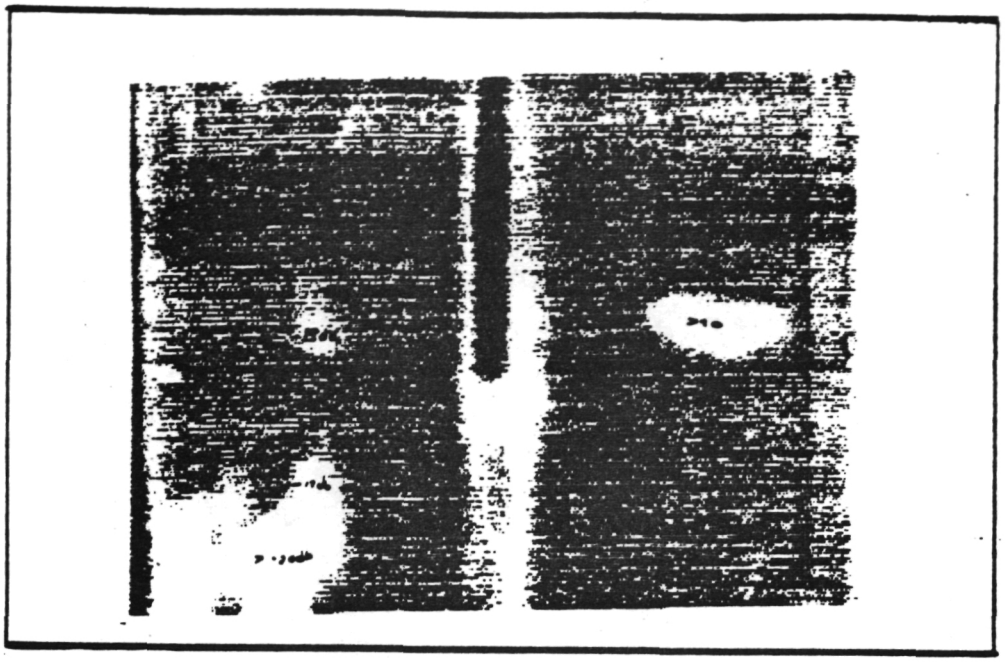

(a)

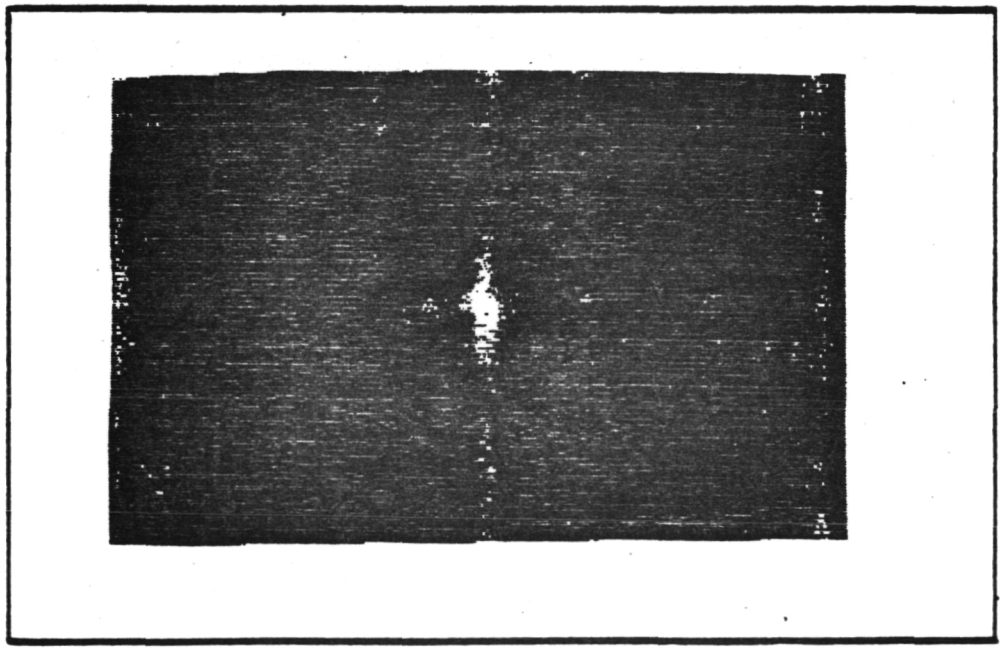

(b)

Figure 27. Typical ultrasonic c-scans of impacted unidirectional composites. Undamaged material is indicated by dark traces. (a) Punch-out damage mode. (b) Splitting and wedging damage mode.

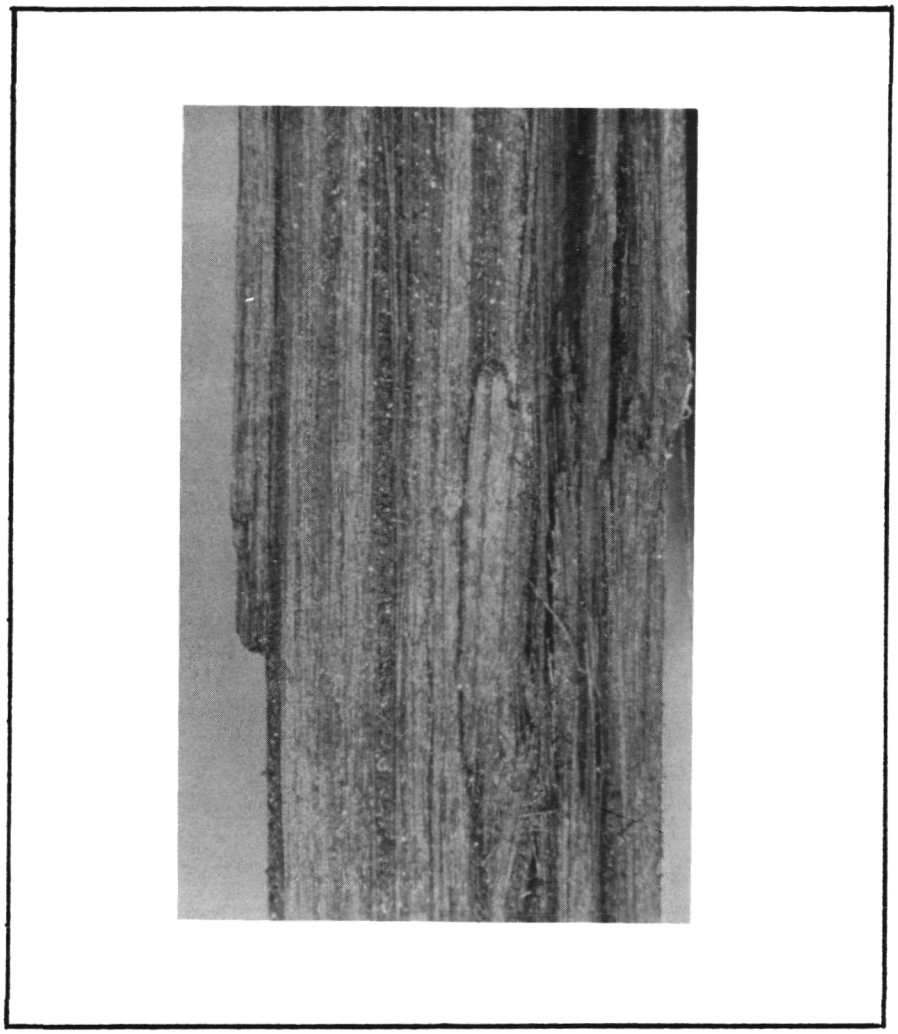

Magnification 15X

Figure 28. Damage incurred by unidirectional composite after being impacted at a velocity of 8 ft/sec (244 cm/sec) with a 0.5 inch (1.27 cm) diameter spherical tipped impactor.

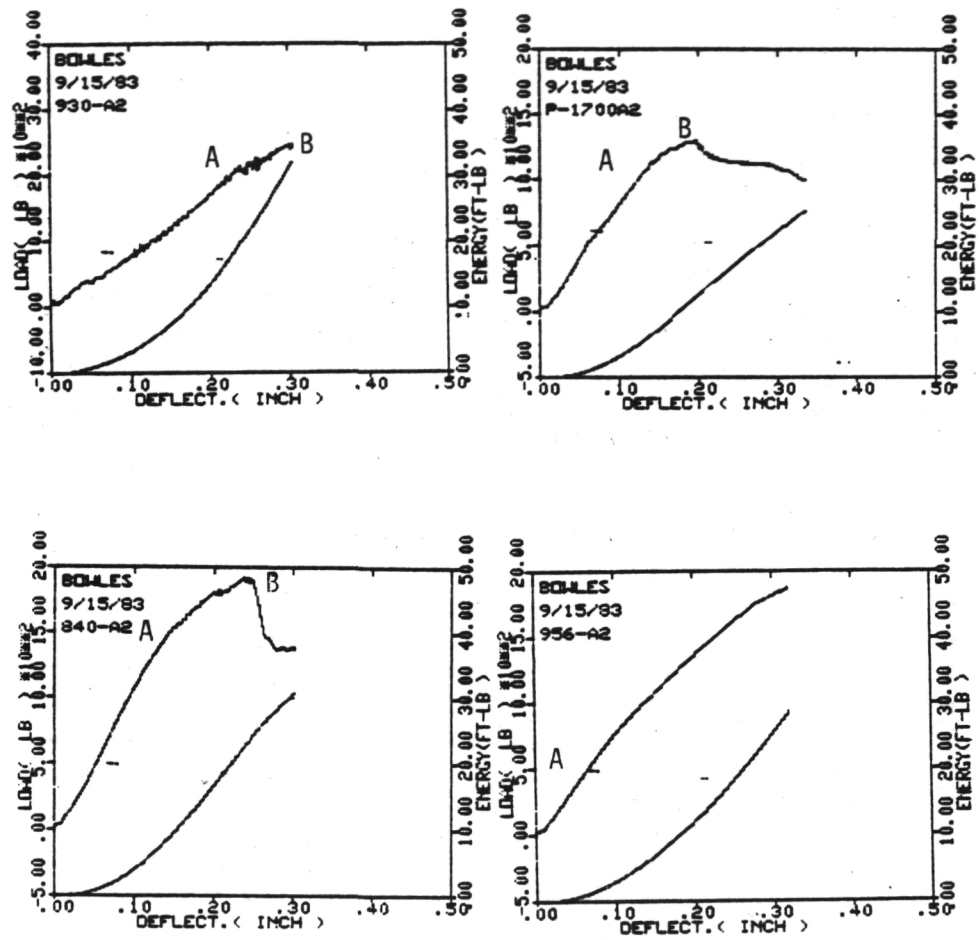

Figure 29. Load-deflection and energy-deflection curves for the 30 ply crossplied composites. The lower curve is the energy curve. The composites represented by the curves are: (a) 930. (b) P-1700. (c) 840. (d) 956.

(a)

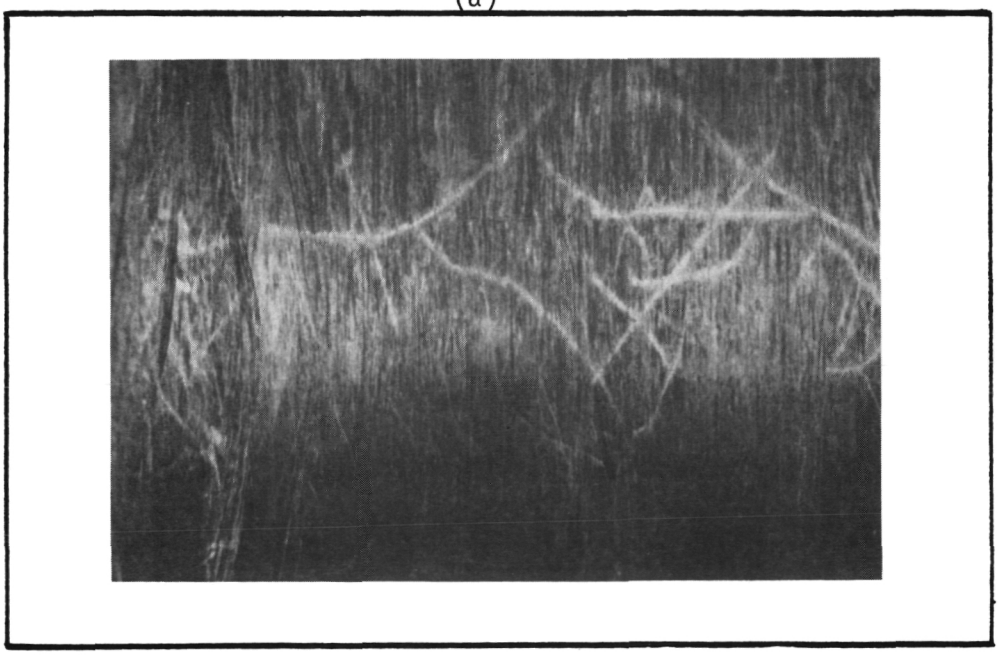

(b)

Figure 30. Thick, crossplied 930 composite subjected to an impact energy of 31 ft-lb (42J). Impact velocity was 8 ft/sec (244 cm/sec). Spherical tipped impactor measured 0.5 inch (1.27 cm) in diameter. Magnification 2X. (a) Impacted surface. (b) Backside surface.

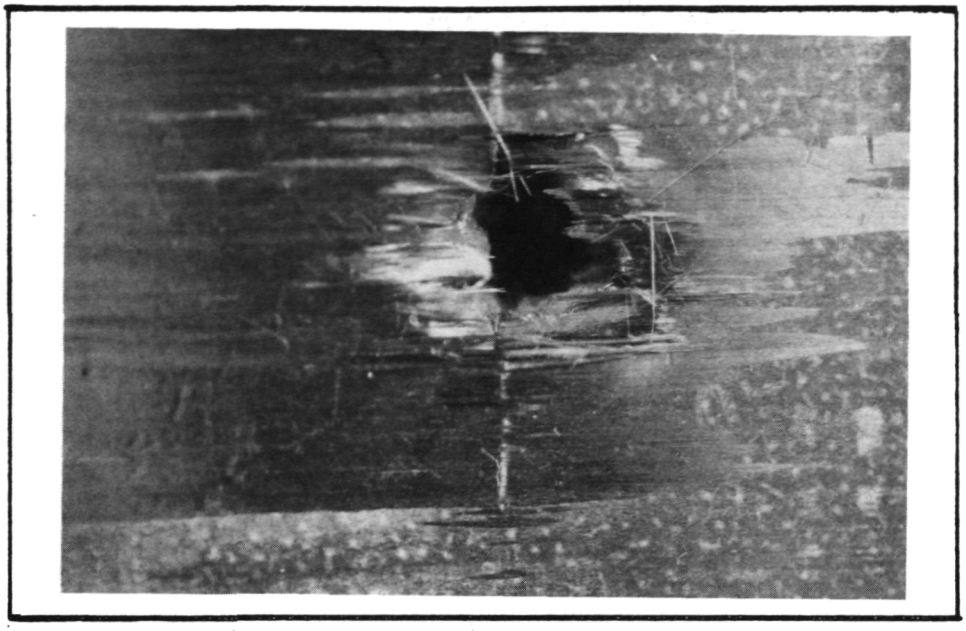

(a)

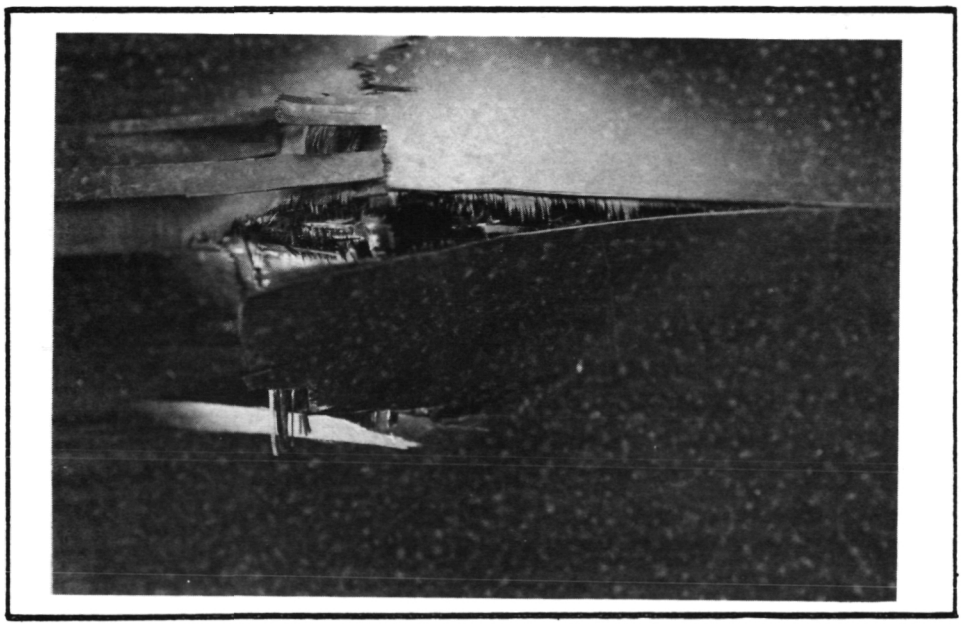

(b)

Figure 31. Thick crossplied P-1700/composite subjected to through penetration impact. Impact velocity was 8 FT/SEC (244 CM/SEC). Spherical tipped impactor measured 0.5 inch in diameter. (a) impacted surface. (b) backside surface.

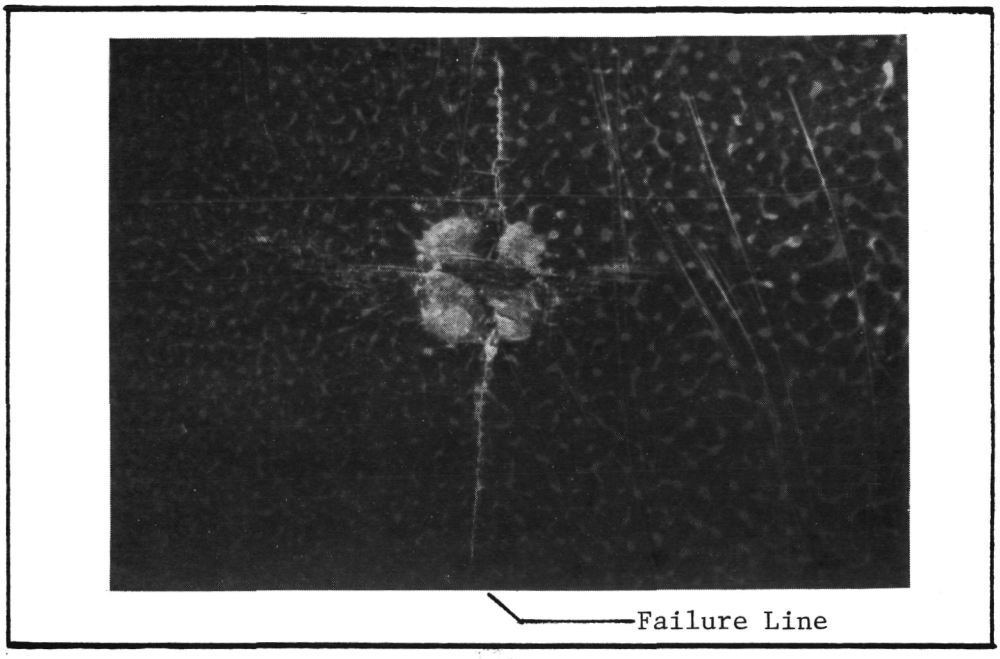

(a)

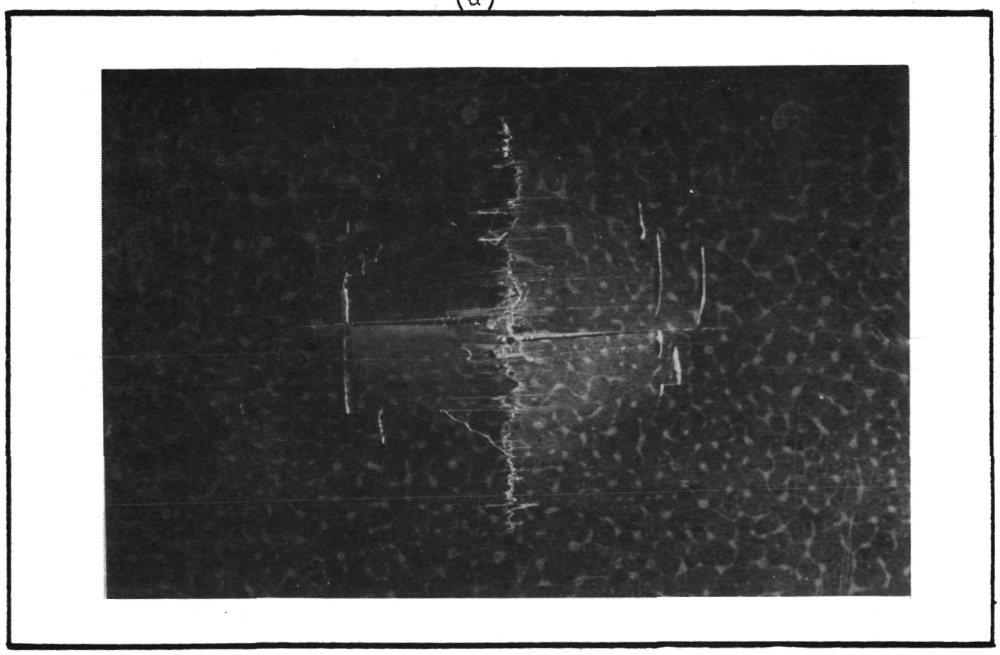

(b)

Figure 32. Thick crossplied 840 composite subject to through penetration impact. Impact velocity was 8 ft/sec (244 cm/sec). Spherical tipped impactor measure 0.5 inch (1.27 cm) in diameter. Magnification 2X. (a) Impacted surface. (b) Backside surface.

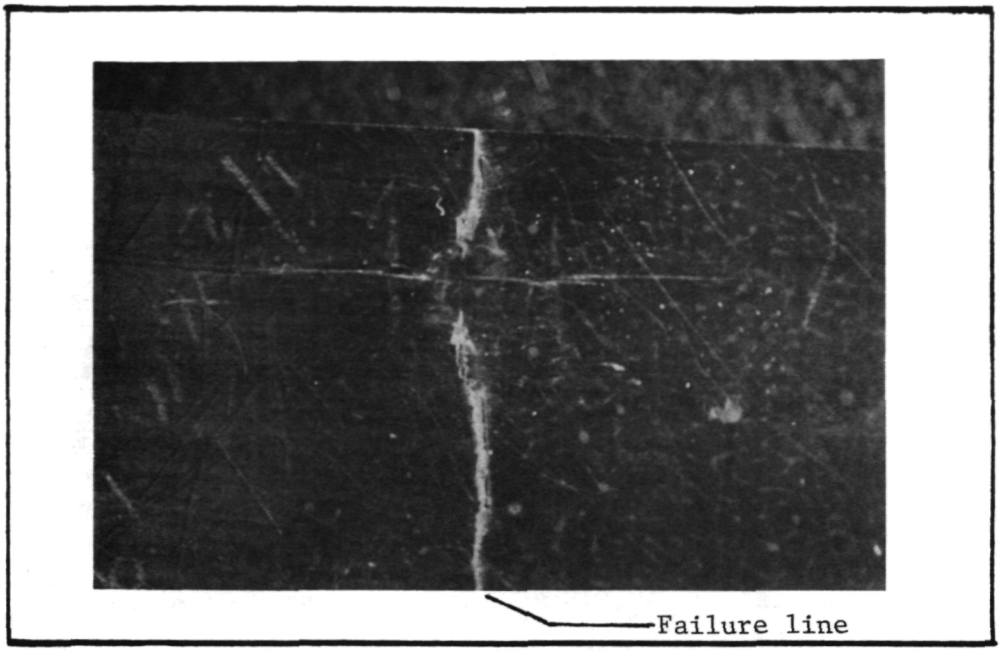

(a)

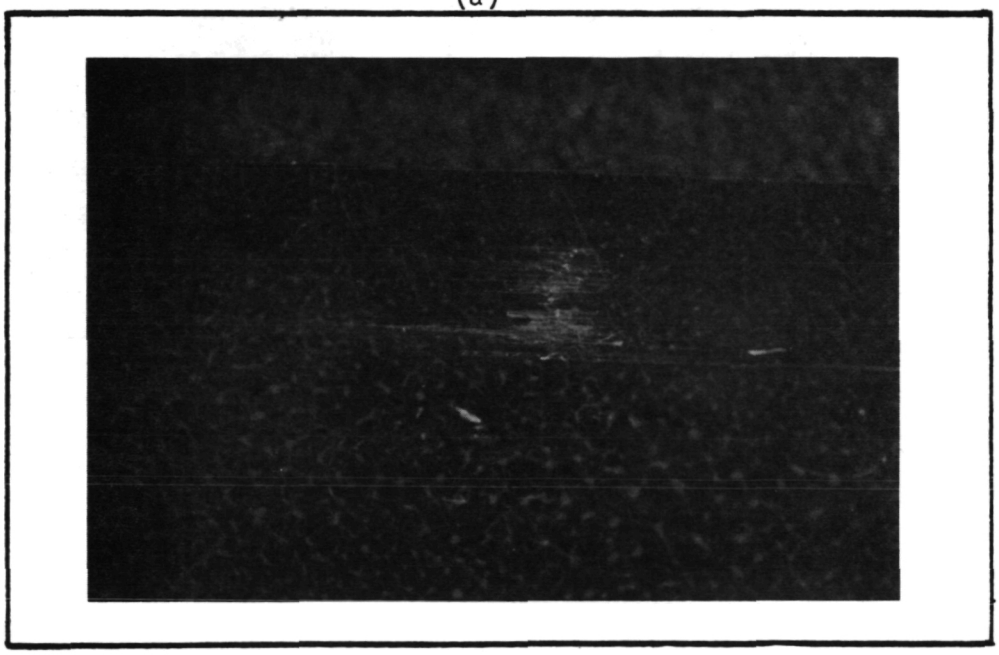

(b)

Figure 33. Thick crossplied 956 composite subject to through penetration impact. Impact velocity was 8 ft/sec (244 cm/sec). Spherical tipped impactor measure 0.5 inch (1.27 cm) in diameter. Magnification 2X. (a) Impacted surface. (b) Back-side surface.

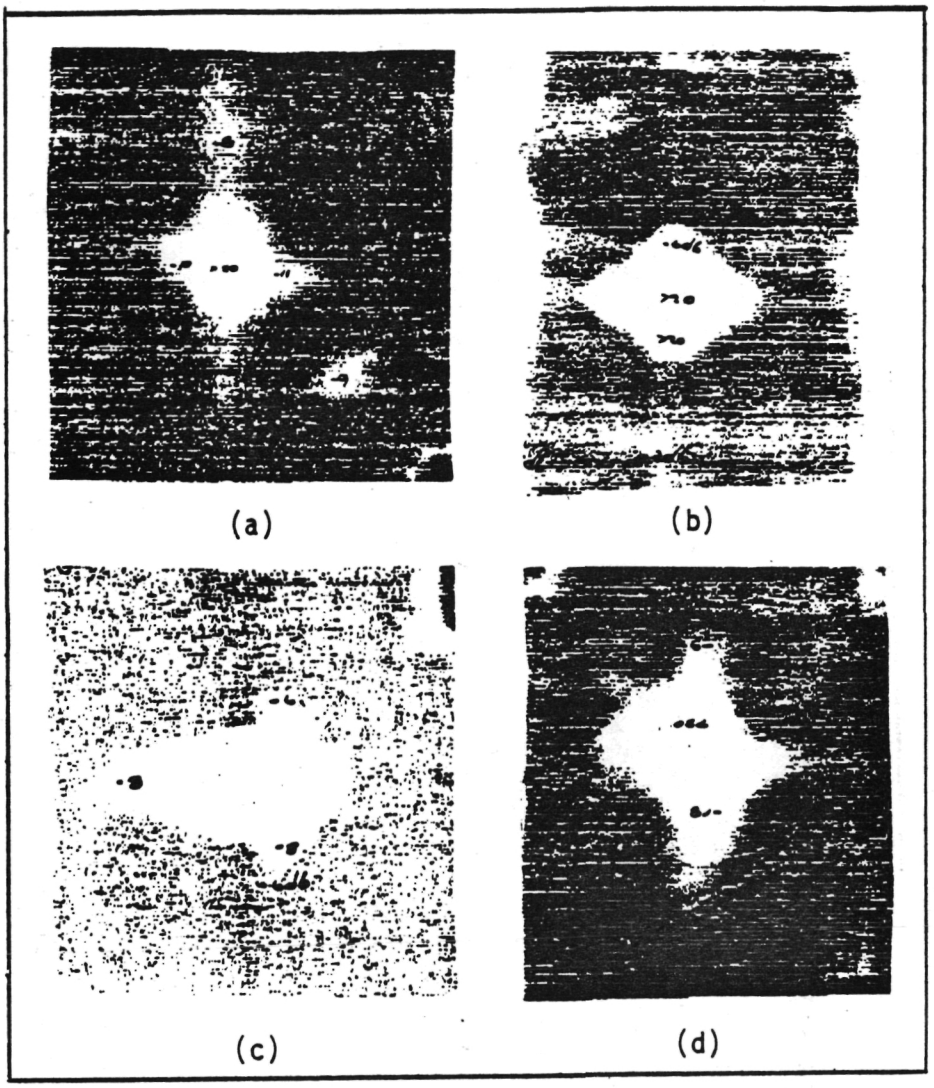

Figure 34. Ultrasonic c-scan traces of the thicker crossplied composites after being impacted. The internal damage varies in magnitude. Dark areas denote sound material. (a) 930. (b) P-1700. (c) 840. (d) 956.

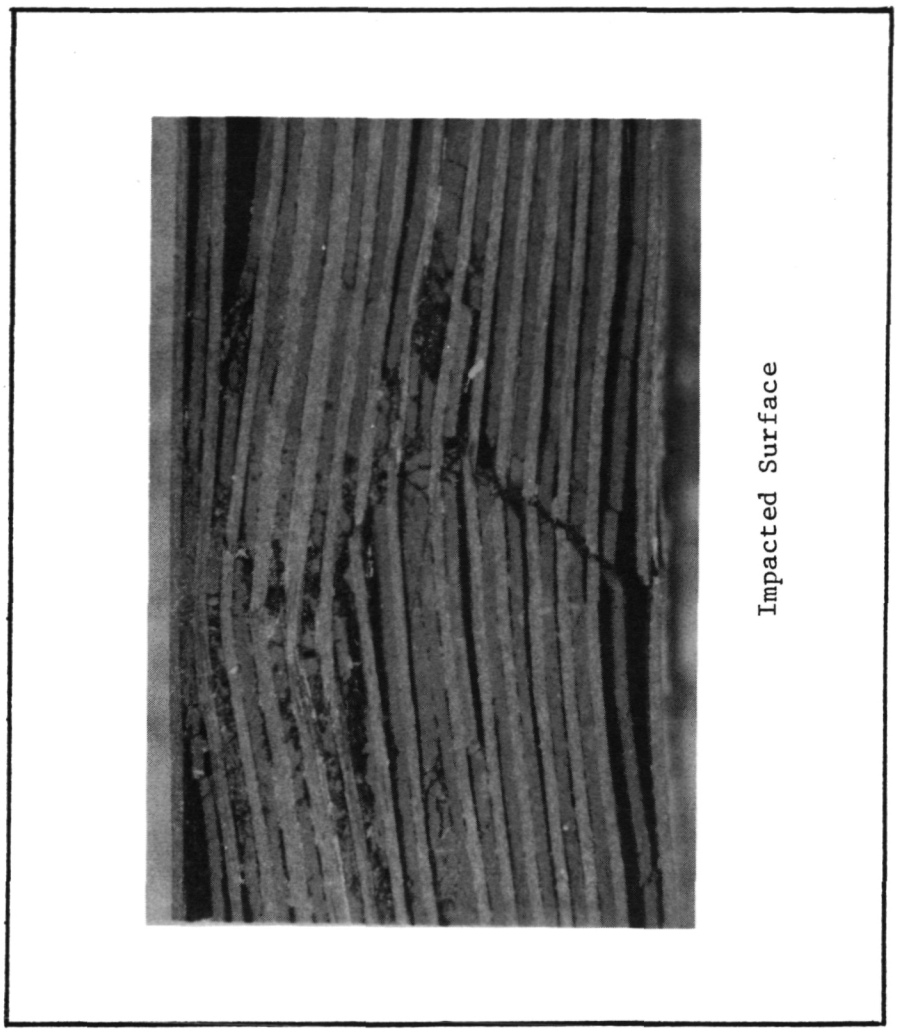

Magnification 13X

Figure 35. Damage incurred by 0.175 inch (0.44 cm) thick 930 crossplied composite after impact. The damaged area is directly under the impact point. Note the fracture through the fibers extends almost through the entire thickness of the specimen.

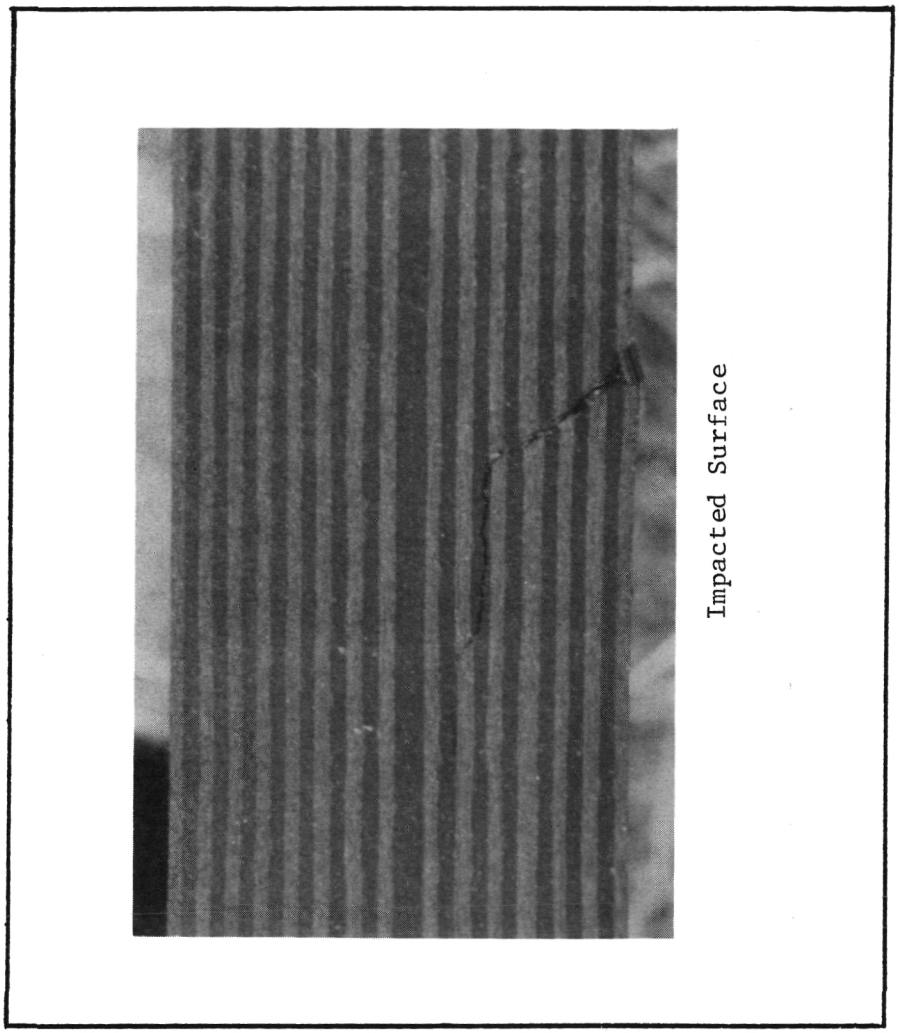

Magnification 13 X

Figure 36. Damage incurred by 0.202 inch (0.51 cm) thick 840 composite after being impacted. Note the delamination at the end of the transfiber crack.

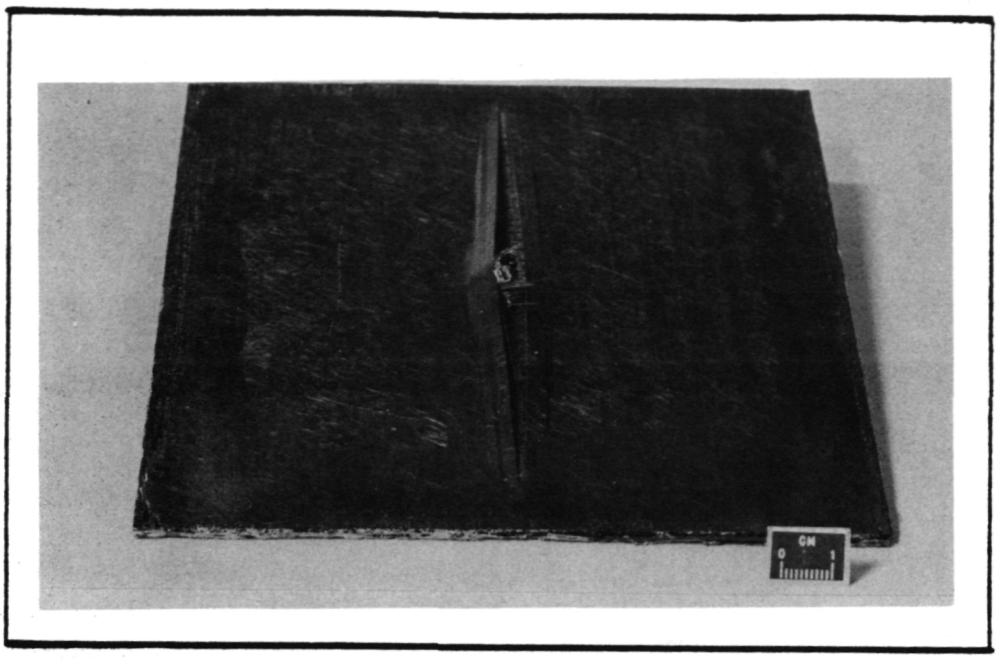

(a)

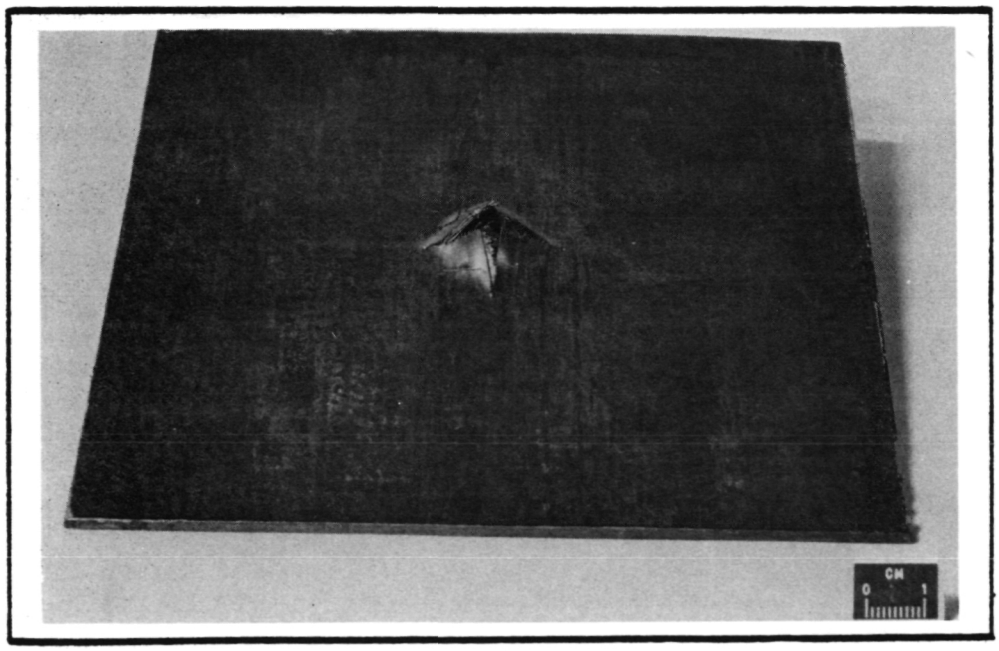

(b)

Figure 37. Impact damage of fifteen ply 930 and P-1700 composites caused by full penetration impact. Note the surface is the back side of the plate. (a) 930. (b) P-1700.

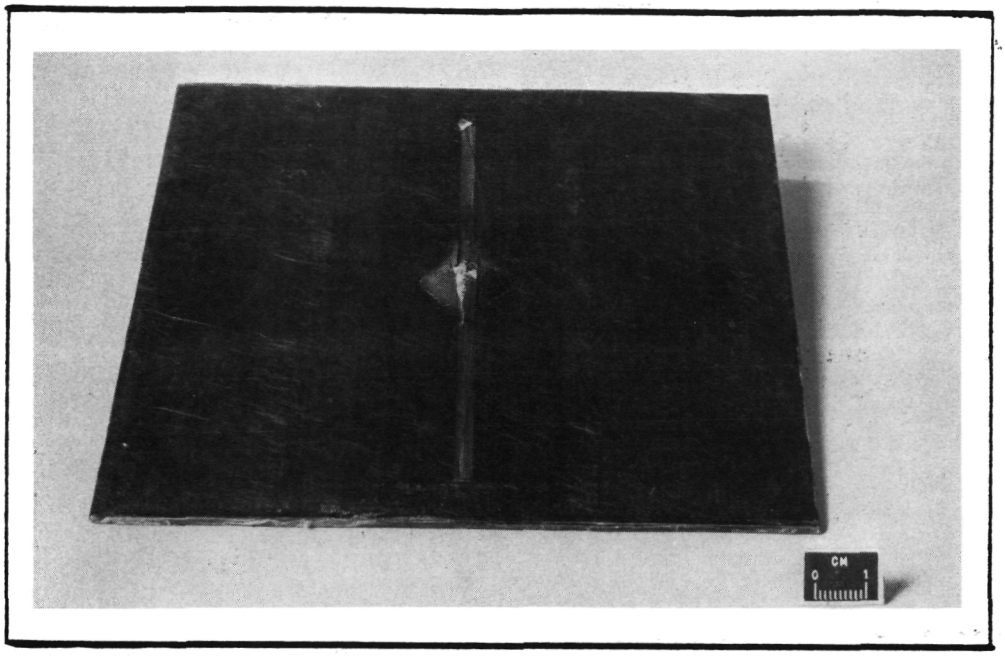

(a)

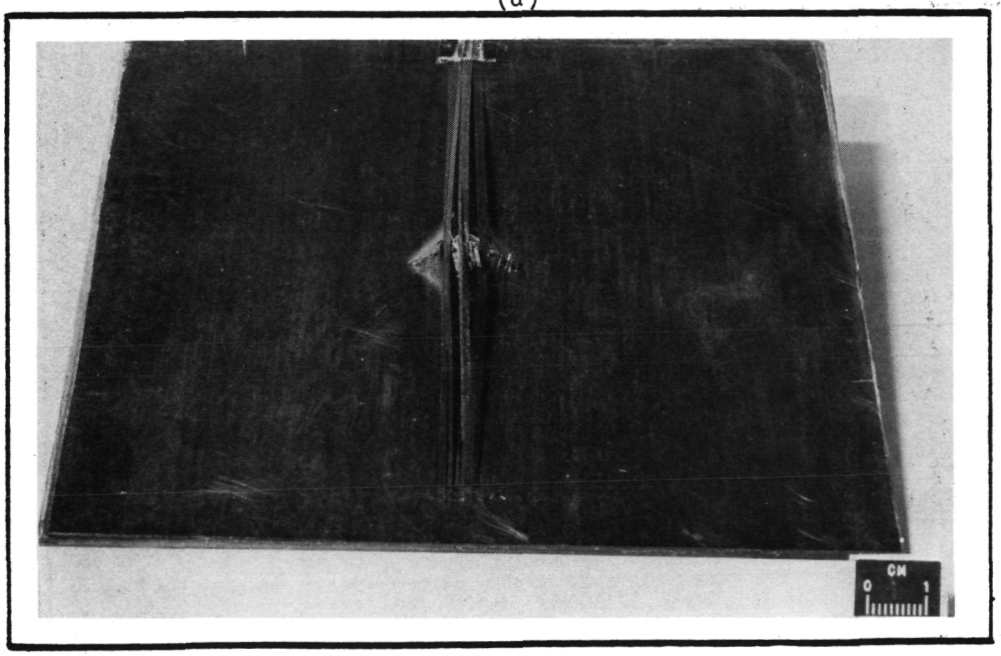

(b)

Figure 38. Impact damage of fifteen ply 840 and 956 composites after full penetration impact. Note the surface is the back side of the plate. (a) 840. (b) 956.

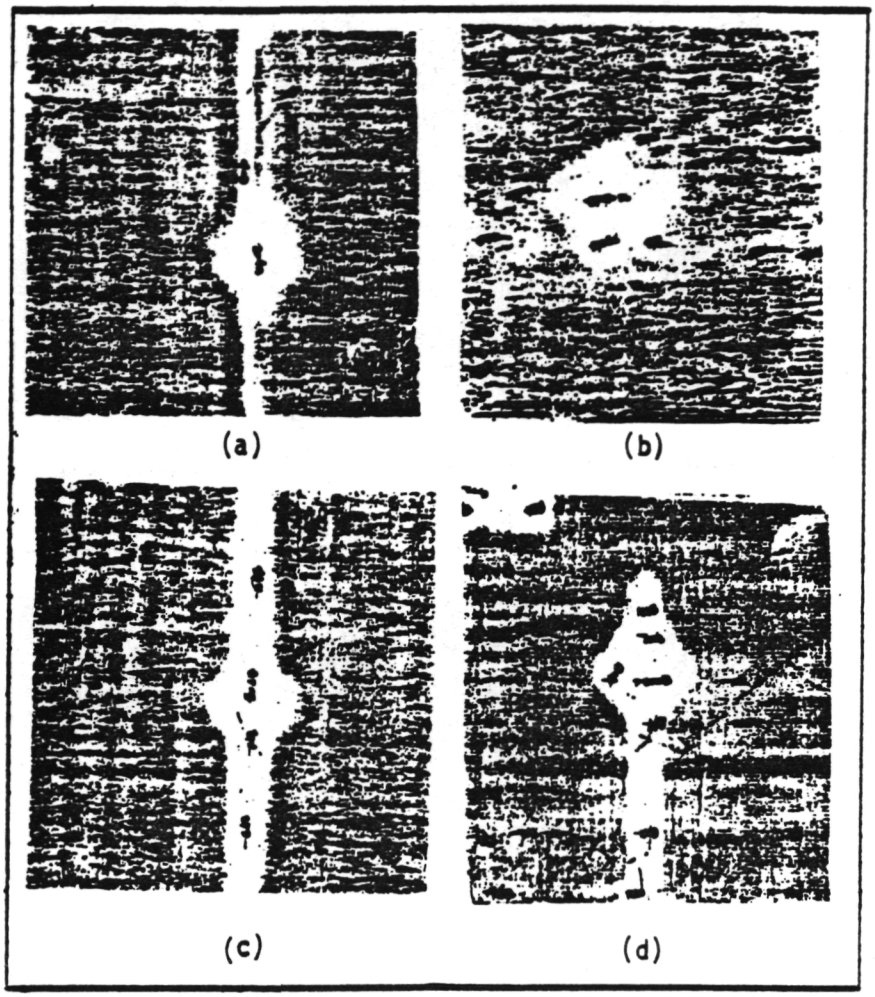

Figure 39. Ultrasonic c-scan traces of fifteen ply impacted composites. There is not any significant variation in the extent of damage among the different composites. Dark areas denote undamaged material. (a) 930. (b) P-1700. (c) 840. (d) 956.

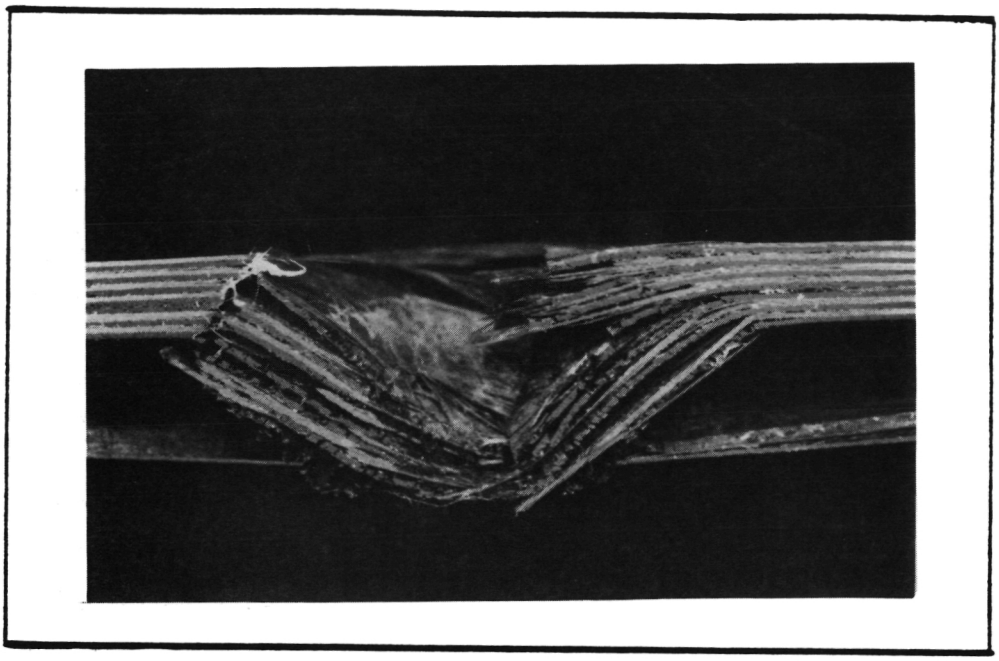

Magnification 5X

(a)

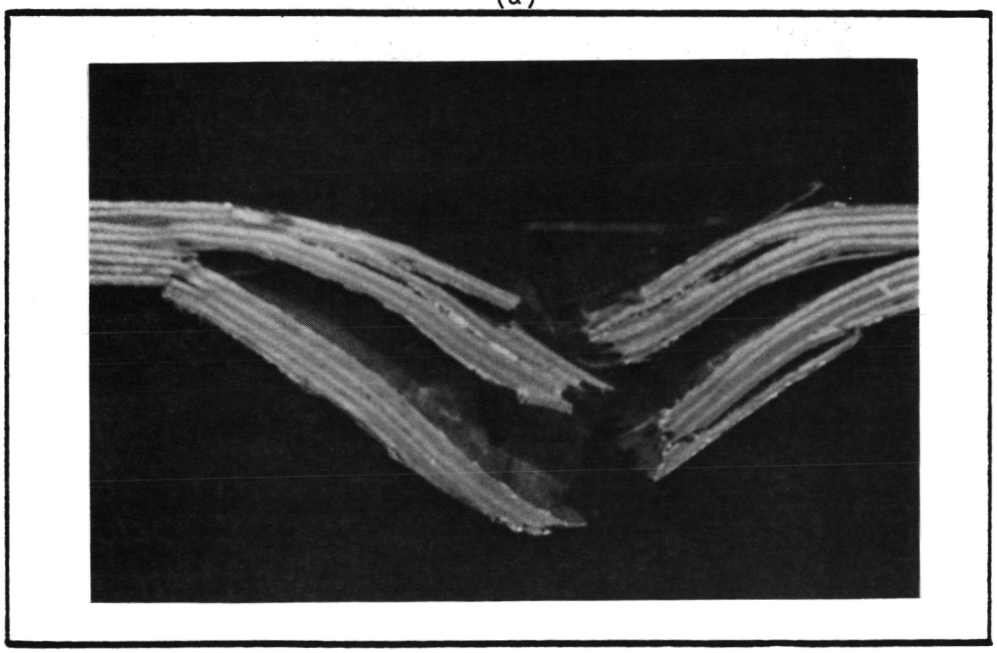

Magnification 5X

(b)

Figure 40. Cross sections of fifteen ply 930 and P-1700 crossplied composites after full penetration impact. Note the difference in the number of delaminations in the two specimens. (a) 930. (b) P-1700.

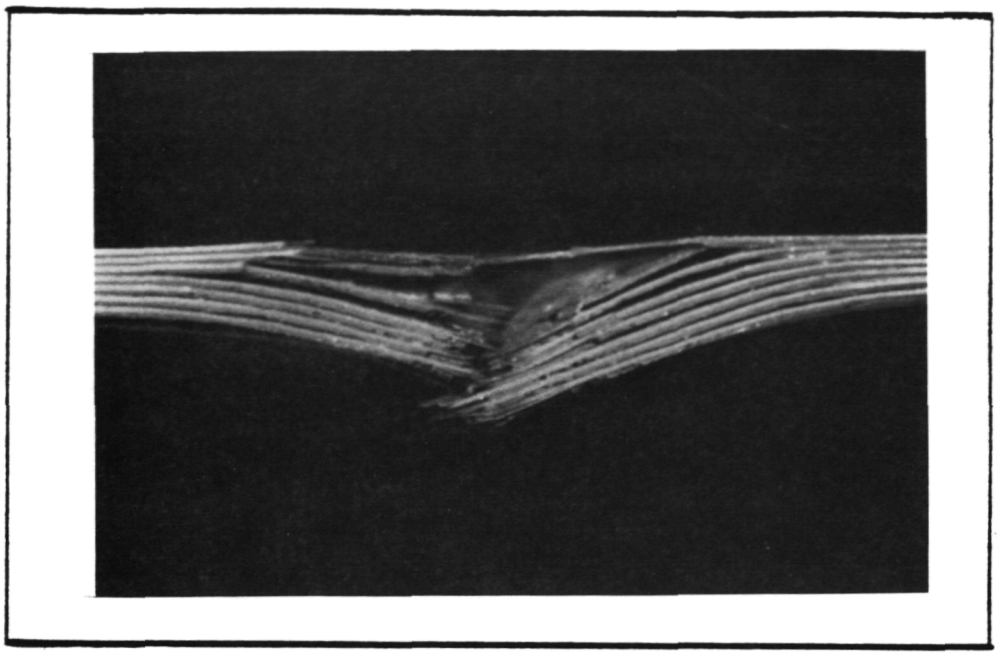

Magnification 5X

(a)

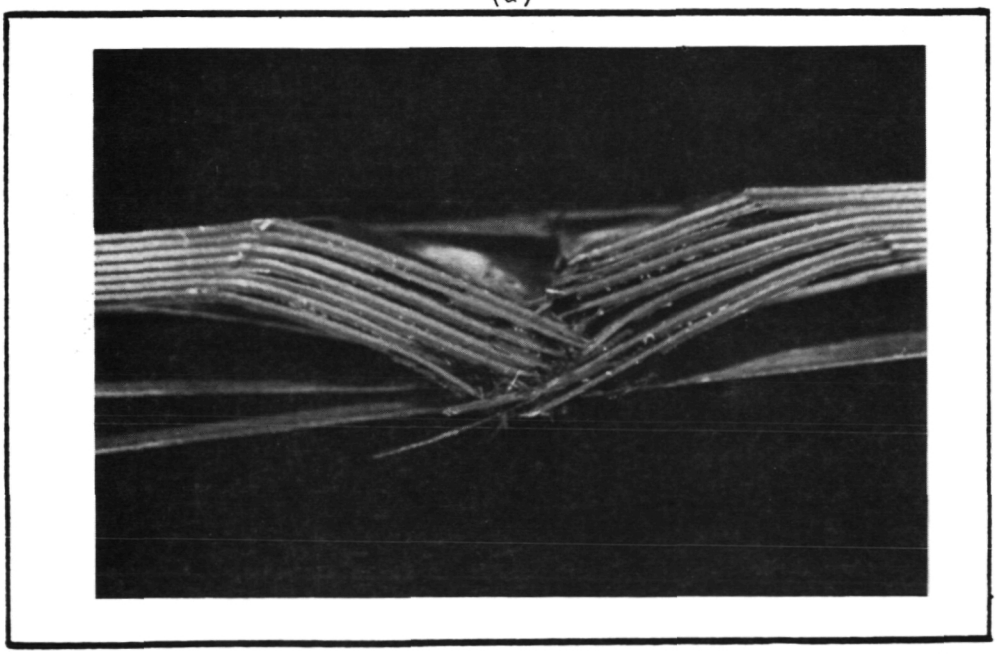

Magnification 5X

(b)

Figure 41. Cross sections of fifteen ply 840 and 956 crossplied composites after full penetration impact. (a) 840. (b) 956.

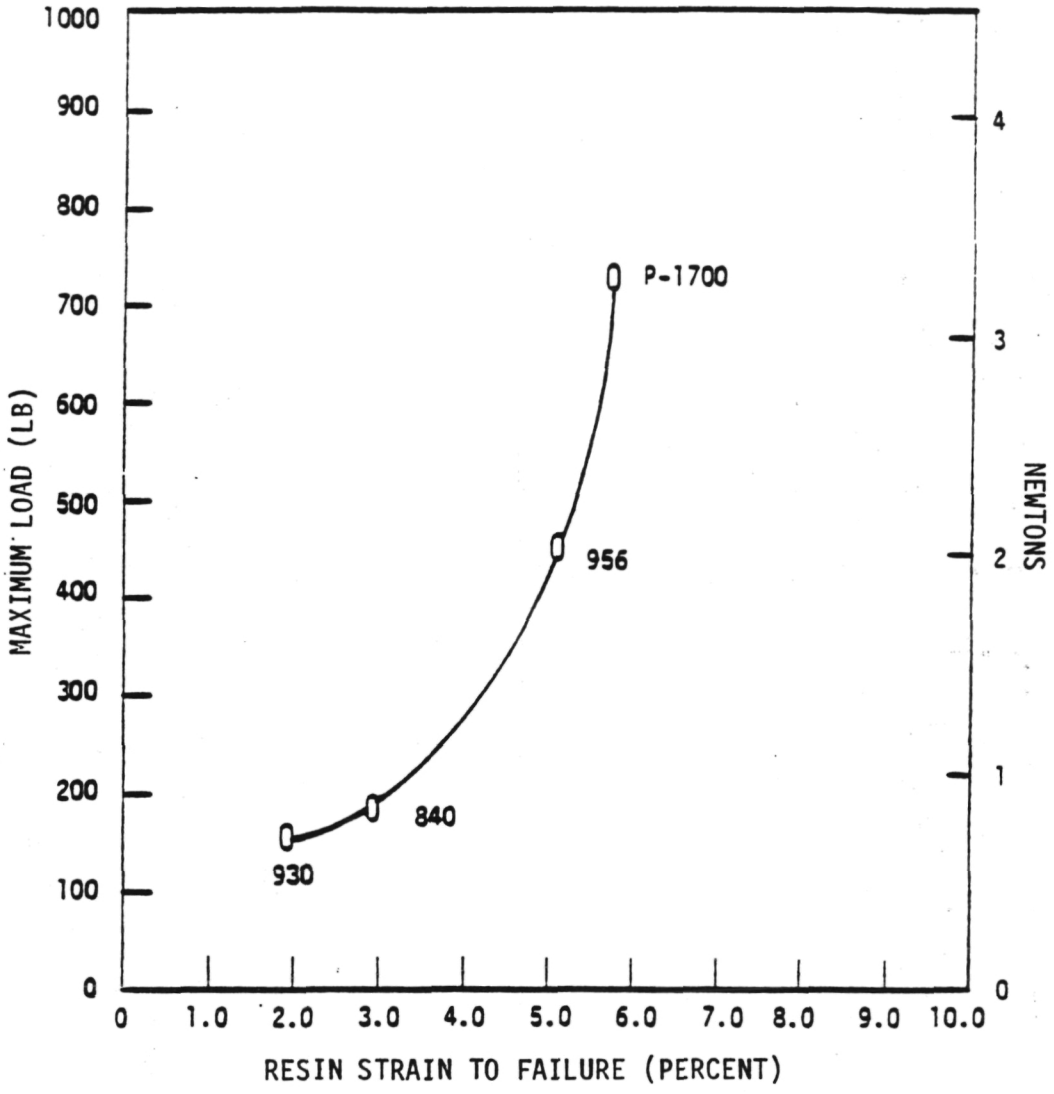

Figure 42. Values of load at failure of the four matrix resins during impact and the yield or fracture strain for each of the resins.

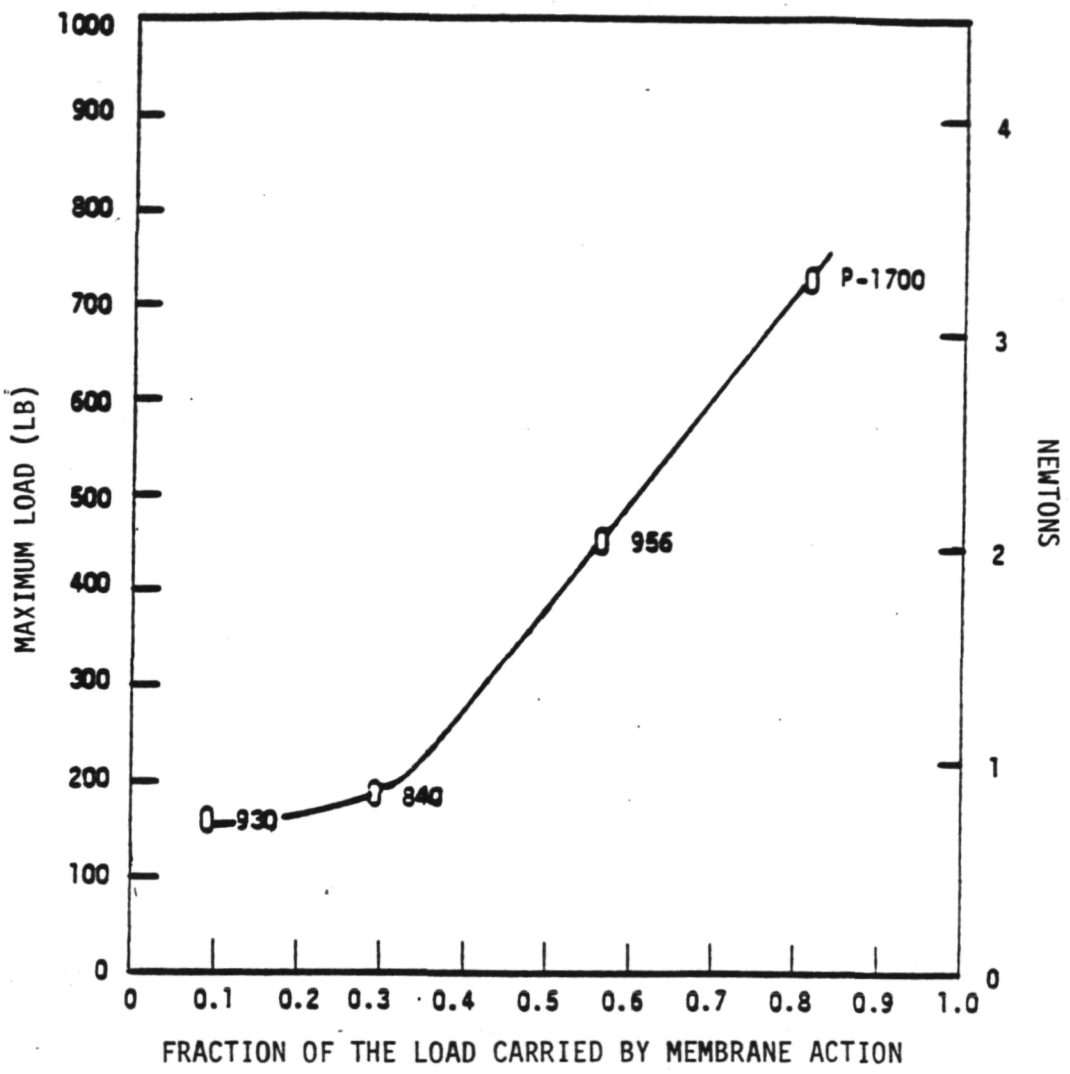

Figure 43. The load at failure and the fraction of the load carried by membrane action for each of the four matrix resins used in this study.

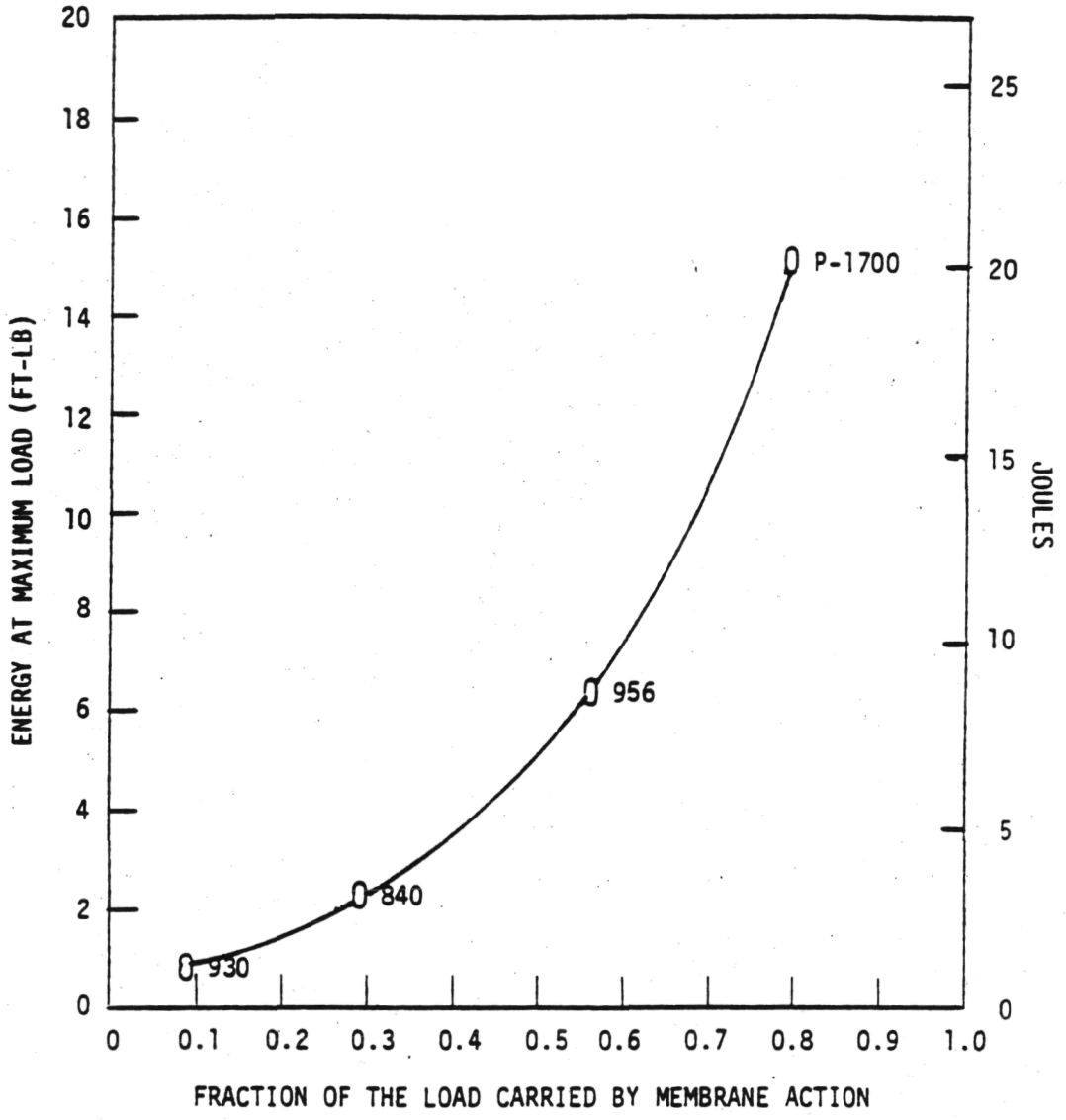

Figure 44. The energy absorbed up to the time of failure and the fraction of the load carried by membrane action for each of the four resins used in this study.

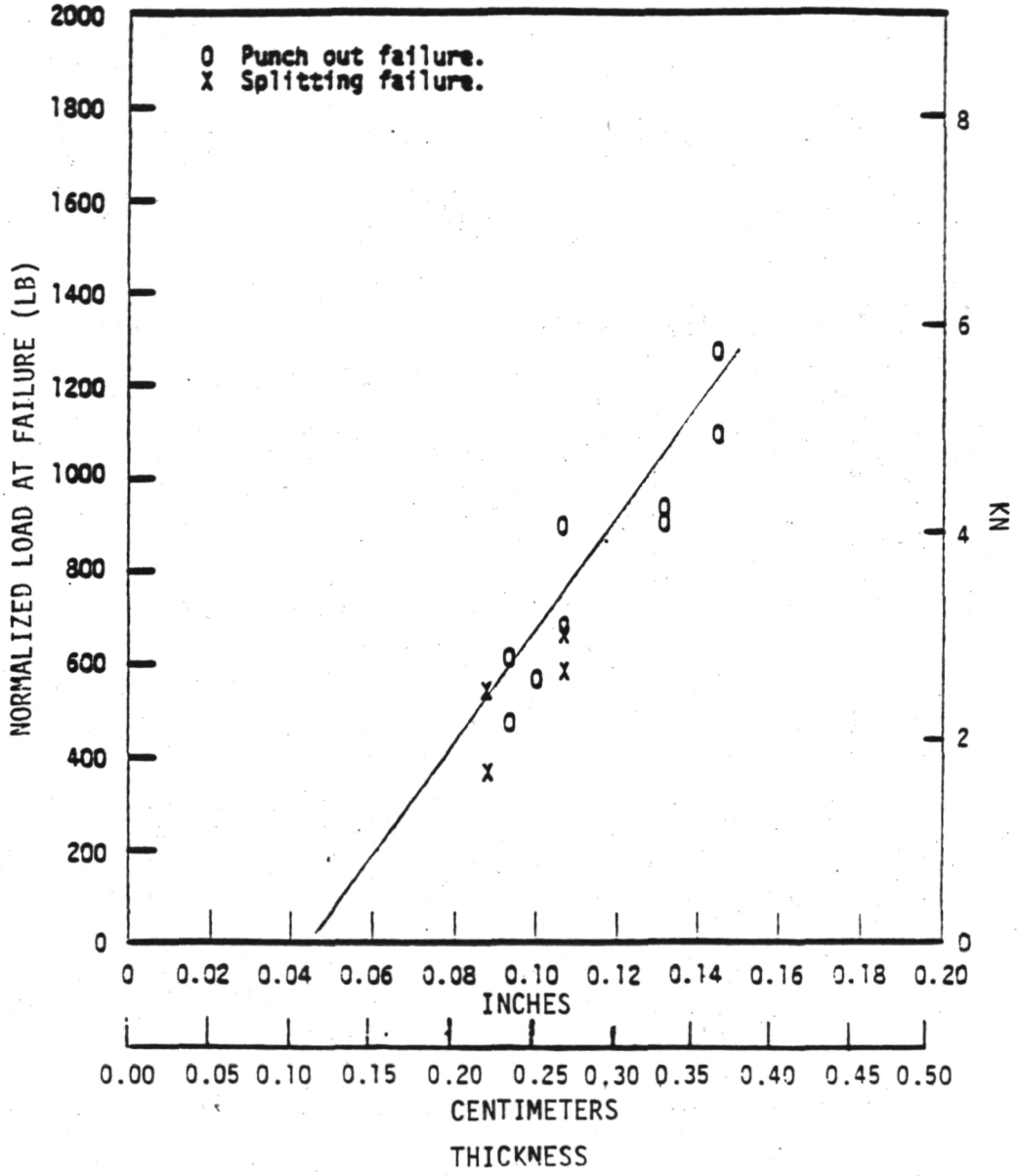

Figure 45. Normalized load at failure of impacted unidirectional composite of different thicknesses. Loads are normalized to 60 volume percent of fiber.

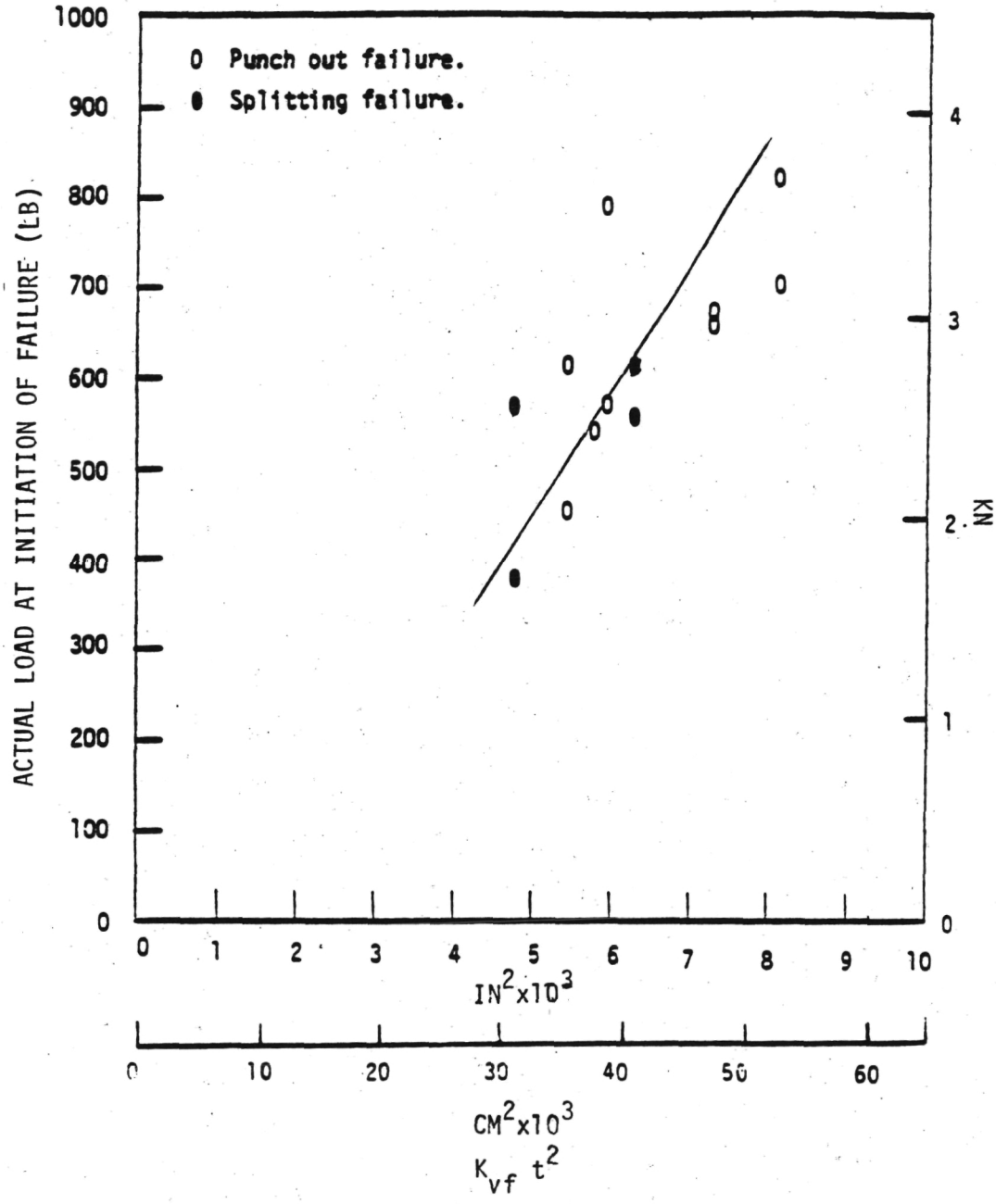

Figure 46. Actual load at failure of impacted unidirectional composites of different thicknesses and fiber volume fractions. The abscissa is a factor which relates load to the thickness and fiber volume fraction for a beam clamped at both ends.

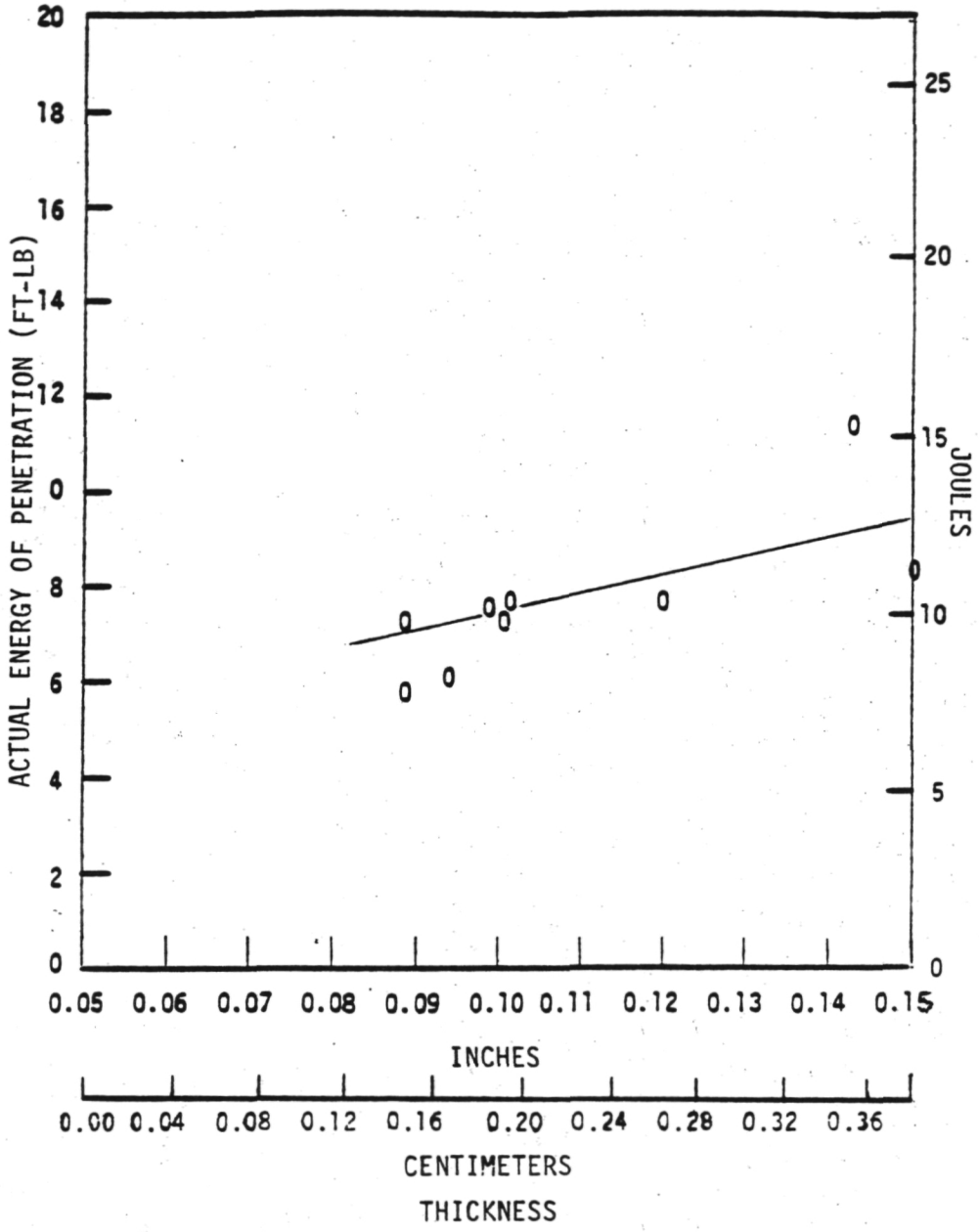

Figure 47. Actual energies of penetration for impacted unidirectional composites of different thicknesses.

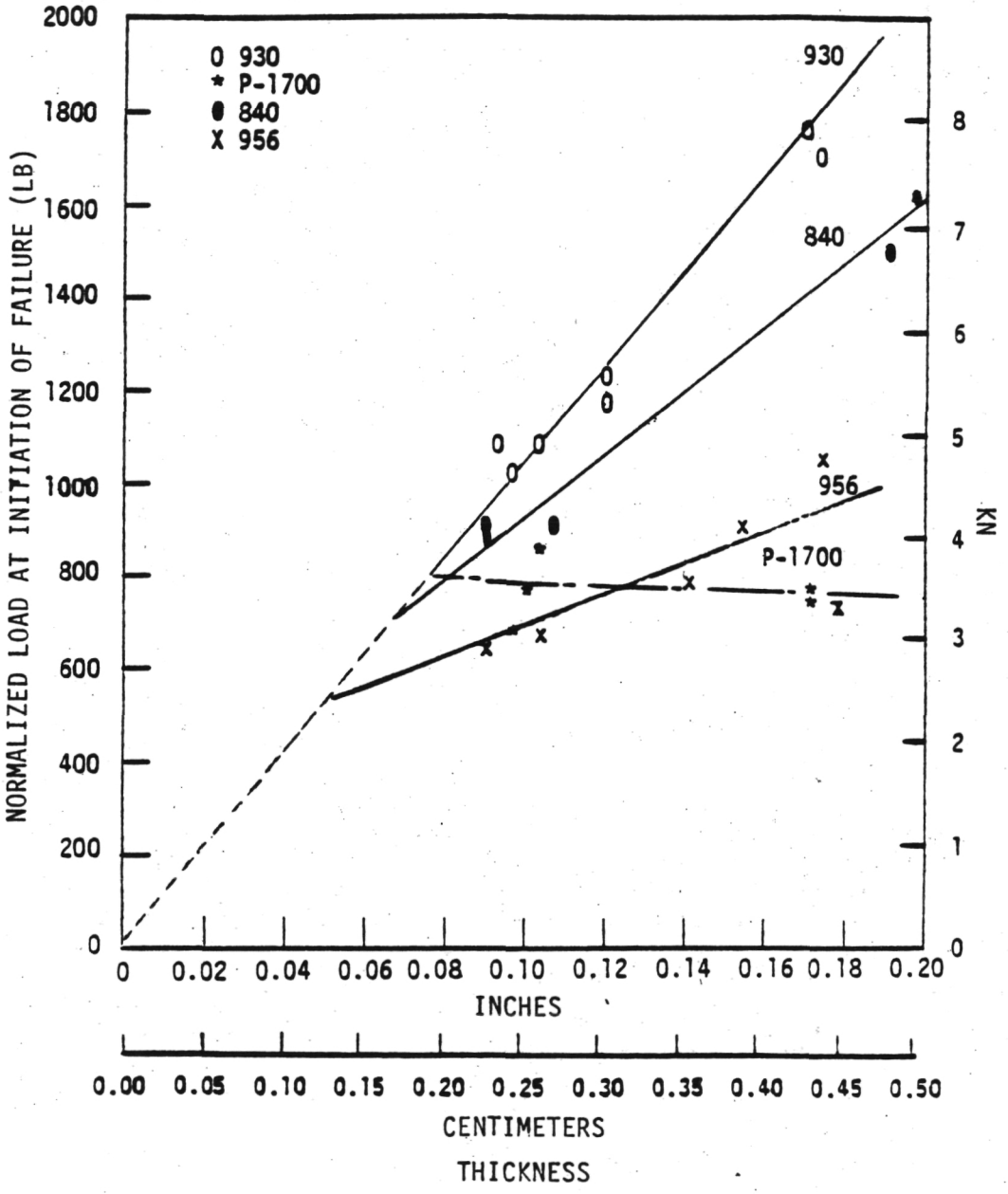

Figure 48. Normalized loads at initiation of failure for crossplied composites of different thicknesses. Loads are normalized to 60 volume percent of fiber.

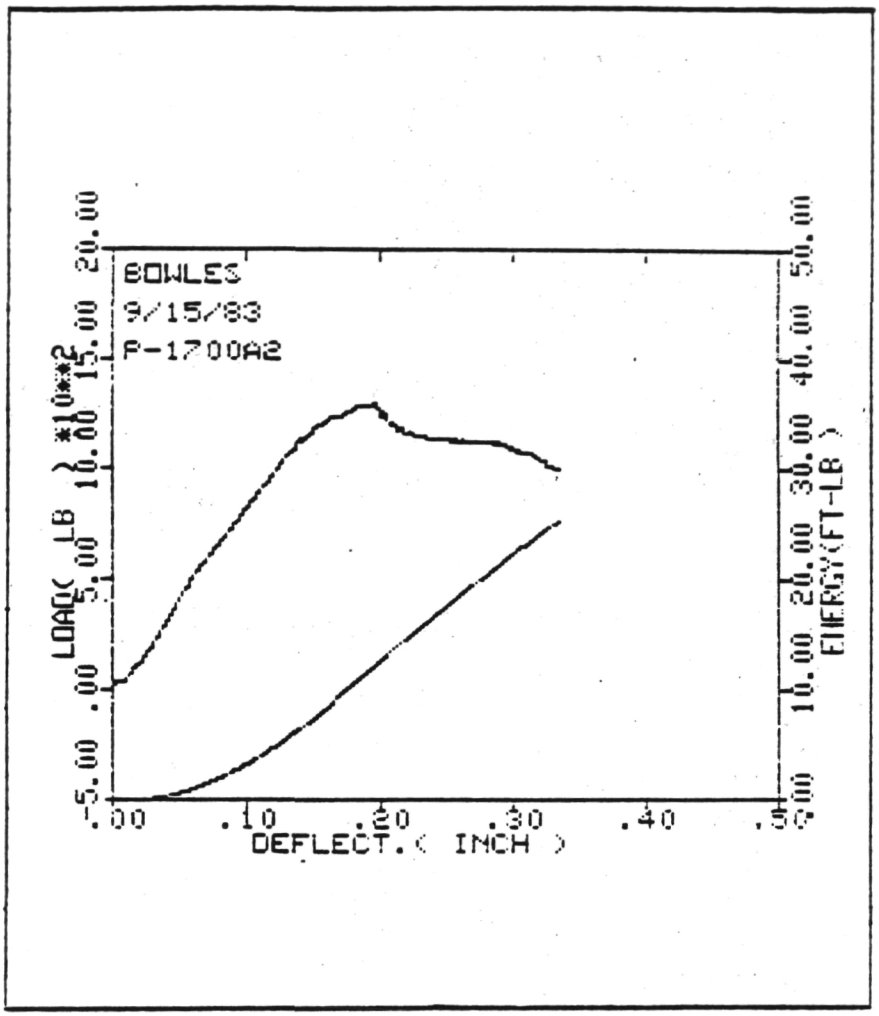

Figure 49. Load deflection and energy-deflection curves recorded during impact of thirty ply P-1700 crossplied composite.

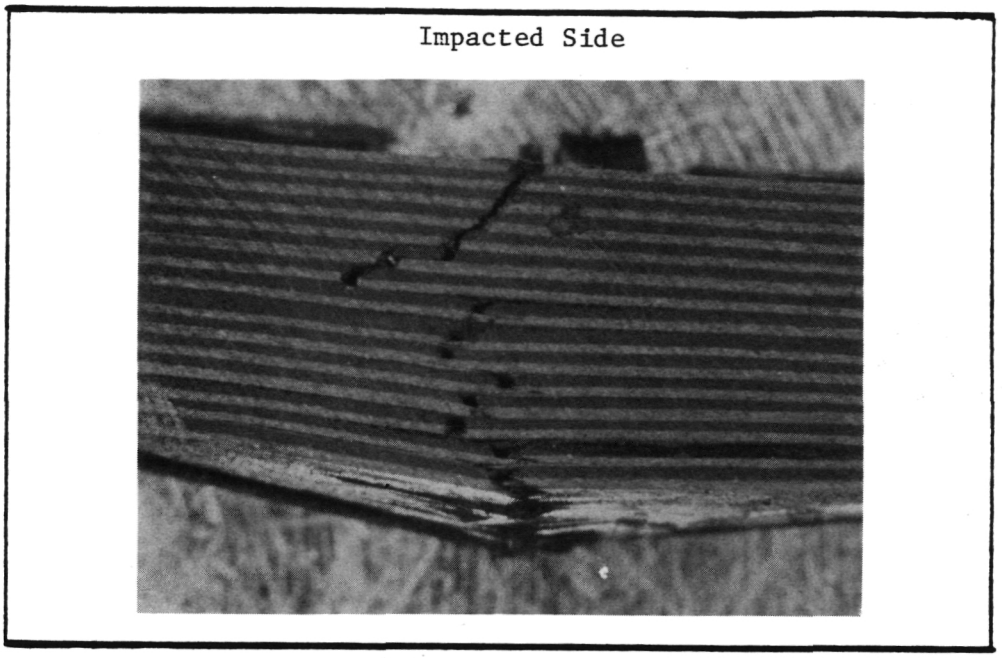

Magnification 10X

(a)

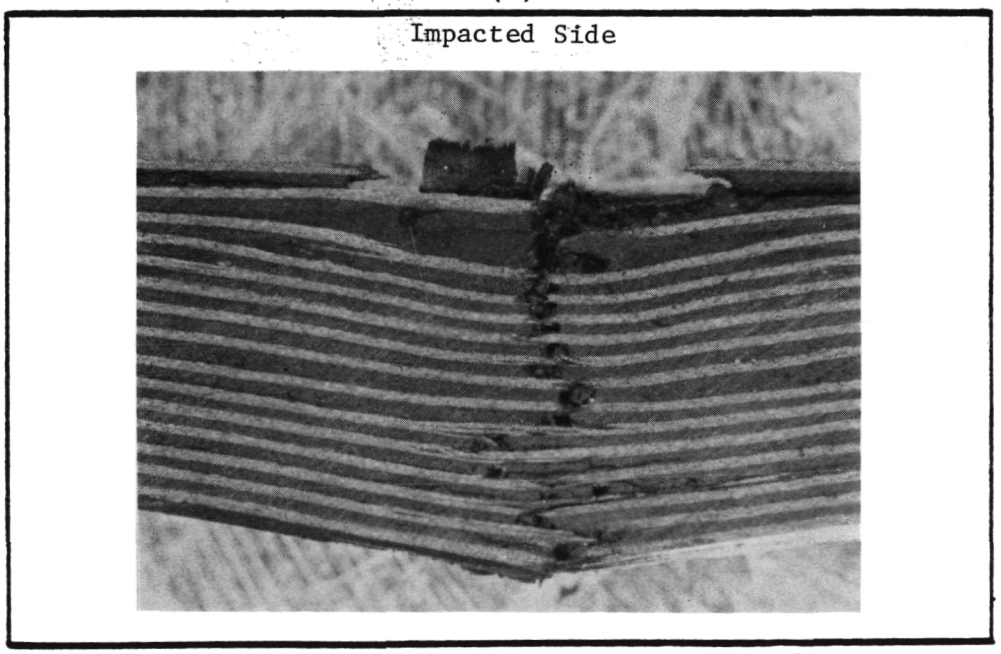

Magnification 10X

(b)

Figure 50. Cross section of the impacted area of the thirty ply 840 crossplied composite. Note the extent of fiber fracture through the thickness. (a) Impact site. (b) Edge of impact site.

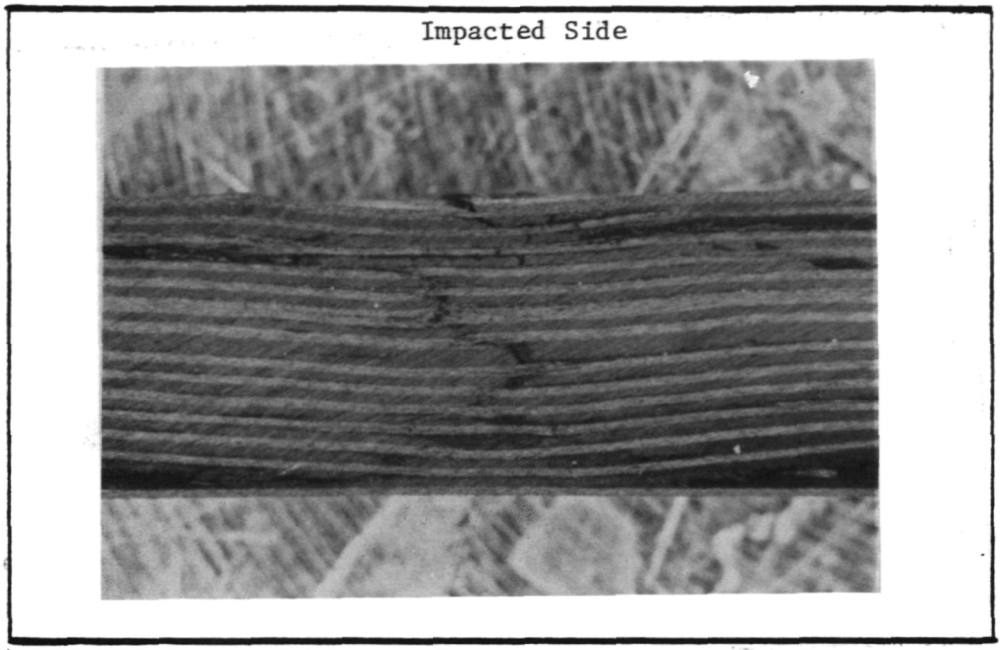

Magnification 10X

(a)

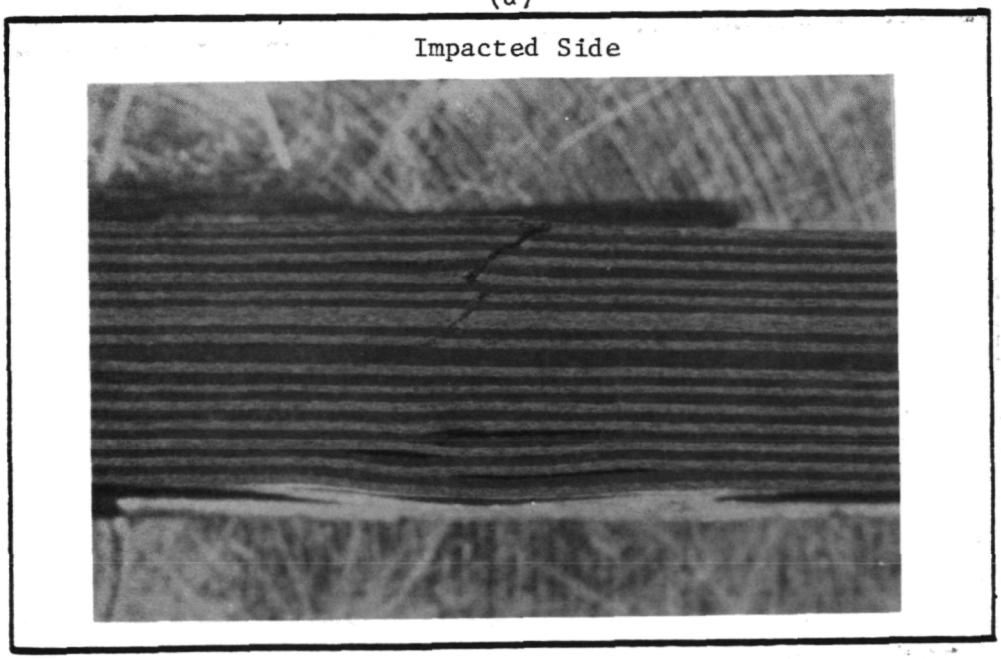

Magnification 10X

(b)

Figure 51. Cross section of the impacted area of the thirty ply 956 crossplied composite. Note the extensive amount of delamination throughout the thickness. (a) Impact site. (b) Edge of impact site.

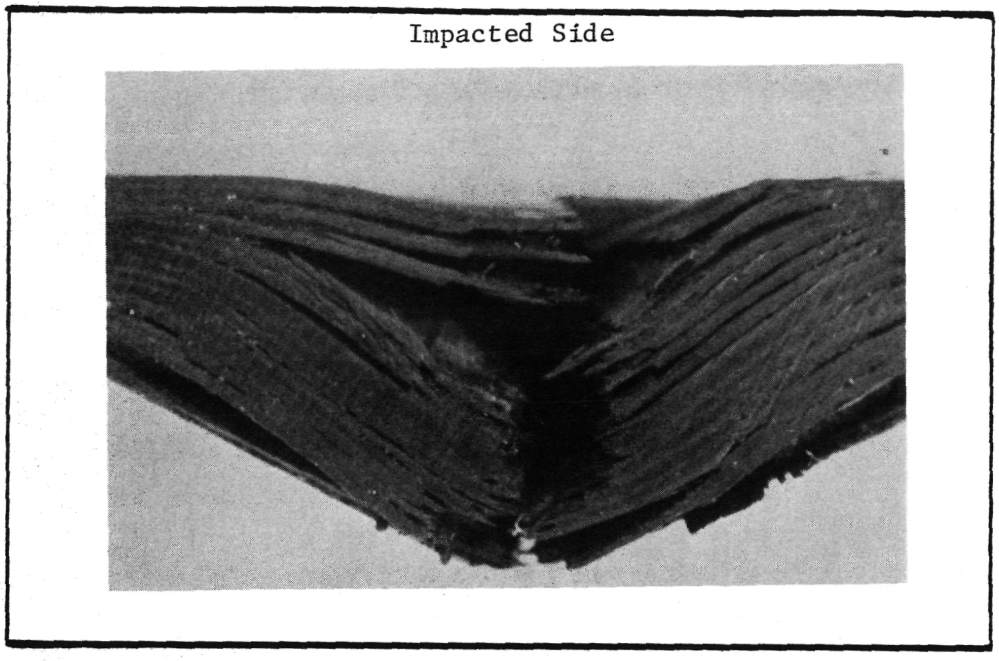

(a) Magnification 10X

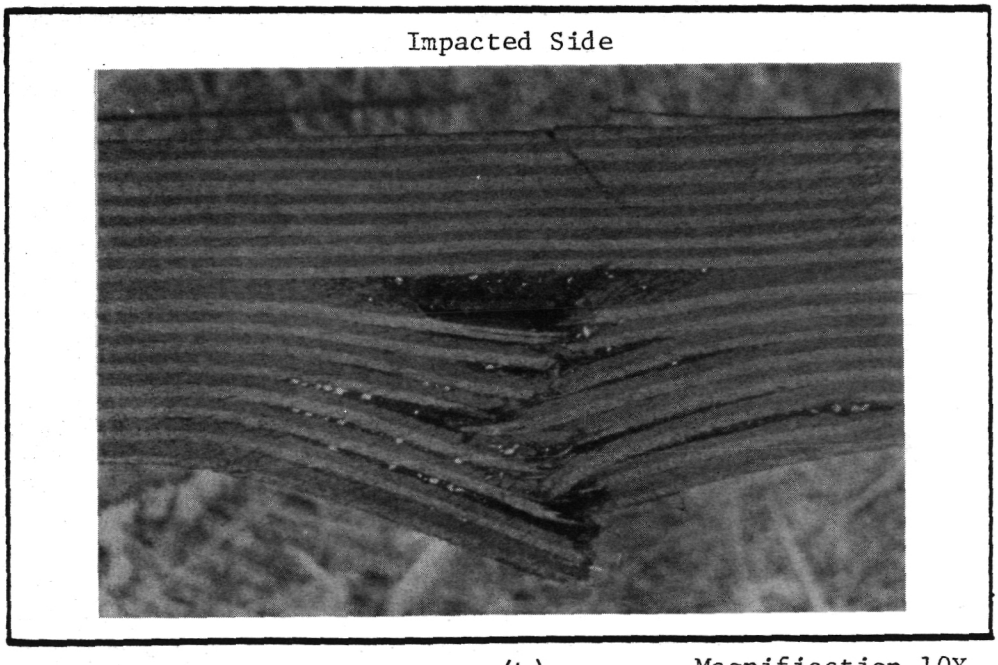

(b) Magnification 10X

Figure 52. Cross section of the impact damaged area of the thirty ply P-1700 crossplied composite. (a) Impact site. (b) Edge of impact site.

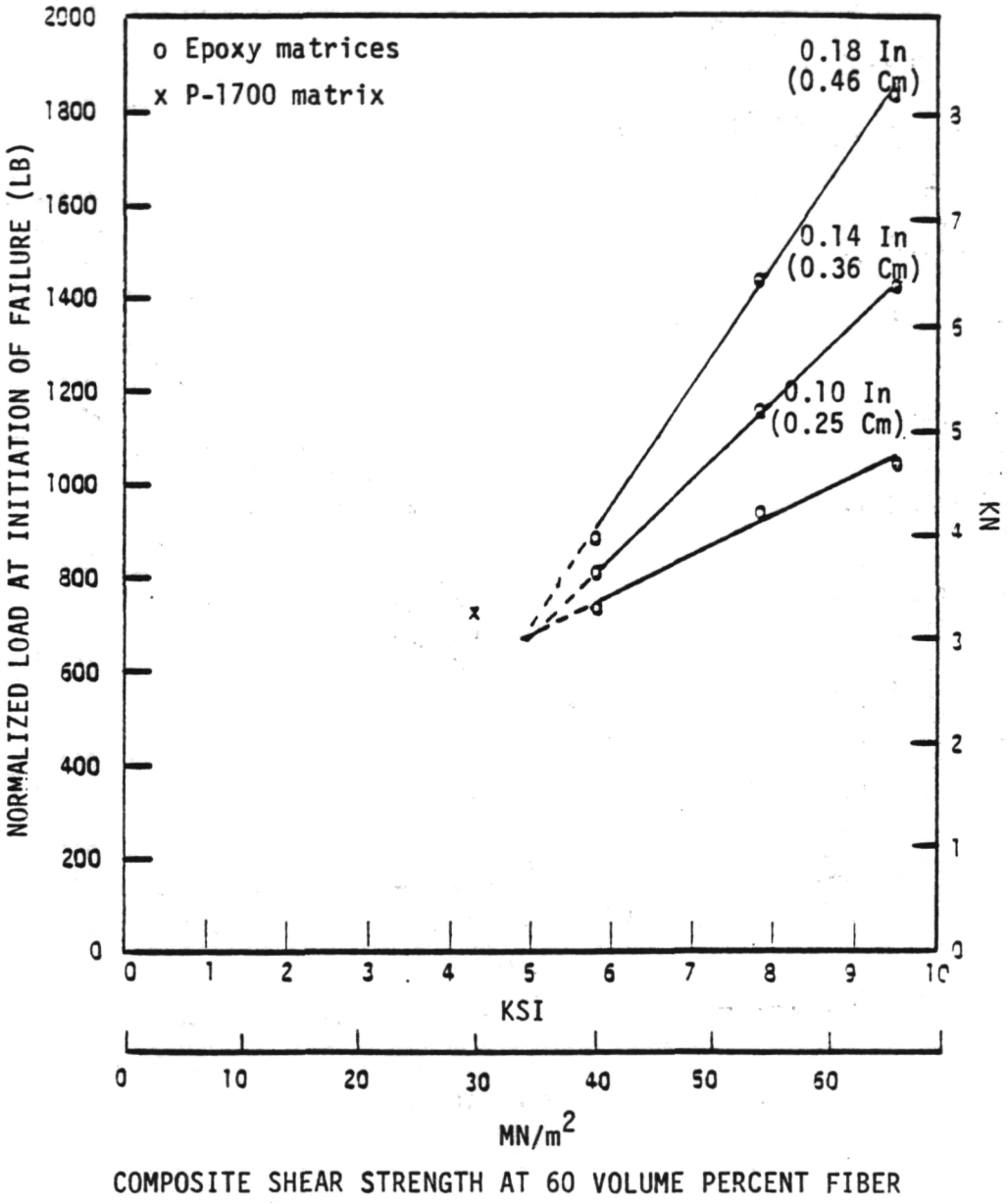

Figure 53. Normalized loads at initiation of damage and composite shear strengths for the thirty ply crossplied composites.

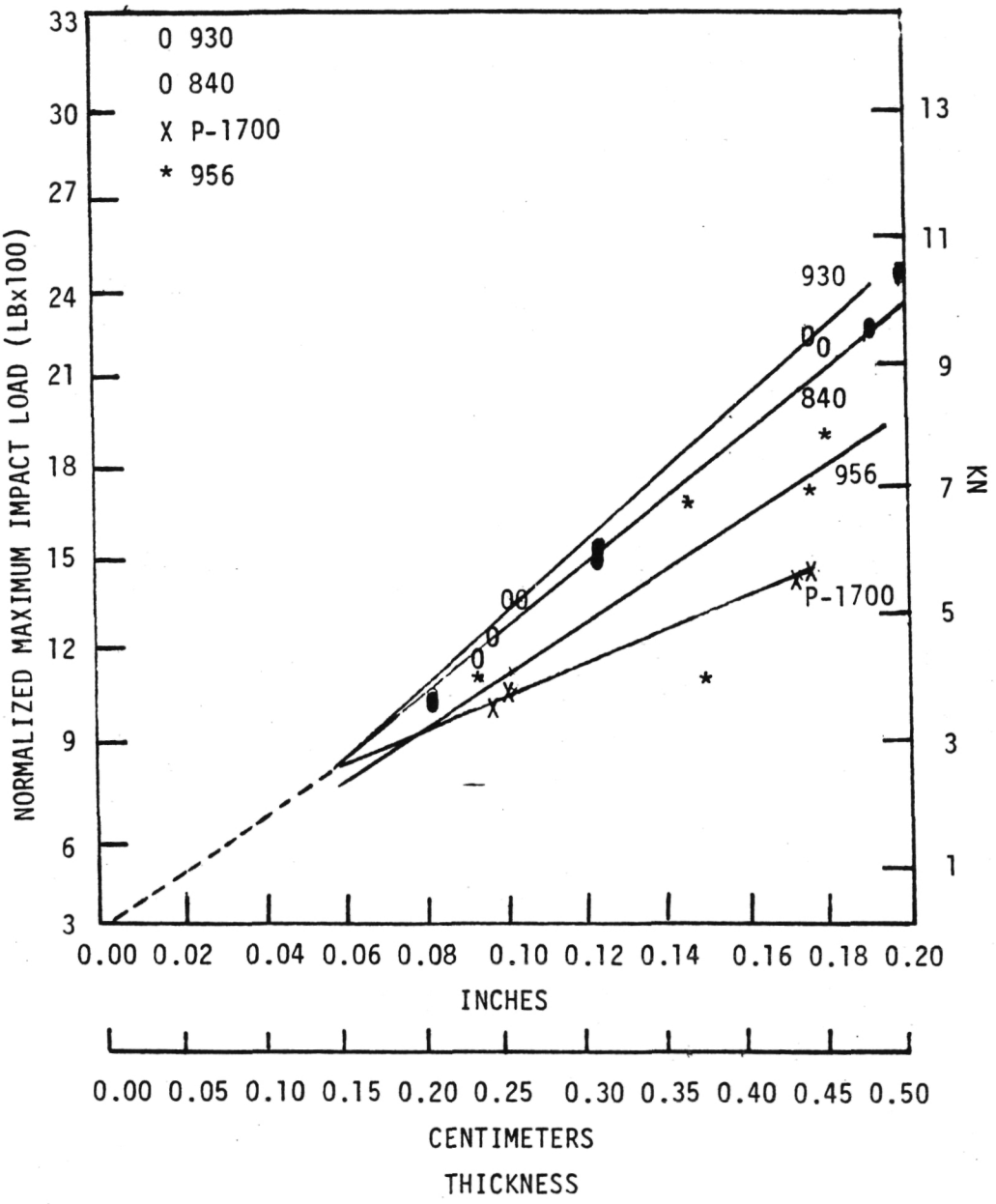

Figure 54. Normalized maximum impact loads for crossplied composites of different thicknesses. Loads are normalized to sixty volume percent of fiber.

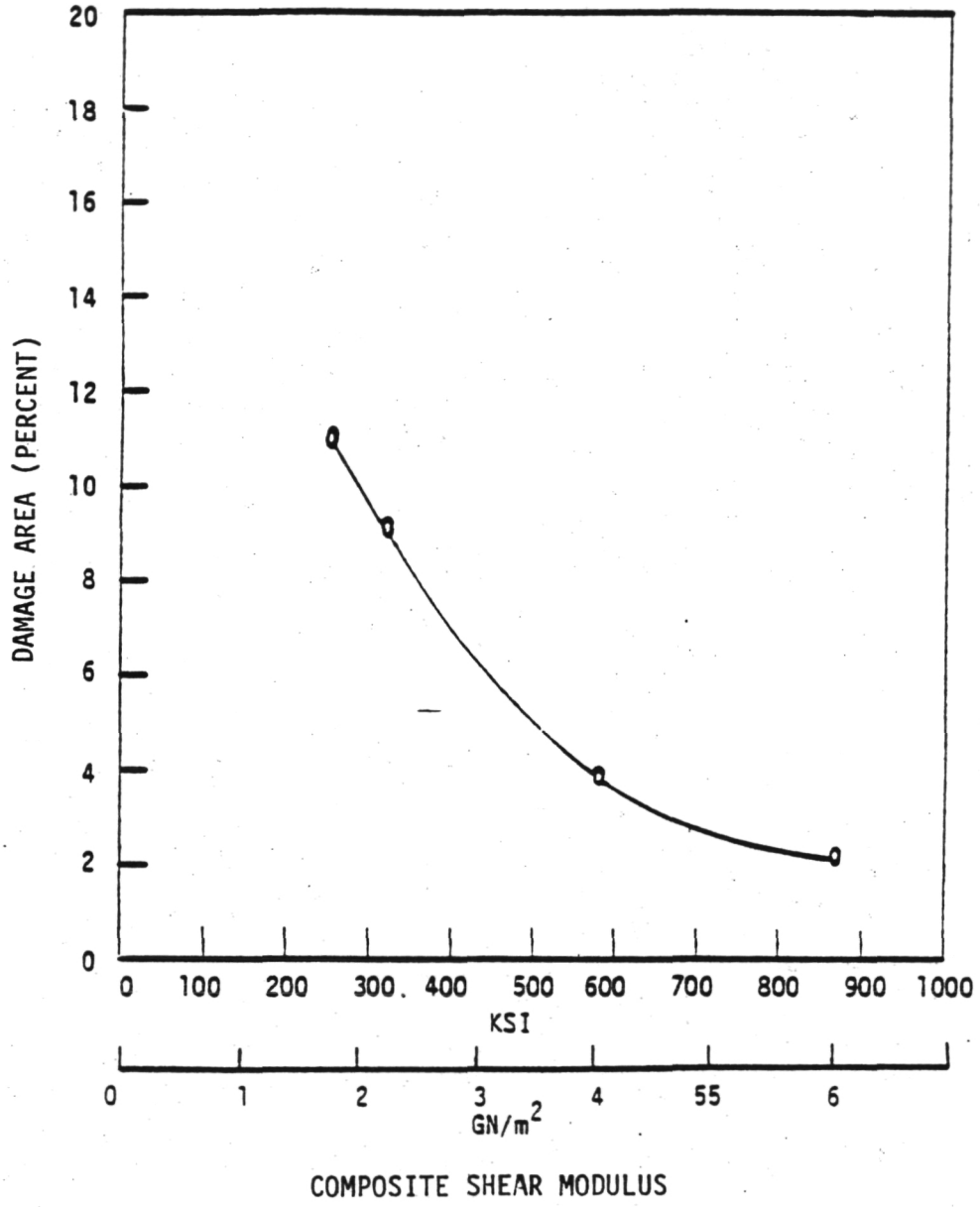

Figure 55. Internal damage area of thirty ply crossplied composites with different shear moduli. Damage area presented as percent of lamirate surface area exposed to the impact.

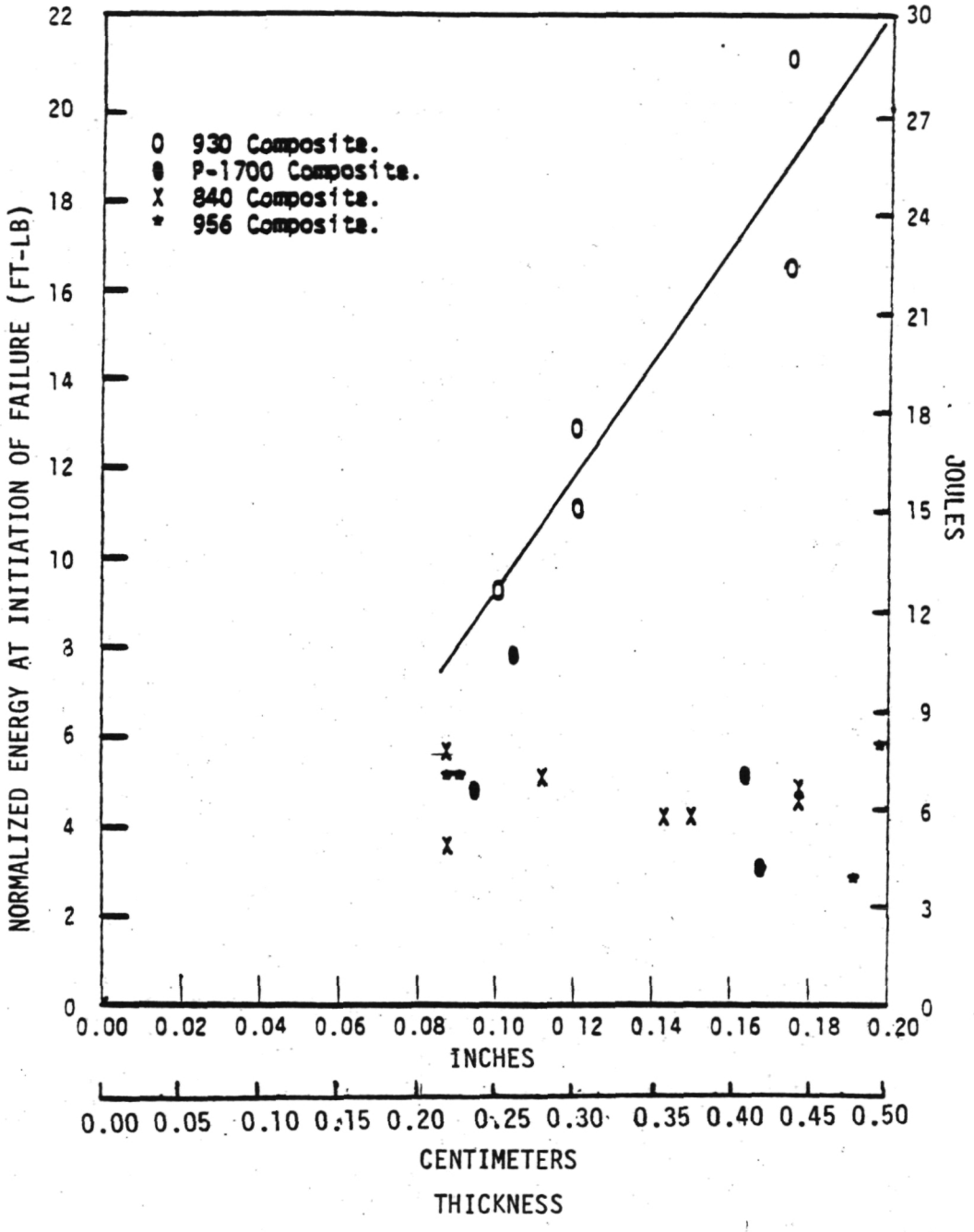

Figure 56. Normalized energies at initiation of damage for crossplied composites of different thicknesses. Data normalized to 60 volume percent fiber.

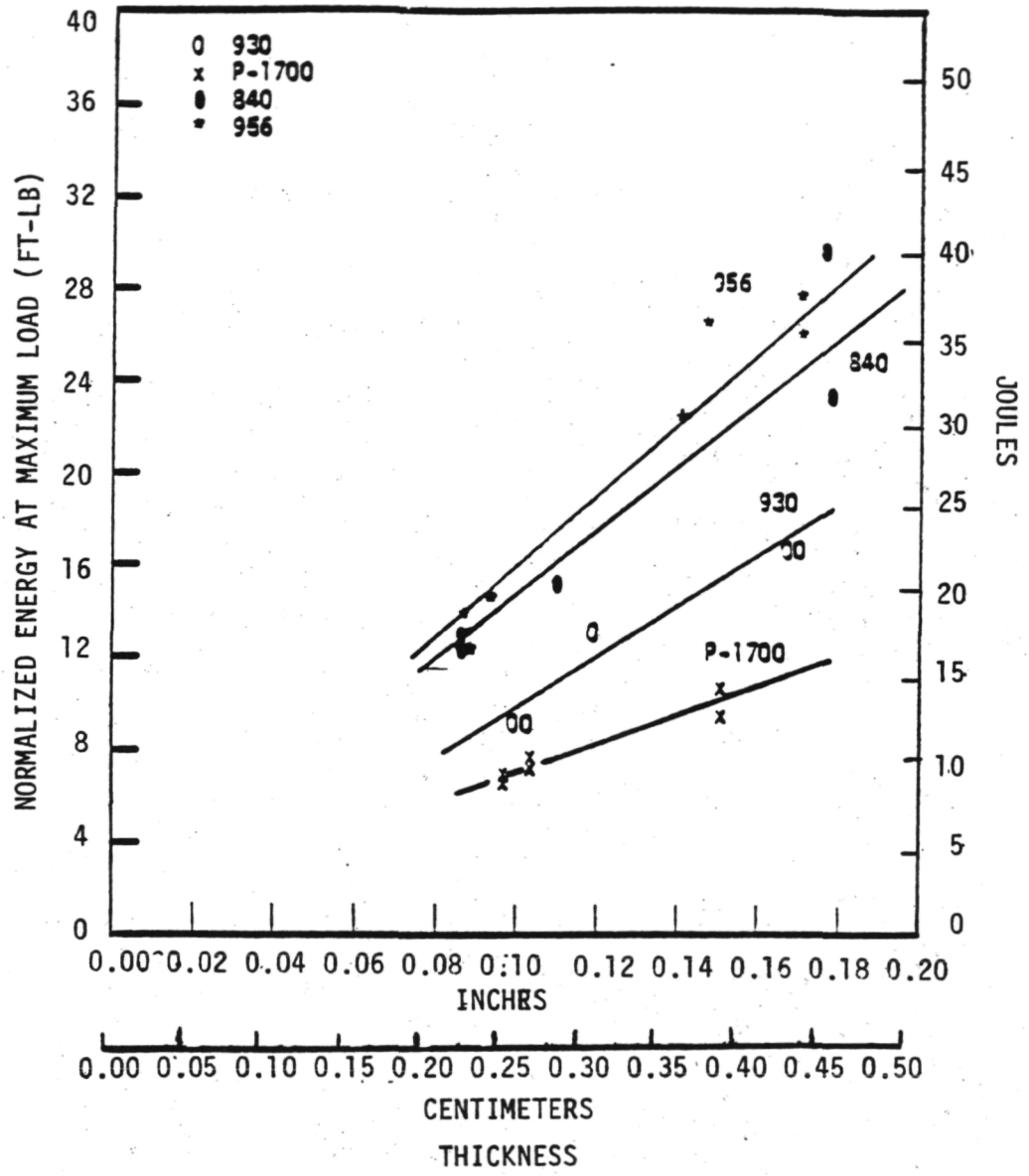

Figure 57. Normalized energies at maximum load for crossplied composites of different thicknesses. Note that the 956 composites do not correlate energy wise with the thickness. Energies are normalized to sixty volume percent.

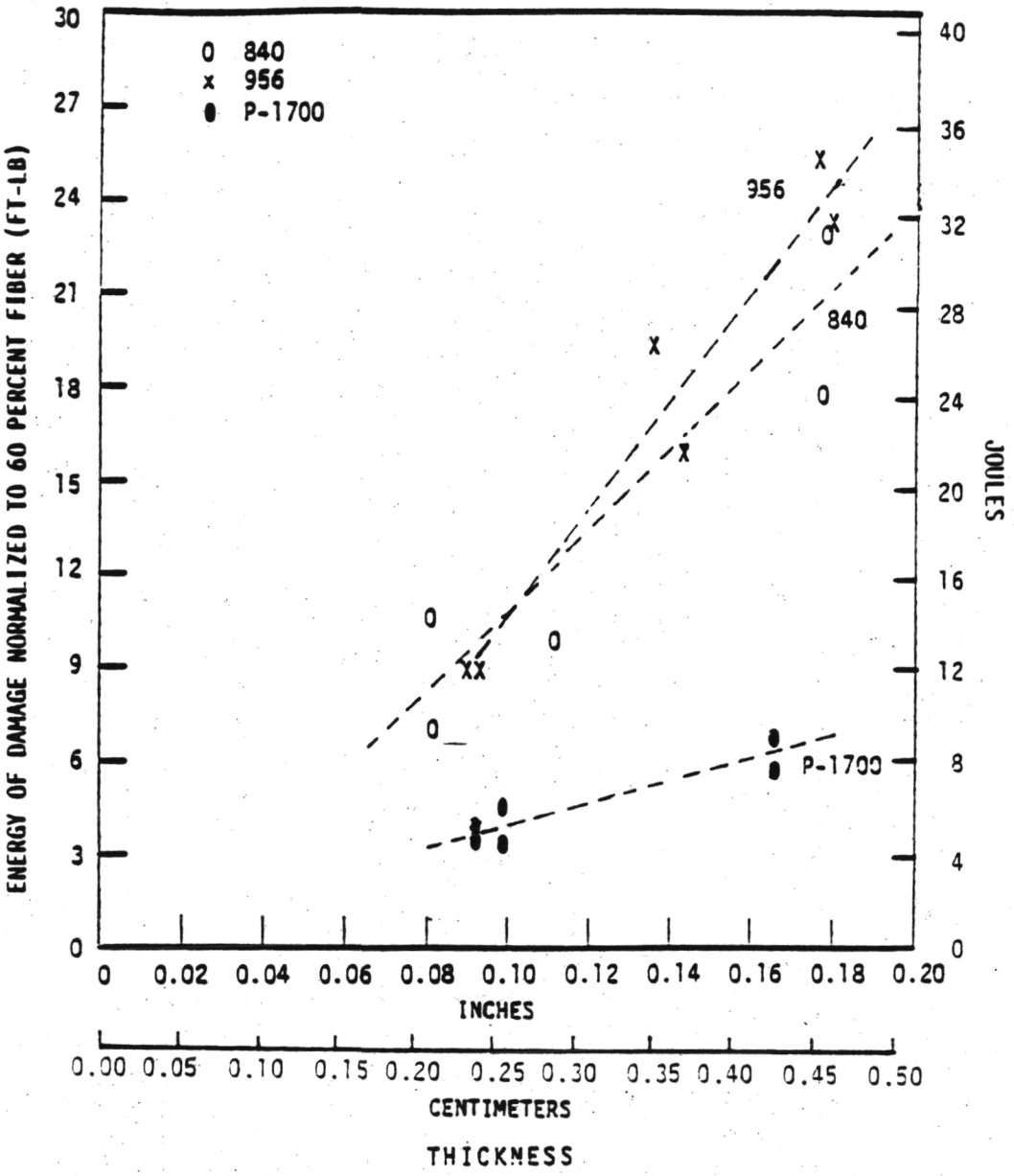

Figure 58. Normalized damage energies ($Q_m - Q_i$) for crossplied composites of different thicknesses. Energies are normalized to sixty volume percent.

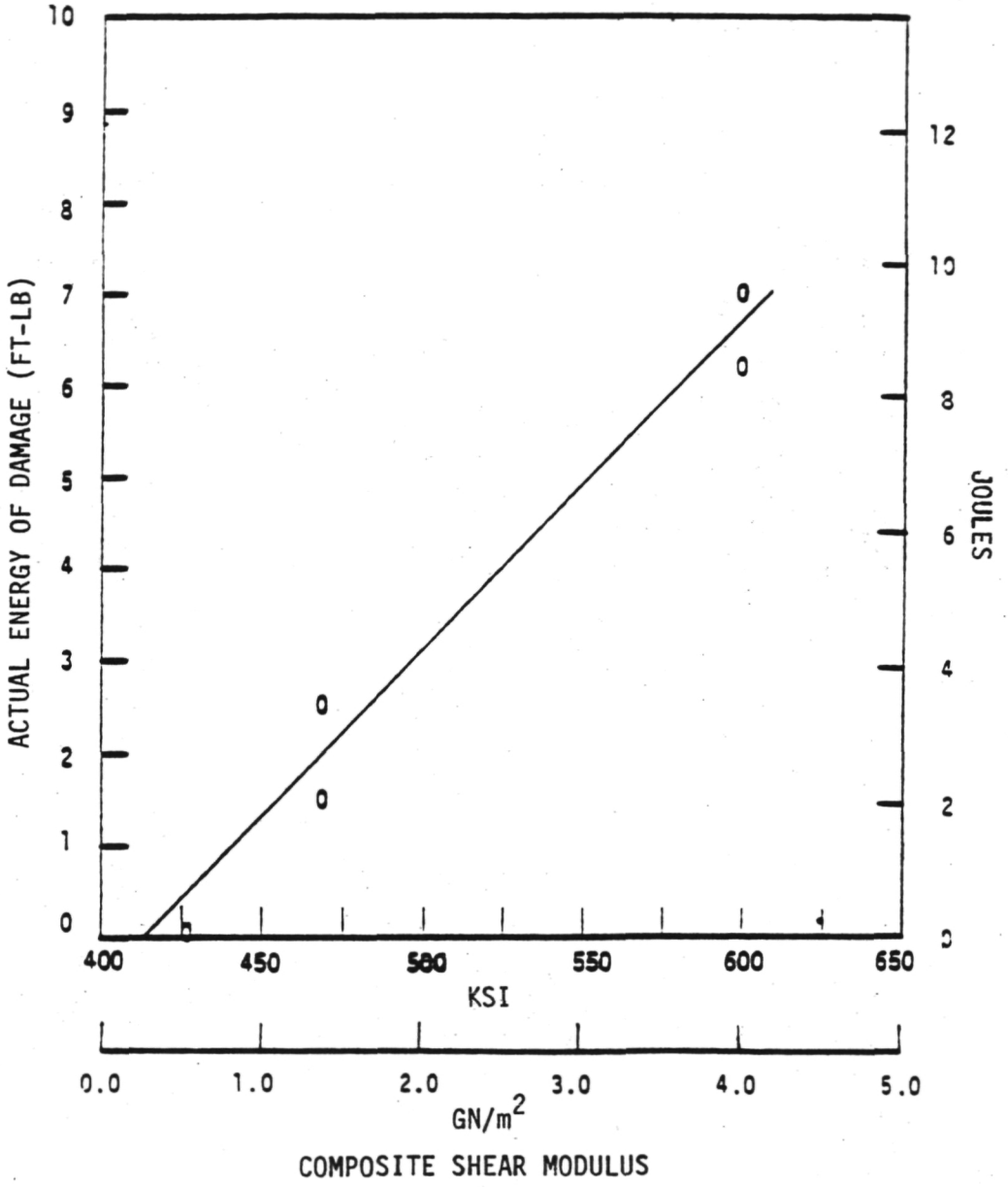

Figure 59. Actual damage energies for crossplied P-1700 composites with different shear moduli.

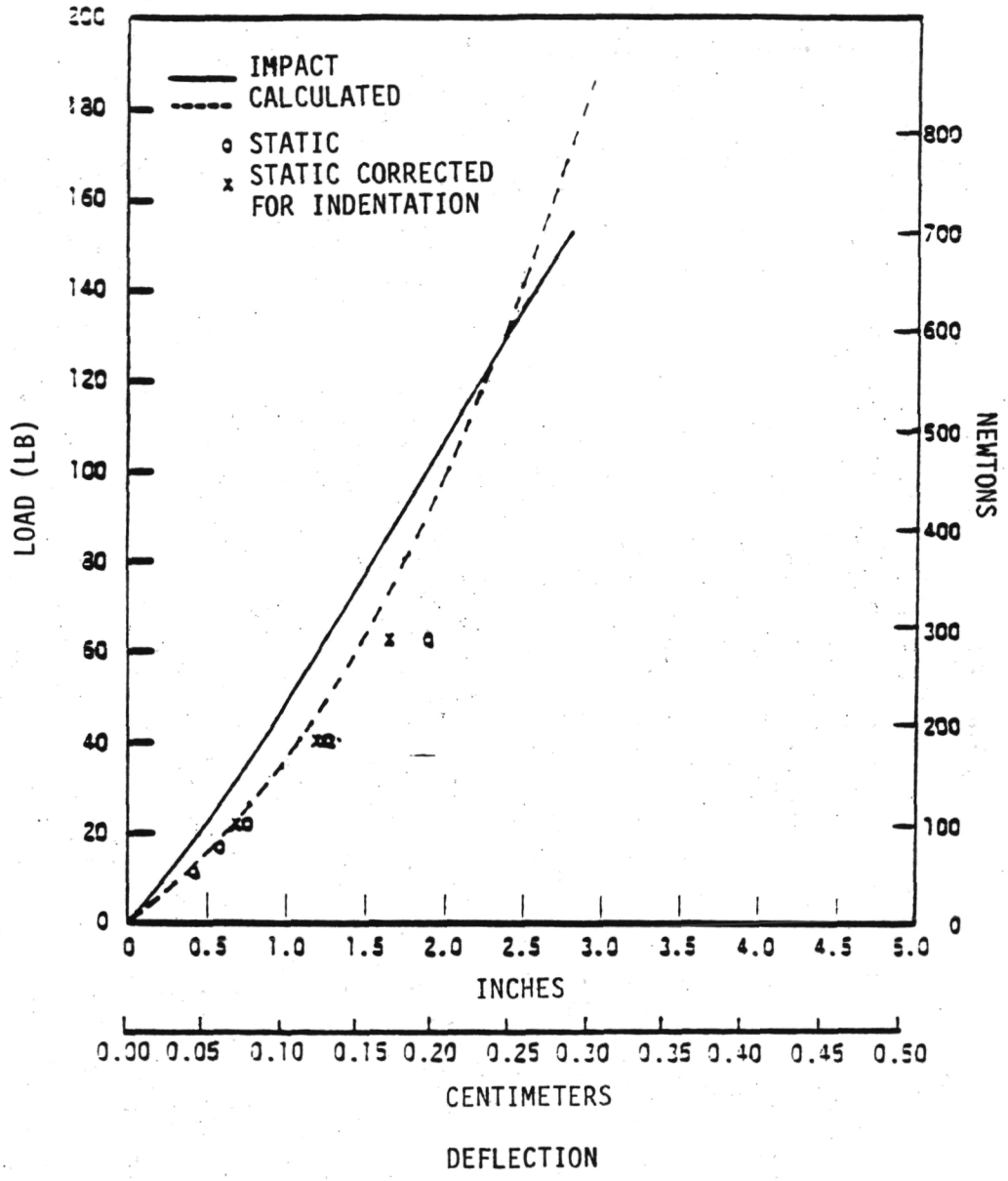

Figure 60. Dynamic, static and calculated values for load and deflection of an 840 resin plate. Deflections were calculated using the equation from Sturm and Moore (35). The location of the dynamic data above the calculated curve indicates the effect of strain rate sensitivity of the resin. Impact velocity was 8 ft/sec (244 cm/sec).

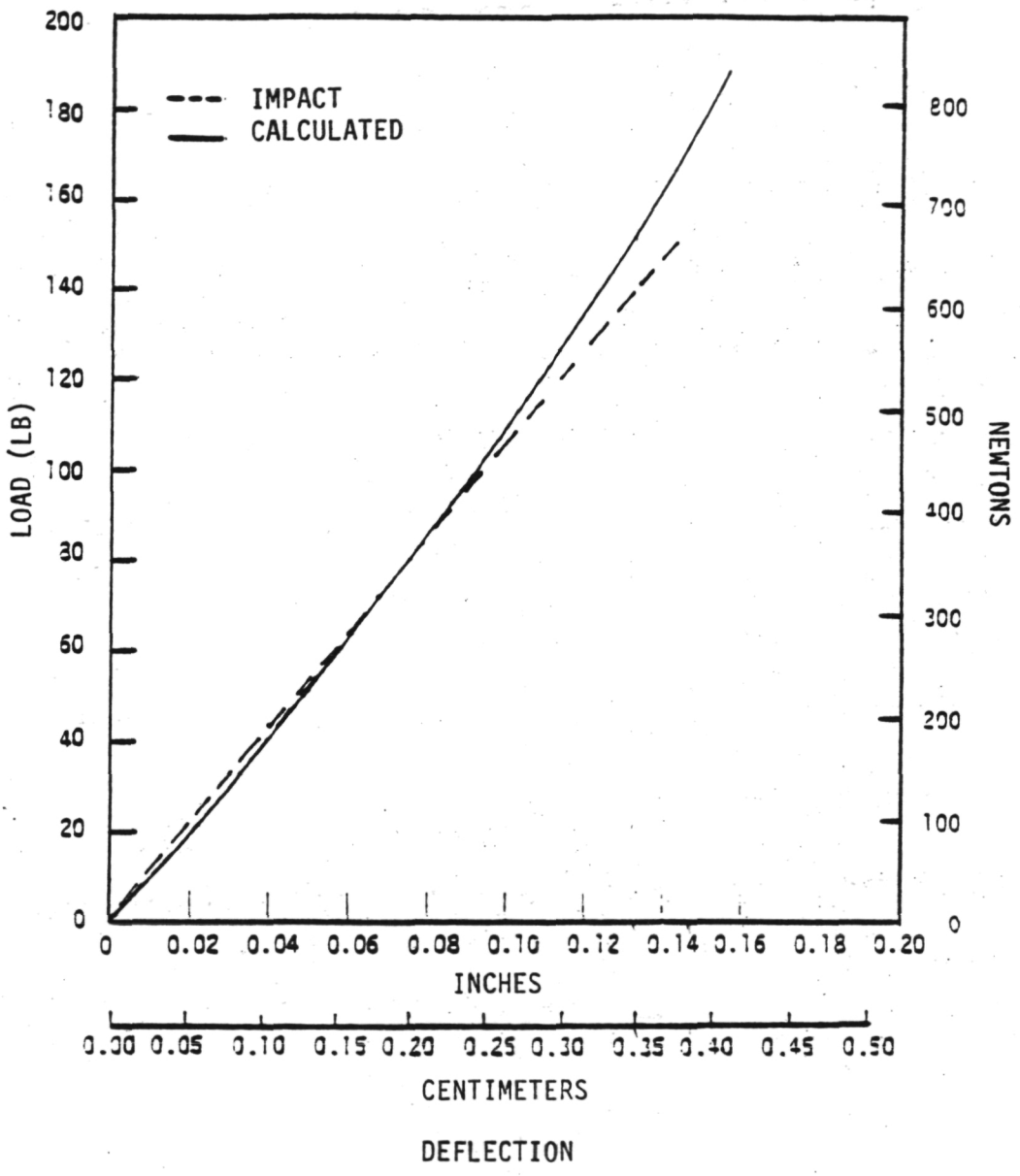

Figure 61. Calculated and dynamic load-deflection values for a 930 resin plate. Note that there is no indication of strain rate sensitivity. Impact velocity was 8 ft/sec (244 cm/sec).

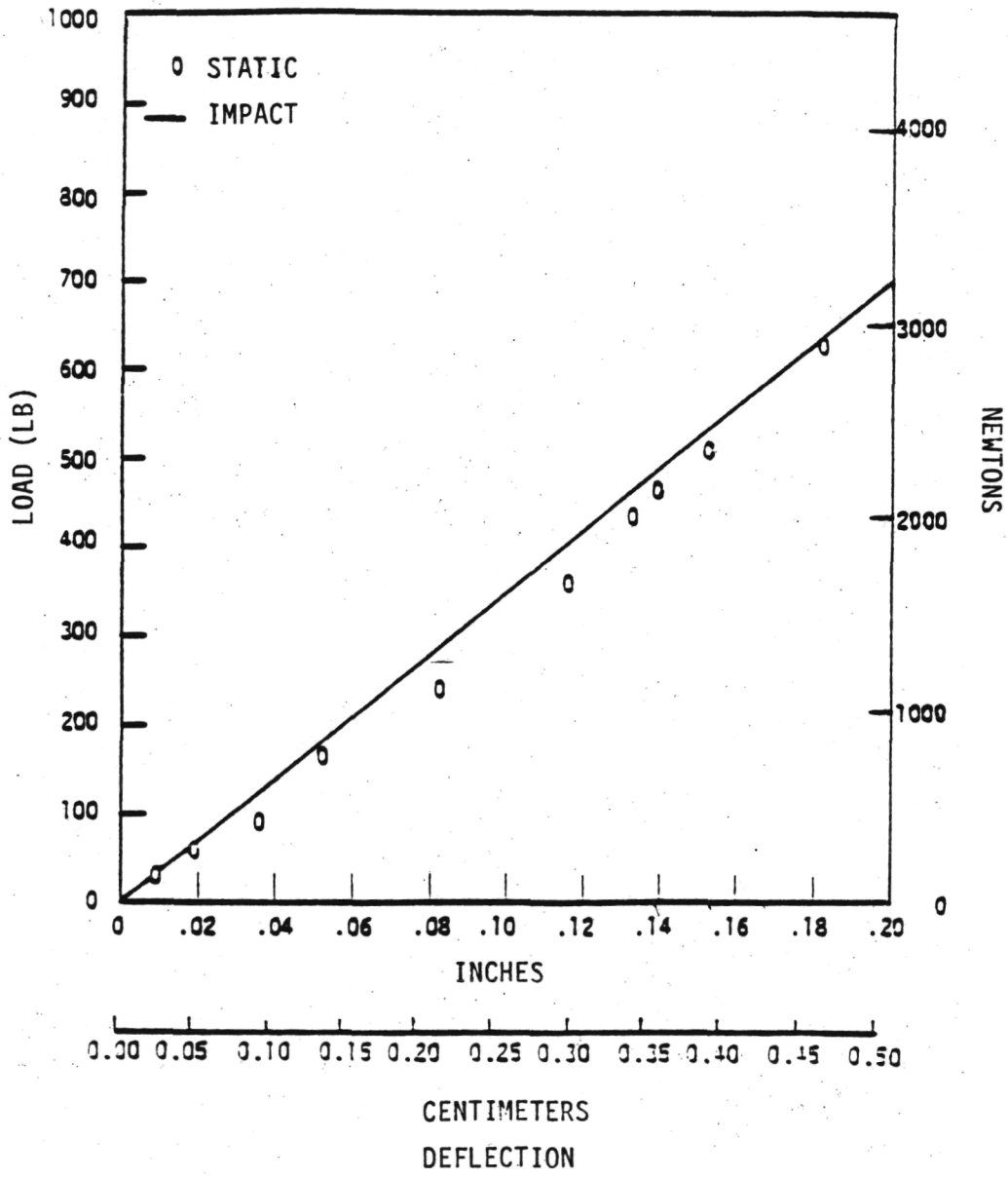

Figure 62. Dynamic and static load deflection data for the fifteen ply, crossplied 840 composite. Impacting velocity was 8 ft/sec (244 cm/sec).

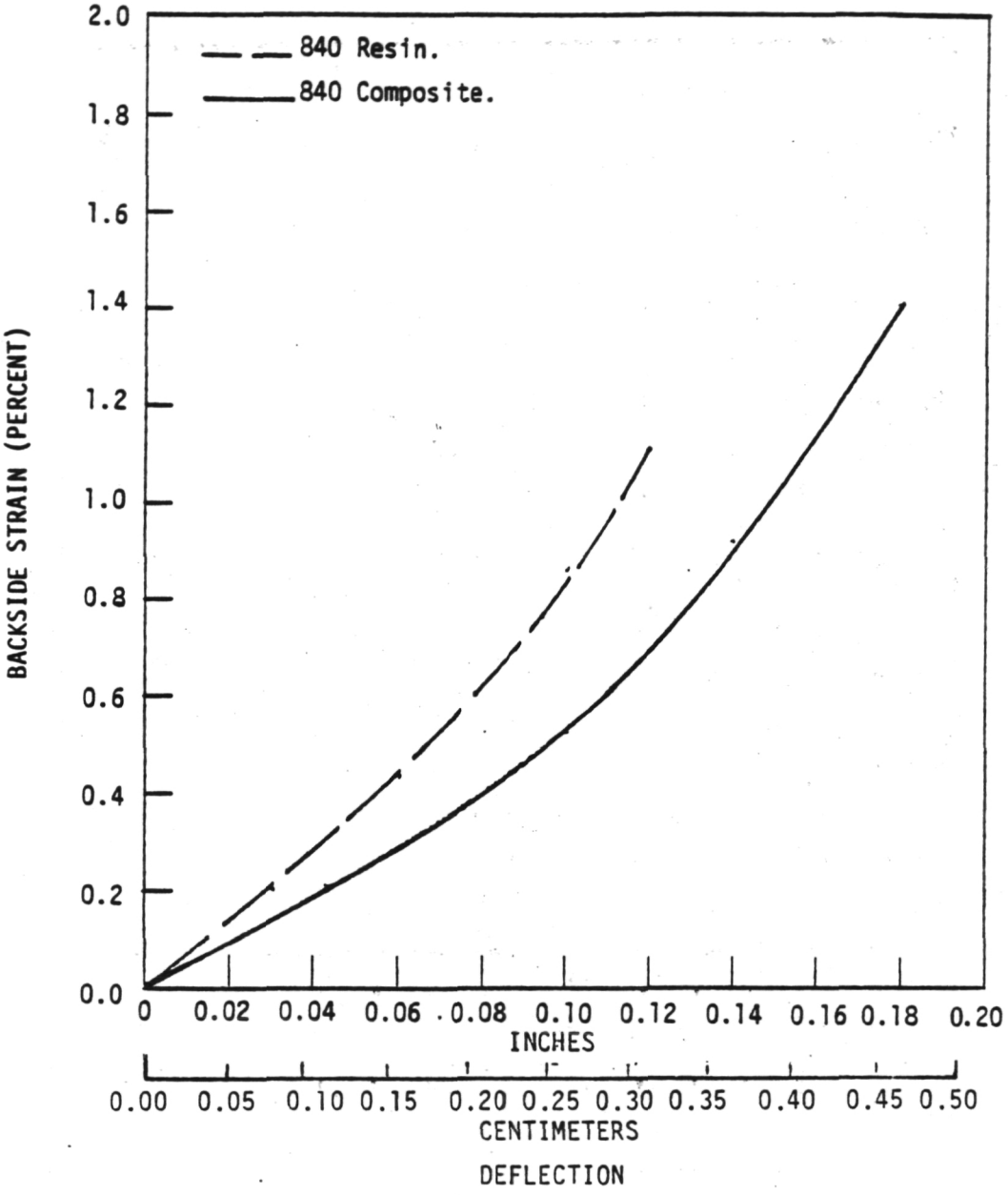

Figure 63. Static deflection-strain data for a 840 epoxy resin plate and a fifteen ply, crossplied 840 composite plate. Strains were measured with strain gages bonded to the backsides of the plates.

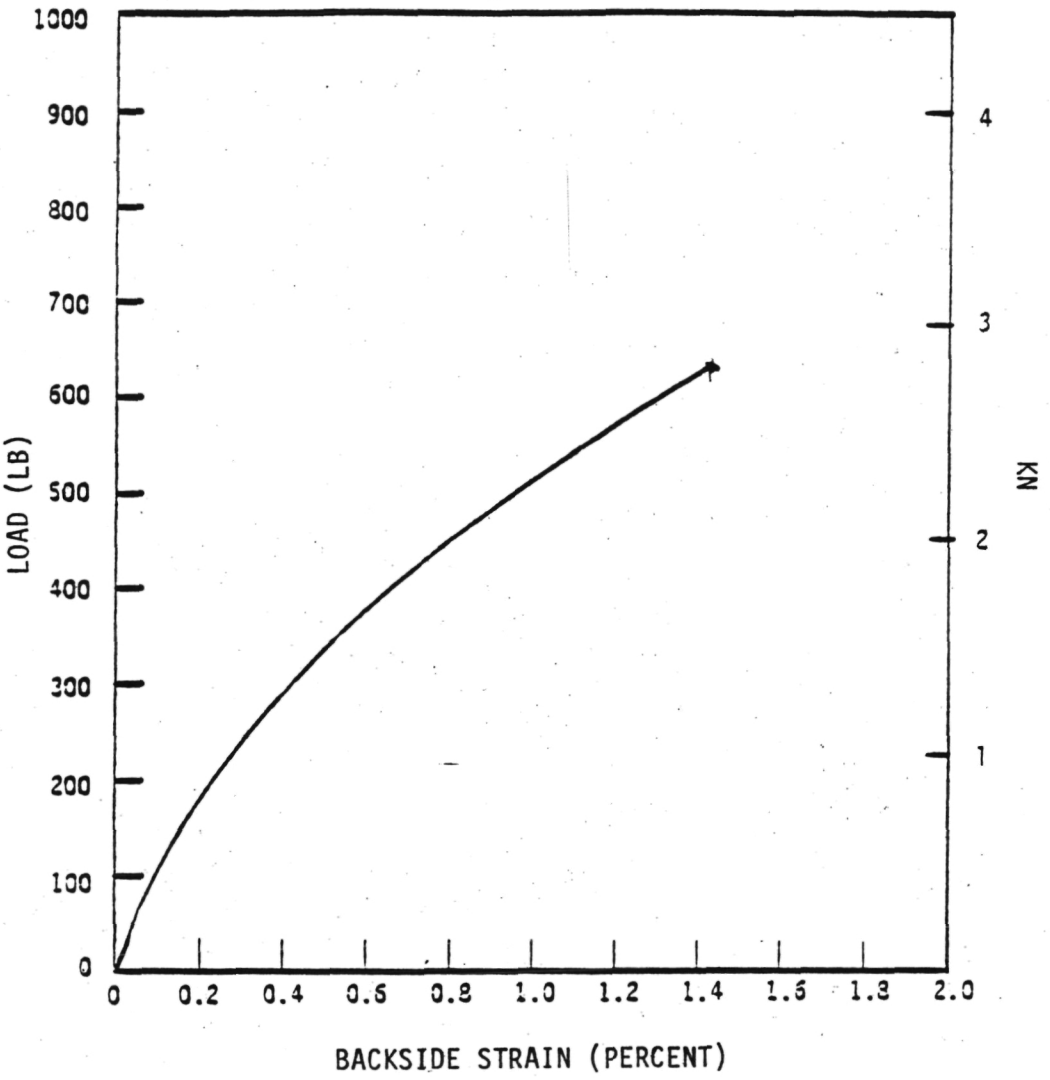

Figure 64. Load-backside strain relationship for fifteen ply crossplied 840 composite. The data were measured under static conditions.

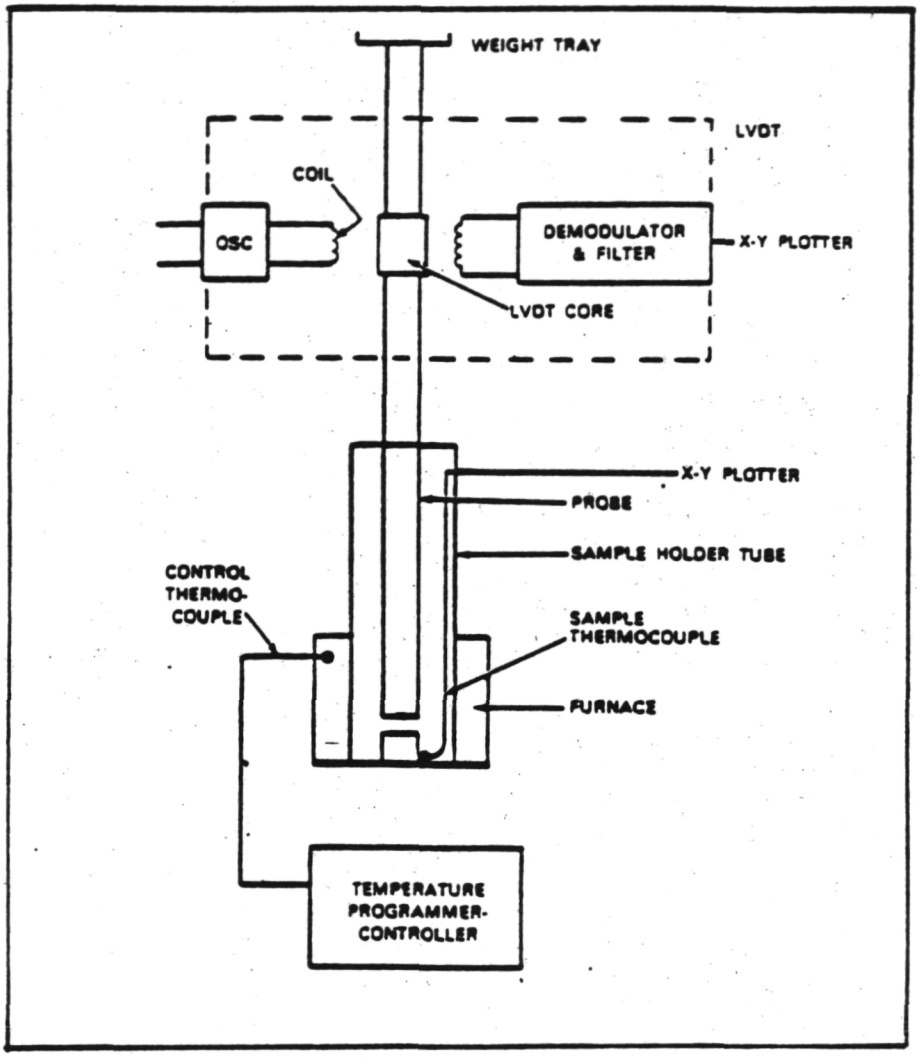

Figure 65. Schematic of the thermal mechanical analyzer.

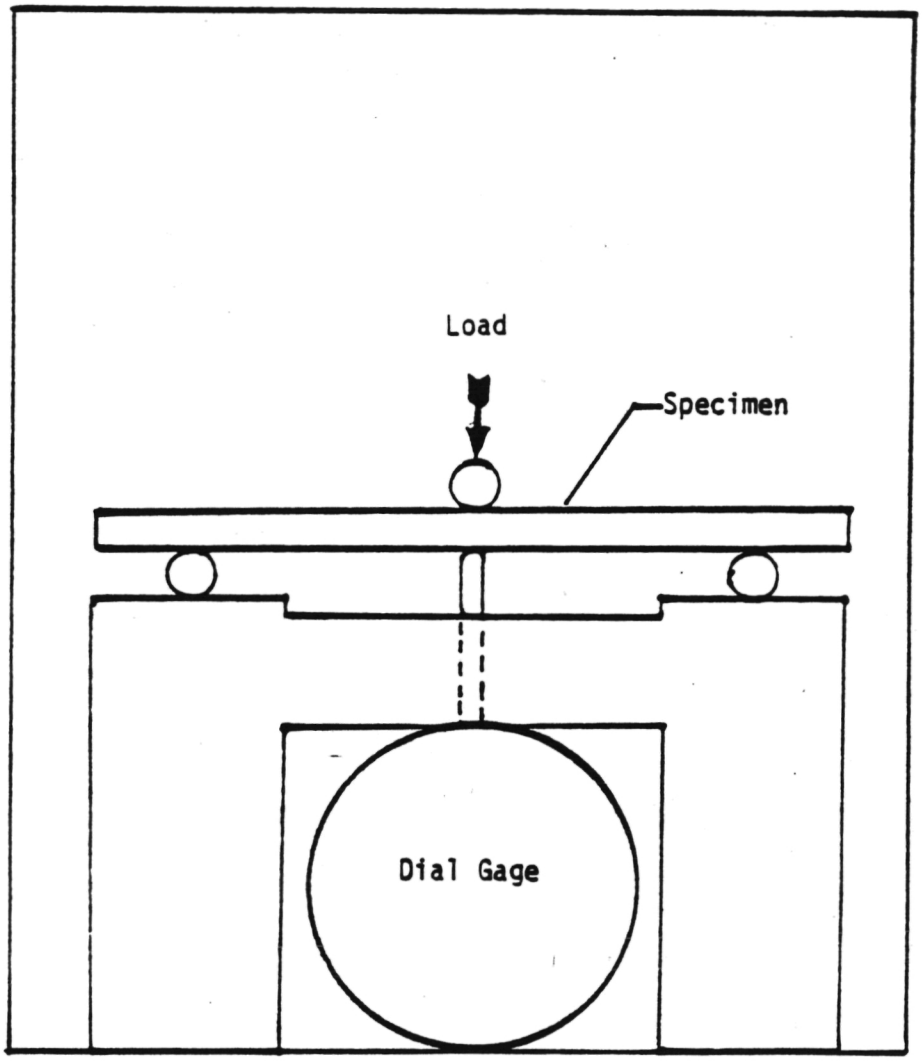

Figure 66. Schematic of the three point bend fixture used for measuring the moduli of composites.

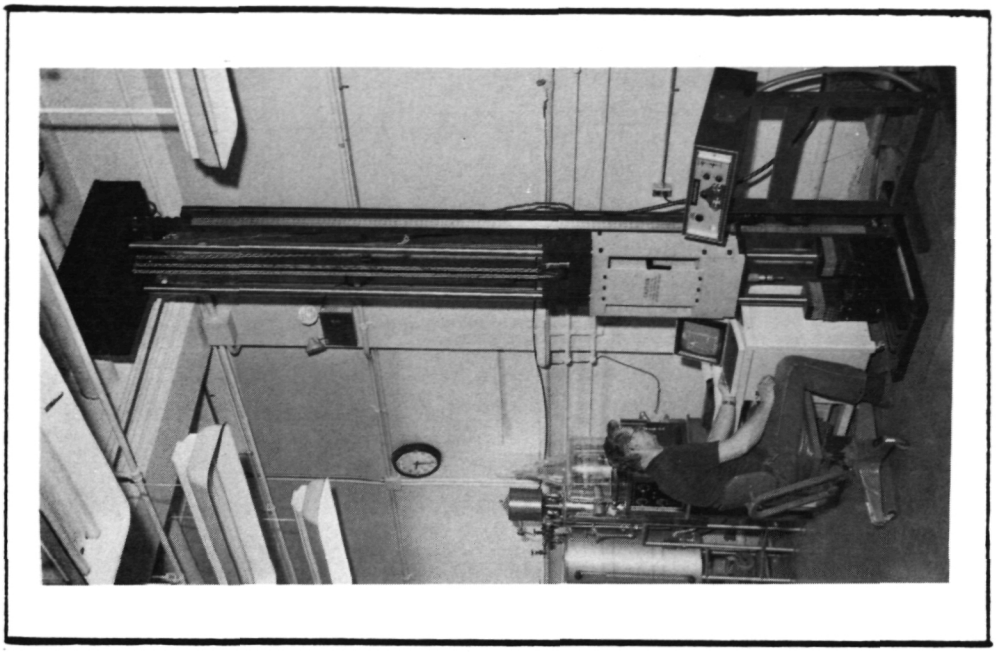

(a)

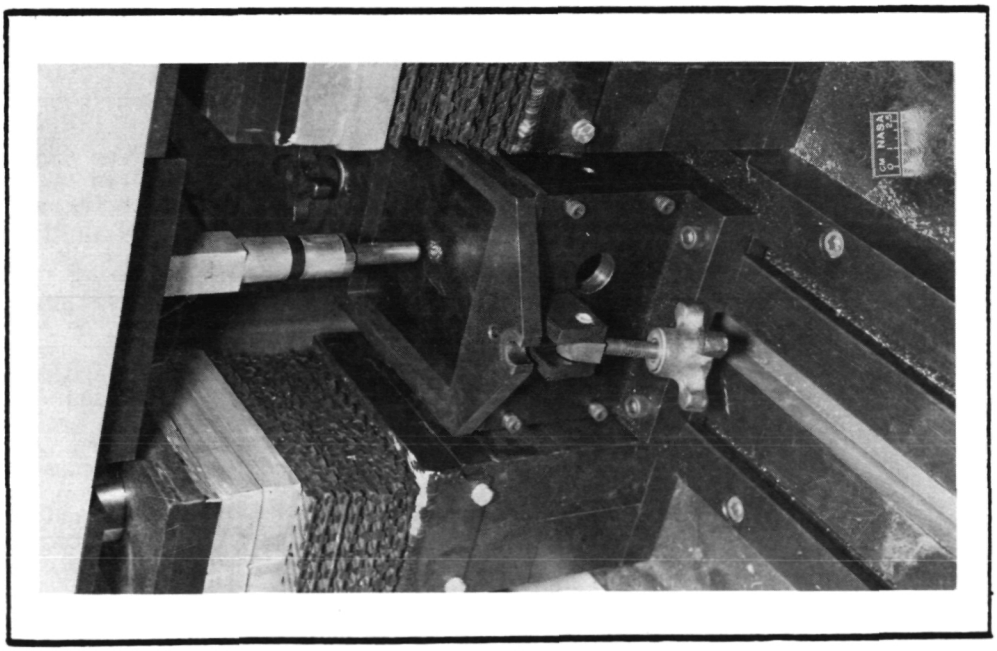

(b)

Figure 67. Instrumented drop weight impact tester used to assess impact resistance of resins and composites. (a) Overall view. (b) Anvil and impactor.

1. Report No.	2. Government Accession No.	3. Recipient's Catalog No.
NASA TM-86886		

4. Title and Subtitle	5. Report Date
Fundamental Studies of Low Velocity Impact Resistance of Graphite Fiber Reinforced Polymer Matrix Composites	November 1985
	6. Performing Organization Code: 505-63-01
7. Author(s): Kenneth J. Bowles	8. Performing Organization Report No.: E-2188
	10. Work Unit No.
9. Performing Organization Name and Address: National Aeronautics and Space Administration, Lewis Research Center, Cleveland, Ohio 44135	11. Contract or Grant No.
	13. Type of Report and Period Covered: Technical Memorandum
12. Sponsoring Agency Name and Address: National Aeronautics and Space Administration, Washington, D.C. 20546	14. Sponsoring Agency Code

15. Supplementary Notes

This report was submitted in partial fulfillment of the requirements for the degree of Doctor of Philosophy to Case Western Reserve University, Dept. of Metallurgy and Materials Science, Cleveland, Ohio in January 1985.

16. Abstract

A study was conducted to relate the impact resistance of graphite fiber reinforced composites with matrix properties through gaining an understanding of the basic mechanics involved in the deformation and fracture process, and the effect of the polymer matrix structure on these mechanisms. It was found that the resin matrix structure influences the composite impact resistance in at least two ways. The integration of flexibilizers into the polymer chain structure tends to reduce the T_G and the mechanical properties of the polymer. The reduction in the mechanical properties of the matrix does not enhance the composite impact resistance because it allows matrix controlled failure to initiate impact damage. Linear polymers, which contain no active groups for crosslinking, do not toughen composites because the fiber-matrix interfacial bond is not of sufficient strength to prevent interfacial failure from occurring. Toughness must be built into the basic polymer backbone and crosslinking structure. It was found that when the instrumented dropweight impact tester is used as a means for assessing resin toughness, the resin toughness is enhanced by the ability of the clamped specimen to deflect enough to produce sufficient membrane action to support a significant amount of the load. Thus, resin strain to failure is also significant. For composite specimens, the amount of deflection is limited by the magnitude of the strain at failure of the graphite fiber (less than 2 percent) and it appears that very little membrane action is realized during the impact of a composite. Unidirectional composites do not appear to simulate the impact behavior of real structural composites and they are not recommended for use in assessing composite impact resistance with the dropweight impact tester. The results of this study indicate that crossplied composite impact resistance is very much dependent on the matrix mechanical properties. When the matrix modulus is reduced, shear induced compressive failure may initiate composite impact failure. When the matrix strength is reduced, interlaminar shear stresses may become significant and initiate impact failure. Both the modulus and the strength of the matrix must be increased to increase the composite impact resistance.

17. Key Words (Suggested by Author(s))	18. Distribution Statement
Graphite fiber; Polymers; Composites; Thermooxidative stability; Mechanical properties	Unclassified - unlimited STAR Category 24

19. Security Classif. (of this report)	20. Security Classif. (of this page)	21. No. of pages	22. Price*
Unclassified	Unclassified		

*For sale by the National Technical Information Service, Springfield, Virginia 22161

National Aeronautics and
Space Administration

Lewis Research Center
Cleveland, Ohio 44135

Official Business
Penalty for Private Use $300

SECOND CLASS MAIL

ADDRESS CORRECTION REQUESTED

Postage and Fees Paid
National Aeronautics and
Space Administration
NASA-451

NASA